

UNIVERSITY OF WOLLONGONG

DOCTORAL THESIS

**Constraining natural contributions to
tropospheric ozone production over
Australia and selected areas of the
Southern Ocean**

Author:
Jesse GREENSLADE

Supervisors:
Jenny Fisher
Clare Murphy

*A thesis submitted in fulfillment of the requirements
for the degree of Doctor of Philosophy
in the*

Centre for Atmospheric Chemistry
School of Earth, Atmospheric, and Life Sciences

November 13, 2019

I, Jesse GREENSLADE, declare that this thesis titled, "Constraining natural contributions to tropospheric ozone production over Australia and selected areas of the Southern Ocean" and the work presented in it are my own. I confirm that:

- This work was done wholly or mainly while in candidature for a research degree at this University.
- Where any part of this thesis has previously been submitted for a degree or any other qualification at this University or any other institution, this has been clearly stated.
- Where I have consulted the published work of others, this is always clearly attributed.
- Where I have quoted from the work of others, the source is always given. With the exception of such quotations, this thesis is entirely my own work.
- I have acknowledged all main sources of help.
- Where the thesis is based on work done by myself jointly with others, I have made clear exactly what was done by others and what I have contributed myself.

Signed: 

Date: 1/8/2019

Contents

Acknowledgements	vii
1 Introduction and Literature Review	1
1.1 The atmosphere	1
1.1.1 Structure	1
1.1.2 Composition and chemistry	2
1.2 Ozone	3
1.2.1 Stratospheric ozone	3
1.2.2 Tropospheric ozone	4
1.2.2.1 Stratosphere to troposphere transport	6
1.2.2.2 Chemical production	6
1.3 Volatile Organic Compounds	8
1.3.1 Emissions	10
1.3.2 Biogenic emissions modelling	11
1.3.3 Isoprene	12
1.3.4 Isoprene chemistry	13
1.3.4.1 High NO _x pathway	14
1.3.4.2 Low NO _x pathway	15
1.3.4.3 Night time processes	15
1.3.5 Radiative Forcing	16
1.4 Formaldehyde	16
1.4.1 Sources and sinks	18
1.4.2 Measurement techniques	19
1.4.2.1 Satellite measurements	20
1.4.2.2 DOAS	21
1.5 Atmospheric Chemistry Modelling	22
1.5.1 Box models	23
1.5.2 Chemical transport models	23
1.5.3 Emissions	24
1.5.4 Uncertainties	25
1.5.4.1 Emissions Inventories	25
1.5.4.2 Resolution	26
1.5.4.3 Chemistry mechanisms	26
1.5.4.4 Clouds	27
1.6 Australia and the southern hemisphere	27
1.6.1 Ozone	27
1.6.2 Biogenic VOCs	28
1.7 Aims	31

2 Data and Modelling	33
2.1 Introduction	33
2.2 Datasets	34
2.2.1 Satellite	35
2.2.1.1 Formaldehyde	35
2.2.1.2 Nitrogen dioxide	36
2.2.1.3 Aerosol optical depth	38
2.2.1.4 Active fires	38
2.2.1.5 Carbon monoxide	38
2.2.1.6 Uncertainties	38
2.2.2 Model datasets	39
2.2.2.1 GEOS-Chem output	39
2.2.2.2 Meteorological reanalysis	39
2.2.2.3 Surface temperatures	39
2.2.3 In situ and ground based datasets	39
2.2.3.1 Short term measurement campaigns	40
2.2.3.2 Ozonesondes	43
2.2.3.3 Wollongong FTIR	43
2.3 GEOS-Chem	46
2.3.1 Overview	46
2.3.2 Installing and running GEOS-Chem	46
2.3.3 Chemical Mechanism	47
2.3.3.1 Nitrogen oxide impacts	50
2.3.3.2 OH regeneration	50
2.3.4 Biogenic emissions from MEGAN	51
2.3.5 Nitrogen oxides	52
2.3.6 GEOS-Chem simulations	53
2.3.6.1 GEOS-Chem outputs	53
2.3.6.2 GEOS-Chem runs	57
2.3.6.3 UCX vs tropchem	58
2.4 OMI satellite formaldehyde	64
2.4.1 Pixel filtering	66
2.4.2 Air mass factor (AMF)	68
2.4.3 Uncertainty	69
2.5 Calculating new AMF	72
2.6 Recalculation of OMI HCHO	75
2.6.1 Outline	75
2.6.2 Creating new shape factors	77
2.6.3 Creating new AMF using GEOS-Chem	78
2.6.3.1 Updating shape factors	78
2.6.3.2 Recalculating the AMF	78
2.6.3.3 Saving the AMF with satellite pixels	79
2.6.4 Vertical columns from AMF	79
2.6.5 Reference sector correction	79
2.6.6 Corrected vertical columns	81
2.6.7 Binning the results daily	84

2.6.8	Difference between original and corrected OMI HCHO columns	85
2.7	Filtering Data	89
2.7.1	Pyrogenic filter	91
2.7.2	Anthropogenic filter	98
2.7.3	Smearing filter	99
2.7.3.1	Calculation of smearing	99
2.7.3.2	NO _x dependence	103
2.8	Summary schematic for OMI HCHO processing	103
2.9	Data Access	106
3	Biogenic Isoprene Emissions in Australia	109
3.1	Introduction	109
3.1.1	Aims	110
3.1.2	Existing emissions estimates	110
3.1.3	Top-down isoprene emissions estimates	111
3.1.3.1	Bayesian inversion	111
3.1.3.2	Linear inversion	112
3.2	Methods	113
3.2.1	Outline	113
3.2.2	Masks and reprocessed satellite HCHO	114
3.2.3	GEOS-Chem emissions	116
3.2.4	Relationship between isoprene emissions and formaldehyde	116
3.2.5	Calculation of modelled slope	118
3.2.5.1	Smearing	118
3.2.6	Modelled background HCHO	120
3.2.7	Calculation of Emissions	124
3.2.8	Running GEOS-Chem using a posteriori emissions	124
3.3	Results	125
3.3.1	A posteriori emissions	127
3.3.1.1	Diurnal variability	133
3.3.1.2	Trends	133
3.3.2	Modelled impacts of reduced isoprene emissions	136
3.3.2.1	Implications for HCHO	137
3.3.2.2	Implications for ozone	137
3.3.3	Comparison with in situ measurements	144
3.4	Uncertainty	147
3.4.1	Top-down emissions	149
3.4.2	Model Uncertainty	150
3.4.3	Satellite Uncertainty	153
3.4.4	Sensitivity to AMF recalculation	159
3.4.5	Sensitivity to filtering	159
3.5	Conclusions and implications	162
4	Stratospheric ozone intrusions	165
4.1	Foreword	165
4.2	Introduction	165
4.3	Data and Methods	167

4.3.1	Ozonesonde record in the Southern Ocean	167
4.3.2	Model description	171
4.3.3	Characterisation of STT events and associated fluxes	171
4.3.4	Biomass burning influence	173
4.3.5	Classifying synoptic conditions during STT events	174
4.4	STT event climatologies	175
4.5	Simulated ozone columns	178
4.6	Stratosphere-to-troposphere ozone flux from STT events	182
4.6.1	Method	182
4.6.2	Results	184
4.6.3	Comparison to literature	189
4.7	Sensitivities and limitations	190
4.7.1	Event detection	190
4.7.2	Flux calculations	190
4.8	Conclusions	192
4.9	Contributions and Acknowledgements	193
5	Summary and Concluding Remarks	195
5.1	Outcomes	195
5.2	Isoprene emissions	196
5.3	Tropospheric Ozone over Australia	196
5.4	Outputs	200
5.5	Future work	200
5.6	Concluding remark	201
A	Relationship between temperature and HCHO	203
B	Daily a priori regression against a posteriori	211
C	Supplementary for Ozone STT chapter	213
S1	Foreword	213
S2	Weather and Smoke analysis	213
S3	Southern Ocean extrapolation	214
S3.1	Outline	214
S3.2	Results	216
Bibliography		219
List of changes		
Added (mh): Australia lacks the ext...	v
Replaced (mh): The primary source is...	v
Added (mh): The second most impo...	v
Deleted (mh): also	v
Replaced (mh): a	vi
Added (mh): Summer (peak season)...	vi
Replaced (mh): In order to examine po...	vi

Added (mh): Background ozone co...	vi
Replaced (mh): only the positive direc...	xxi
Replaced (tb): (OH) and hydroperox...	3
Added (tb): 350	4
Replaced (tb): lower energy ($\lambda < ...$)	4
Replaced (tb): results in a vertical pr...	4
Added (tb): called the <i>ozone layer</i>	4
Replaced (mh): our	6
Added (tb): These properties are la...	9
Added (tb): Other major emission...	9
Added (tb): This thesis mostly foc...	9
Replaced (mh): This thesis focuses	11
Deleted (tb): MEGAN parameterise...	11
Added (tb): Biogenic emissions m...	11
Added (tb): There is a potential iss...	12
Replaced (tb): and other models	12
Deleted (tb): Other models also exis...	12
Replaced (mh): , the optical depth of v...	22
Deleted (mh): can help us	22
Replaced (mh): peoples	22
Deleted (mh): our	22
Replaced (mh): information is lacking	22
Added (tb): (Section 1.3.2)	25
Replaced (tb): may be heavily influe...	25
Deleted (mh): us	26
Deleted (tb): Modelled emissions ar...	26
Added (tb): For example,	26
Replaced (tb): MEGAN	26
Replaced (mh): scientists	28
Deleted (mh): our	28
Replaced (mh): the	28
Replaced (mh): This thesis aims	31
Replaced (mh): This thesis aims	31
Replaced (mh): This thesis aims	31
Deleted (mh): I aim to improve the u...	31
Added (mh): is analysed	31
Deleted (mh): I detail	31
Added (mh): is examined	31
Replaced (mh): This thesis aims	31
Replaced (mh): This thesis aims	31
Replaced (mh): . In this thesis	31
Added (mh): is used	31
Replaced (mh): this thesis aims	32
Replaced (mh): This includes a descri...	32
Replaced (mh): a comparison of	32
Replaced (mh): an analysis of	32

Deleted (mh): .	32
Replaced (mh): topography is not an i...	34
Replaced (mh): GEOS-Chem version 1...	46
Deleted (mh): for us	46
Added (mh): in this work	46
Replaced (mh): For this thesis, GEOS-...	46
Deleted (mh): we start to see	59
Added (mh): becomes apparent	59
Deleted (mh): I use	66
Added (mh): is used	66
Replaced (mh): it is assumed that	70
Replaced (mh): this uncertainty can be...	70
Replaced (mh): gives	73
Deleted (mh): We use	73
Added (mh): is used	73
Replaced (mh): , which allows one to	73
Replaced (mh): Conversion of $d\tau$ to th...	73
Replaced (mh): provides	73
Deleted (mh): us	74
Replaced (mh): this thesis uses	74
Deleted (mh): we calculated	74
Added (mh): is calculated as follows	74
Replaced (mh): Then one	74
Deleted (mh): we have	78
Deleted (mh): our	78
Deleted: .	78
Replaced (mh): the	79
Replaced (mh): a	79
Deleted (mh): our	79
Deleted (mh): we use	79
Added (mh): are used	79
Deleted (mh): We use	98
Added (mh): is used	98
Replaced (mh): provides	102
Replaced (mh): only the E term is cha...	102
Deleted (mh): we remove	102
Added (mh): is removed	102
Replaced (mh): only the positive direc...	104
Deleted (mh): I list	106
Added (mh): are listed	106
Replaced (mh): This chapter describes ...	109
Replaced (mh): the technique is applied	110
Replaced (mh): Isoprene emissions are ...	110
Replaced (mh): an outline is provided ...	110
Replaced (mh): This thesis discusses	110
Added (mh): s	110

Deleted (mh): I develop and analyse	111
Replaced (mh): is developed, analyse...	111
Replaced (mh): H	111
Added (mh): is also looked into	111
Replaced (mh): the Bayesian method i...	112
Replaced (mh): T	113
Added (mh): is broadly followed	113
Replaced (mh): is the	114
Replaced (mh): the OMI product is used	114
Replaced (mh): Ω can be related to	117
Replaced (mh): the	120
Replaced (mh): The a posteriori estim...	132
Replaced: . This	132
Replaced (mh): the following quadrat...	149
Replaced (mh): the	150
Replaced (mh): , the variance in the m...	150
Replaced (mh): T	150
Added (mh): is used	150
Deleted (mh): , I created and tested	162
Added (mh): is created and tested	162

List of Figures

1.1	Pressure (red) logarithmically decreasing, shown with percentage of atmosphere below at several points. Temperature (green) changes throughout the atmosphere. Figure modified from https://climate.ncsu.edu/edu/Structure	2
1.2	Tropospheric ozone processes, Figure 1 in Young et al. (2017). DOI: https://doi.org/10.1525/elementa.265.f1	5
1.3	NO - NO ₂ - O ₃ photoequilibrium cycle without and with (A, B respectively) influence from VOCs. Figure reproduced from Atkinson (2000).	8
1.4	Dependence of ozone production rate on NO _x and VOC concentrations reproduced from Mazzuca et al. (2016).	9
1.5	Simplified isoprene products following oxidation by OH, reproduced from Mao et al. (2013).	13
1.6	The overall radiative forcings and uncertainties of several atmospheric constituents. Reproduced from Stocker et al. (<i>IPCC, 2013: Climate Change 2013: The Physical Science Basis. Contribution of Working Group I to the Fifth Assessment Report of the Intergovernmental Panel on Climate Change</i>), chapter 8.	17
1.7	HCHO spectrum, with a typical band of wavelengths used for DOAS path measurements. Reproduced from Davenport et al. (2015).	20
1.8	An example spectrum showing absorption features used for species concentration measurements by GOME-2. Image reproduced from EU-METSAT and ESA (EUMETSAT 2015).	21
1.9	Standard box model parameters, reproduced from Jacob (1999).	24
1.10	Forest types in Australia reproduced from http://www.agriculture.gov.au/abares/forestsaustralia/australias-forests	29
1.11	Global and Australian isoprene emission factors modified from Guenther et al. (2006).	30
2.1	Example of NO ₂ tropospheric columns for 29 Jan. 2005 from the OMNO2d product. Data downloaded from https://search.earthdata.nasa.gov/search , DOI:10.5067/Aura/OMI/DATA3007.	36
2.2	Average 2005 tropospheric NO ₂ from OMNO2d with pixels screened for < 30% cloud cover.	37
2.3	Climate Prediction Center daily maximum temperature data for 1 Jan. 2005.	40
2.4	Locations of ground based in situ measurements (top panel) and ozonesonde release sites (bottom panel).	41

2.5	Top: MUMBA, SPS1, and SPS2 time-series for HCHO (orange) and isoprene (green), along with detection limits (dashed). Bottom: isoprene measurements superimposed onto a single year.	42
2.6	Mean midday FTIR profile (x_{ret}) and a priori profile (x_{apri}). Shaded area shows the inter-quartile range over the same time period. Profile is averaged between November 2007 and April 2013.	44
2.7	Left panel shows the mean midday (13:00 - 14:00 local time) total column averaging kernel, along with the inter-quartile range (IQR) between November 2007 and April 2013. Right panel shows the mean averaging kernel for the vertical profile over the same time period, coloured by vertical level. One in six vertical levels are labelled and plotted with a solid line, and the rest are shown with dashed lines. The x-axes are unitless in the two plots shown here.	45
2.8	MEGAN schematic, from http://lar.wsu.edu/megan/ . In GEOS-Chem, a pre-computed emission factors map is used for isoprene in lieu of the soil moisture algorithm.	51
2.9	Left to right columns show tropospheric NO ₂ columns (Ω_{NO_2} ; molec cm ⁻²) from GEOS-Chem (GC), OMNO2d (OMI), and the differences. Each row shows one season from 2005, the left two columns use the left colour scale, while the third column uses the right colour scale.	54
2.10	Left and right columns show anthropogenic and soil emissions of NO respectively from GEOS-Chem in molec cm ⁻² s ⁻¹ . Each row shows one season from 2005. Anthropogenic and soil emissions use a logarithmic and linear colour scale respectively.	55
2.11	The first column shows scatter plots of tropospheric NO ₂ columns between GEOS-Chem (y-axis) and OMNO2d (x-axis) at $2^\circ \times 2.5^\circ$. The reduced major axis linear regression is drawn in red, and the equation, regression coefficient (r), and number of grid squares (n) used is inlaid as a legend. The second and third columns show the scatter between emissions and the bias between GEOS-Chem and OMNO2d (GC-OMI), for anthropogenic and soil emissions respectively. The third column has a different x-axis scale for each season. These right two columns share the far right axis; however, emissions are from anthropogenic and soil sources respectively. All scatter points are coloured by the sum of anthropogenic and soil NO emissions (from GEOS-chem), as per the colour bar shown at the bottom.	56
2.12	Surface HCHO simulated by GEOS-Chem with UCX (A: top left), and without UCX (B: top right), along with their absolute and relative differences (bottom left, right respectively). Amounts are the average of all times between 1 Jan and 28 Feb 2007.	59
2.13	As Figure 2.12 but using total column amounts instead of surface concentrations.	60
2.14	As Figure 2.12, except showing isoprene surface concentrations.	61
2.15	As Figure 2.14, except showing isoprene total column amounts.	62

2.16 Total column ozone simulated by GEOS-Chem with UCX (A: top left), and without UCX (B: top right), along with their absolute and relative differences (bottom left, right respectively). Amounts are the average of all times between 1 Jan and 28 Feb 2007.	63
2.17 Here is an impression of the OMI scanning swathes as the housing satellite sweeps around the Earth. The charge-coupled device (CCD) has two dimensions: wavelengths and cross-tracks. The table shows the optical properties for OMI's three channels. Reproduced from Schenkeveld et al. (2017).	65
2.18 Solar and viewing zenith angles, reproduced from http://sacs.aeronomie.be/info/sza.php	66
2.19 HCHO Column amount histograms for a subset of OMI swaths over Australia on the 18th of March 2013. Negative entries are shown in the left panel, positive in the right. Note the different scale between negative and positive panels.	68
2.20 Top row shows $0.25^\circ \times 0.3125^\circ$ binned OMHCHO columns with one day, one month, and one month with non-biogenic masking applied from left to right respectively. Bottom row shows the uncertainty for each grid square after averaging.	71
2.21 Top row: averaged OMI Satellite AMF for 2005, from the OMHCHO dataset (left, AMF_{OMI}), recalculated using GEOS-Chem shape factors (middle, AMF_{GC}), and recalculated using GEOS-Chem shape factors and scattering weights (right, AMF_{PP}). Middle row: AMF time series over 2005 for each recalculation. Bottom row: AMF frequency distributions over January and February. Oceanic pixels are filtered out, only land pixels are included in this figure.	80
2.22 Example of remote Pacific RSC using 8-day average measurements and one month modelled data. Ω_{VC} shows the uncorrected vertical columns, while Ω_{VCC} shows the corrected vertical columns. OMI corrections shows the correction applied globally based on latitude and OMI track number (sensor). Ω_{GC} shows the GEOS-Chem modelled HCHO VC over the reference sector (region within black vertical lines), with Ω_{VCC} showing the corrected OMI VC over the same area.	82
2.23 Example of track correction interpolation for January 1st 2005. Points represent the difference between satellite slant column measurements and modelled slant columns over the remote Pacific.	83
2.24 Row 1: regridded corrected Ω_{HCHO} from OMHCHO on January 1, 2005: original (left), recalculated using new shape factors (middle), and additionally using updated scattering weights (right). Row 2: same but for the monthly average for January 2005. Row 3: the distribution over the month for each of the three column amounts. Distribution bins are logarithmic, resulting in wider bins for higher column amounts.	86

2.25 Monthly pixel counts over Australia (non-oceanic) used in recalculation of vertical columns. N_{GC} refers to the number of pixels used in AMF recalculation without running PP code, N_{PP} refers to those that have been recalculated using PP code. Filters applied are described in Section 2.7.	87
2.26 Top row: averaged OMI satellite VCC for 2005, from the OMHCHO dataset (left, VCC_{OMI}), recalculated using GEOS-Chem shape factors (middle, VCC_{GC}), and recalculated using GEOS-Chem shape factors and scattering weights (right, VCC_{PP}). Middle row: VCC time series over 2005 for each recalculation. Bottom row: VCC frequency distributions over January and February. Oceanic pixels are filtered out, so only land pixels are included in this figure.	88
2.27 Top row shows grid squares filtered out by anthropogenic (left) and pyrogenic (right) influence masks over 2005. Bottom row shows portion of Australian grid squares filtered out each day.	90
2.28 Recalculated OMI vertical HCHO columns and pixel counts for January 2005. Column 1: VCC_{PP} amounts after applying the active fire filter. The filter is applied at $0.25^\circ \times 0.3125^\circ$ resolution, before output is averaged into $2^\circ \times 2.5^\circ$ bins. Column 2: Pixel counts after applying the active fire filter (summed into $0.25^\circ \times 0.3125^\circ$ bins). Row 1-4: increasing number of prior days that have active fires are included when masking fire influence. The first row shows the values without applying any active fire filter. The average and maximum VCC column amount (at $0.25^\circ \times 0.3125^\circ$ resolution), and number of pixels, is inset as text in column 1 of each row. The second to fourth row respectively show the columns after filtering for adjacent fire on up to 2, 4, and 8 prior days.	92
2.29 AAOD from OMAERUVd (columns 1, 2, 3) over Australia for four different scenarios (rows 1-4). Density plots show normalised AAOD frequencies (scale not shown), and the threshold used in this work of 0.03 (see text) is demarcated by a horizontal line. Black Saturday (row 2) refers to the occurrence of widespread bush fires across Victoria. The transported plume in row three can be seen in the overlaid AOD shown in the last column. Scenes in the final column are created using the EOS Worldview website https://worldview.earthdata.nasa.gov/ from satellite products provided therein.	94
2.30 Top: percentage of pixels filtered out by fire and smoke masks in 2005 (left) and 2012 (right). Bottom: percentage filtered out each day from land squares in Australia for the two years shown.	95
2.31 Forest coverage, coloured by predominant tree species.	96
2.32 Top: gas fields and pipelines (2018) for Australia (http://www.ga.gov.au/scientific-topics/energy/resources/petroleum-resources/gas). Bottom: petrol Well locations over Australia (as of 2018) (http://dbforms.ga.gov.au/www/npm.well.search).	97
2.33 Mean (left) and standard deviation (right) of OMNO2d daily $0.25^\circ \times 0.25^\circ$ tropospheric cloud filtered NO ₂ columns.	98

2.34	Top row: 2005 OMNO2d NO ₂ column mean before (left) and after (right) applying the anthropogenic threshold filters as described in the text. Bottom row: time series for Australia, and each region (by colour) shown in the bottom panels, with mean for that region shown as horizontal bars within the bottom panels at the right (over 360-400 on the x-axis). The time series before and after applying the anthropogenic filter are shown on the left and right respectively. The thicker black line shows the mean value over all of Australia, and the grey shaded area shows the inter-quartile range. The dashed and dotted horizontal lines show daily and yearly mean thresholds respectively.	100
2.35	2005 OMNO2d NO ₂ column means (top left) and distributions (top right) for Australia, and each region shown in the area map (by colour). Vertical dashed lines show the threshold for anthropogenic influence; any columns above this value are filtered out. The vertical axis is normalised so that area under the curve adds to unity, and as such is not important except as a visual measure of the relative width between the distributions.	101
2.36	Top: OMNO2d tropospheric NO ₂ columns averaged into 2° × 2.5° horizontal bins for Jan, 2005. Bottom: Scatter plot of NO ₂ against smearing calculations from GEOS-Chem (\hat{S}), with points above and below the smearing threshold range of 800-4600 s coloured red and blue respectively. Points are binned by NO ₂ with and without the smearing filter applied (orange and magenta respectively). Overplotted is the mean and standard deviation (error bars) within each bin. Due to the logarithmic Y scale only the positive direction of standard deviations is shown—we only show the positive direction of standard deviations^{mh} for unfiltered data.	104
2.37	Flow diagram showing how OMHCHO level two swath data is read, processed, and gridded in this thesis.	105
3.1	Top-down isoprene emissions estimate formation using OMHCHORP and GEOS-Chem outputs.	115
3.2	Top left: reduced major axis slope between modelled tropospheric column HCHO and isoprene emissions (E_{GC}) using midday (13:00-14:00 LT) values over for January 2005, per grid square at 2° × 2.5° horizontal resolution. Top right: Squared reduced major axis correlation coefficient for regression in top left. Bottom: Sample of correlations from four grid squares. Coloured dots in top panels correspond to the colour of the regressions shown in bottom panel.	119
3.3	Row 1: monthly slope along with 95% confidence interval both before (blue) and after (magenta) applying the smearing filter for the model grid square containing Sydney over 2005-2012. Row 2: regression coefficient and data point counts before (left) and after (right) performing filtering for slopes shown in row 1. Additionally, limits for r and n used in slope utilisation (see text) are shown with dashed lines. Row 3: slope and confidence interval using the multi-year dataset for each month. Row 4: regression coefficient and data point counts for row 3.	121

3.4 Seasonally averaged smearing (\hat{S} , see text) over 2005. Diamonds represent grid squares which have had at least 10 (pink) or 30 (red) days removed due to the smearing filter over the season. Red crosses show where the filter has removed all data.	122
3.5 Top left: Background total column HCHO based on longitudinally averaged values over the remote Pacific Ocean. Top right: Background total column HCHO based on GEOS-Chem output with isoprene emissions set to zero. Bottom left: Distributions of column amounts over land squares in Australia from the two background definitions and the monthly HCHO average from GEOS-Chem (standard tropchem run). Bottom right: Absolute difference between the two background defined value maps.	123
3.6 Total daily isoprene emissions (in kg) is represented by the area under the sine wave.	125
3.7 Sub-regions used in subsequent figures: Northern, North Eastern, South Eastern, South Western, and Middle. Australia-wide averages will be black or grey, while averages from within the coloured rectangles will match the colour shown here. Oceanic grid squares are filtered out from any area averages made in this chapter.	126
3.8 Row 1: Biogenic emissions of isoprene from GEOS-Chem (a priori, E_{GC}). Row 2: Emissions calculated using the OMI top-down inversion (a posteriori, E_{OMI}). Row 3: Absolute differences between the first two rows. Midday emissions are averaged for each season (DJF, MAM, JJA, SON), and colours represent averaged areas from subregions shown in Figure 3.7. Grey dashed horizontal bars are added to highlight the scale differences between rows.	127
3.9 Regional multi-year seasonal mean a priori emissions (magenta) compared to a posteriori emissions (cyan). Error bars show the regionally averaged uncertainty (calculated as described in 3.4.1). Additional horizontal dashes show the uncertainty plus effects from potential HCHO biases (discussed in Section 3.4.1) from satellite underestimation (40%) and monthly clear sky overestimation (13%).	128
3.10 The multi-year monthly mean (lines) and inter-quartile-range (shaded) of midday (13:00-14:00 LT) isoprene emissions estimates. A priori emissions are shown by the dashed lines and hatched shaded areas show the inter-quartile-range. A posteriori emissions are shown using the solid lines, with inter-quartile-range shown by unhatched shaded areas. Colours denote the region over which the multi-year monthly average was taken, as in Figure 3.7.	130

- 3.11 Scatter plot of a priori emissions against a posteriori emissions using monthly averaged grid squares as regression data points. Data points are created using monthly averages (of midday emissions) for each grid box for each month of summer (DJF) within each region shown. Multiple years of data are used, meaning if a region has 10 grid boxes, the 8 years of data will add up to 10 boxes \times 3 months \times 8 years = 240 data points minus filtered and zero emission squares. Plots are coloured by regions shown in Figure 3.7. The linear best fit regression is inset into each plot along with the line equation and regression coefficient. The normalised distribution of each population is shown at the top and right spine of each subplot, with the right spine (facing the a priori axis) using the a priori axis and scale, and the top spine using the a posteriori axis and scale. 131
- 3.12 Top row: multi-year mean a priori emissions in Tg yr^{-1} from E_{GC} (GEOS-Chem; running MEGAN) and from E_{OMI} (top-down emissions) respectively. The total flux from E_{OMI} is calculated assuming a sinusoidal daily cycle, with daylight hours prescribed for each month as described in Section 3.2.8). Bottom left and right show the absolute and relative differences, respectively. 132
- 3.13 The diurnal cycle of GEOS-Chem a priori emissions (solid line) averaged by month into hourly bins over from 2005 to 2013 along with top-down a posteriori (dashed line) emissions. Standard deviations for the monthly average are shaded for the a priori, and shown with error bars at 13:30 LT for the a posteriori. Top-down emissions shown here are based on monthly midday emissions being the peak of a sine wave which drops to zero after and before daylight hours (see Section 3.2.8). 134
- 3.14 A priori (row 1) and a posteriori (row 2) monthly emissions anomalies from multi-year monthly mean, split by region (see Figure 3.7). 135
- 3.15 Row 1: Isoprene emissions scaling factor α for the average January (left) and July (right) over 2005-2012. Row 2: a priori (magenta, left axis), a posteriori (cyan, left axis), and α (black, right axis) multi-year monthly averages calculated for the $2^\circ \times 2.5^\circ$ grid box containing Sydney. 136
- 3.16 Daily mean total column HCHO amounts from GEOS-Chem with a priori (new emissions run) and a posteriori (tropchem run) a posteriori scaled isoprene emissions, along with the recalculated OMI HCHO columns. Each row shows the average over regions in Figure 3.7. 138
- 3.17 Total column HCHO a priori (left) and a posteriori (middle) isoprene emissions, and their relative differences (right). Top row shows summer (DJF) averaged total columns, while bottom row shows the winter (JJA). 139
- 3.18 Regionally and seasonally averaged HCHO total columns from GEOS-Chem (Ω_{GC} , and Ω_{GC}^α) and recalculated OMI measurements (Ω_{OMI}) side by side. Each row represents one region within Australia, while each column represents from left to right: summer, autumn, winter, spring. Standard deviations between grid boxes used to form the multi-year seasonal average are shown with error bars. 140

3.19 Monthly averaged HCHO profile over the $2^\circ \times 2^\circ$ grid box containing Wollongong modelled by GEOS-Chem before (VMR) and after (VMR $^\alpha$) scaling isoprene emissions. Shaded areas represent the inter-quartile range over the month.	141
3.20 Surface ozone concentrations (ppb) per region over 2005. Concentrations are shown using the left axis, and absolute differences (tropchem run - scaled run) shown in grey using the right axis.	142
3.21 Multi-year seasonal surface (up to ~ 150 m) ozone before (left) and after (middle) scaling isoprene emissions, and their relative differences (right). Top row shows summer (DJF) averaged total columns, while bottom row shows the winter (JJA).	143
3.22 GEOS-Chem grid box ($2^\circ \times 2.5^\circ$) containing Wollongong FTIR, SPS, and MUMBA campaign data.	144
3.23 SPS1, SPS2, and MUMBA (left to right columns respectively) midday (13:00-14:00 local time) measurements of isoprene, HCHO, and ozone (top to bottom rows respectively). Shown in magenta and brown are the a priori and a posteriori GEOS-Chem surface outputs for the matching grid square at midday for days containing measurements.	146
3.24 Multi-year (from all days where both measurements and model data exist: 2007-2012) monthly mean total column (Ω) HCHO from the FTIR instrument at Wollongong (southeast Australia), and the colocated convolved GEOS-Chem equivalent before (Ω_{GC}) and after (Ω_{GC}^α) scaling isoprene emissions. Shaded areas show inter quartile range.	148
3.25 Median and inter-quartile range of multi-year monthly relative uncertainty in the a posteriori. Median relative uncertainty in S and Ω are added as dashed and dotted lines respectively.	151
3.26 Summer (DJF, top row) and winter (JJA, bottom row) a posteriori emissions (left column) and relative error (right column).	152
3.27 Median and inter-quartile range of monthly binned uncertainty in S	154
3.28 Mean and standard deviation (vertical error bars) of total pixel counts per region per season, before (magenta) and after (cyan) applying smearing, pyrogenic, and anthropogenic filters.	157
3.29 Median and inter-quartile range for monthly binned relative uncertainty in satellite vertical columns.	158
3.30 Top row: averaged OMI Satellite AMF for 2005, from the OMHCHO dataset (left, AMF_{OMI}), recalculated using GEOS-Chem shape factors (middle, AMF_{GC}), and recalculated using GEOS-Chem shape factors and scattering weights (right, AMF_{PP}). Middle row: mean and inter-quartile range of each AMF over 2005 for each season. Bottom row: mean and inter-quartile range of non-zero a priori emissions based on the three AMFs (with matching subscripts) along with the a priori emissions from GEOS-Chem.	160

3.31 Multi-year monthly mean values for a posteriori emission estimates calculated with (solid) and without (dashed) applying filters for anthropogenic, pyrogenic, and smearing influences. The portion of pixels within each region which are filtered is shown on the right axis with a blue dotted line.	161
4.1 Ozonesonde release sites and the regions used to examine STT effect on tropospheric ozone levels.	168
4.2 Multi-year monthly median tropopause altitude (using the ozone defined tropopause) determined from ozonesondes measurements at Davis (2006-2013), Macquarie Island (2004-2013), and Melbourne (2004-2013) (solid lines). Dashed lines show the 10th to the 90th percentile of tropopause altitude for each site.	169
4.3 Multi-year mean seasonal cycle of ozone mixing ratio over Davis, Macquarie Island, and Melbourne as measured by ozonesondes. Measurements were interpolated to every 100 m and then binned monthly. Black and red solid lines show median ozone and lapse-rate defined tropopause altitudes (respectively), as defined in the text.	170
4.4 An example of the STT identification and flux estimation methods used in this work. The left panel shows an ozone profile from Melbourne on 8 January 2004 from 2 km to the tropopause (blue dashed horizontal line). The right panel shows the perturbation profile created from band-pass filtering of the mixing ratio profile. The STT occurrence threshold calculated from the 95th percentile of all perturbation profiles is shown as the orange dashed line, and the vertical extent of the event is shown with the purple dashed lines (see details in text). The ozone flux associated with the STT event is calculated using the area outlined with the orange dashed line in the left panel.	172
4.5 Seasonal cycle of STT event frequency at Davis (top), Macquarie Island (middle), and Melbourne (bottom). Events are categorised by associated meteorological conditions as described in the text, with low pressure fronts (“frontal”) in dark blue, cut-off low pressure systems (“cut-off”) in teal, and indeterminate meteorology (“misc”) in cyan. Events that may have been influenced by transported smoke plumes are shown in red (see text for details).	176
4.6 Seasonal distribution of STT events using the alternative STT proxy, obtained from consideration of the static stability at the ozone and lapse rate tropopauses, for Davis (2006-2013), Macquarie Island (2004-2013), and Melbourne (2004-2013).	177
4.7 The distribution of STT events’ altitudes at Davis (top), Macquarie Island (middle), and Melbourne (bottom), determined as described in the text. Events are coloured as described in Fig. 4.5.	178
4.8 The distribution of STT events’ depths, defined as the distance from the event to the tropopause, at Davis (top), Macquarie Island (middle), and Melbourne (bottom), determined as described in the text. Events are coloured as described in Fig. 4.5.	179

4.9 Comparison between observed (black) and simulated (pink, red) tropospheric ozone columns (Ω_{O_3} , in molecules cm ⁻²) from 1 January 2004 to 30 April 2013. For the model, daily output is shown in pink, while output from days with ozonesonde measurements are shown in red. For each site, the model has been sampled in the relevant grid square.	180
4.10 Observed and simulated tropospheric ozone profiles over Davis, Macquarie Island, and Melbourne, averaged seasonally. Model medians (2005-2013 average) are shown as red solid lines, with red dashed lines showing the 10th and 90th percentiles. Ozonesonde medians (over each season, for all years) are shown as black solid lines, with coloured shaded areas showing the 10th and 90th percentiles. The horizontal dashed lines show the median tropopause heights from the model (red) and the observations (black).	181
4.11 Example comparisons of ozone profiles from ozonesondes (black) and GEOS-Chem (red) from three different dates during which STT events were detected from the measurements. The dates were picked based on subjective visual analysis. The examples show the best match between model and observations for each site. GEOS-Chem and ozonesonde pressure levels are marked with red and black dashes respectively.	183
4.12 Top panel: tropospheric ozone attributed to STT events. Bottom panel: percent of total tropospheric column ozone attributed to STT events. Boxes show the inter-quartile range (IQR), with the centre line being the median, whiskers show the minimum and maximum, circles show values which lie more than 1.5 IQR from the median. Values calculated from ozonesonde measurements as described in the text.	185
4.13 (Top) Tropospheric ozone, (I)mpact per event, and (P)robability of event detection per sonde launch, averaged over the region above Davis. The tropospheric ozone column Ω_{O_3} (black, left axis) is from GEOS-Chem, while the STT probability P (magenta, right axis) and impact I (teal, right axis) are from the ozonesonde measurements. The STT impact is multiplied by ten to better show the seasonality. (Bottom) Estimated contribution of STT to tropospheric ozone columns over the region, with uncertainty (shaded area) estimated as outlined in Sect. 4.7. The black line shows STT ozone flux if event lifetime is assumed to be two days, with dashed lines showing the range of flux estimation if we assumed events lasted from one day to one week.	186
4.14 As described in 4.13, for the region containing Macquarie Island.	187
4.15 As described in 4.13, for the region containing Melbourne.	188
5.1 Top row: Summer surface-level ozone before (left) and after (right) scaling isoprene emissions in GEOS-Chem to match top-down estimates. Middle row: absolute (left) and relative (right) differences. Bottom row: linear regression between the two model runs along with a black dashed line representing the 1-1 ratio. Each point represents one summer averaged land grid square (as shown in the top row).	198

5.2 Sub-regions used in subsequent figures. Australia-wide averages will be black or grey, while results from within the coloured rectangles will match the colours shown here.	199
A.1 Top row (left): surface temperature averaged over January and February 2005. Top row (right): correlation between spatially averaged GEOS-Chem temperatures and recalculated satellite vertical columns. Second row: GEOS-Chem surface temperatures correlated against GEOS-Chem HCHO, with different colours for each grid box, and black showing the spatially averaged correlation over time. Third row: as second row, except GEOS-Chem HCHO comes from the biogenic emissions only simulation. A reduced major axis regression is used within each gridbox using daily overpass time surface temperature and HCHO. The distribution of slopes (solid) and regression correlation coefficients (dashed) for the exponential regressions is shown in the inset panels in rows 2 and 3.	204
A.2 As Figure A.1 but for northern Australia.	205
A.3 As Figure A.1 but for south-western Australia. TODO: Fix y axis in subplot 322	206
A.4 Surface HCHO from GEOS-Chem overpass output (midday) on the Y axis vs surface temperatures at midday (T_{GC}) and vs maximum daily temperatures from the CPC data set (T_{CPC}). Top row: Sydney grid square scatter plot and regression with one data point for each day in the summer of 2005-2006. Bottom row: as top row except averaging over several grid boxes covering south eastern Australia (SEA: 37°S to 29°S, 146°E to 153.5°W). Grid squares with pyrogenic influence detected are removed (prior to any averaging) in the right column.	208
A.5 OMI recalculated vertical columns of HCHO on the Y axis vs surface temperatures at midday (T_{GC}) and vs maximum daily temperatures from the CPC data set (T_{CPC}). Top row: Sydney grid square scatter plot and regression with one data point for each day in the summer of 2005-2006. Bottom row: as top row except averaging over several grid boxes covering south eastern Australia (SEA: 37°S to 29°S, 146°E to 153.5°W). Grid squares with pyrogenic influence detected are removed (prior to any averaging) in the right column.	209
B.1 Scatter plot (binned hexagonally with darker colours representing higher data-point frequency) along with the distributions of MEGAN (y axis) and the top-down estimate (x axis). This figure is based on summer (December - February) midday values over multiple years (2005-2012). Coloured by regions shown in Figure 3.7.	212

S1	Example detection of biomass burning influence using AIRS total column CO. The top panel (17 October 2007) shows a day when ozone above Melbourne (purple dot) could have been caused by a transported biomass burning plume, and so was flagged in subsequent analysis. The bottom panel (3 February 2006) shows a day when ozone over Melbourne was not influenced by transported smoke.	214
S2	(Left) Vertical profile of ozone (black), relative humidity (blue), and temperature (red) measured by ozonesonde over Melbourne on 3 February 2005. The detected ozone STT event is highlighted in pink. Tropopause heights using both the ozone definition (black dashed line) and lapse rate definition (red dashed line) are also shown. (Right) Geopotential heights at 500 hPa from the ERA-Interim reanalysis, with wind vectors over-plotted. Also shown is the 1 PVU contour line (purple).	215
S3	Same as Fig. S2 but for 13 January 2010. Also shown in this figure is the 2 PVU contour (white), often used to determine dynamical tropopause height.	216
S4	Region used for large SO estimation of STT flux	217
S5	(Top) The three quantities used to calculate the total Southern Ocean ozone flux from STT events. The tropospheric ozone column Ω_{O_3} (black, left axis) is from GEOS-Chem, while the STT probability P (magenta, right axis) and impact I (teal, right axis) are from the ozonesonde measurements. The STT impact is multiplied by 10 to better show the seasonality. (Bottom) Estimated contribution of STT to tropospheric ozone columns over the Southern Ocean. The shaded area shows the uncertainty as calculated in Sect. 6 of the parent document, with the -dashed lines showing the range of values when assuming events last one day (upper dashed line) up to one week (lower dashed line).	218

List of Tables

2.1	Detection limits for MUMBA	40
2.2	Species and lumped species from the GEOS-Chem mechanism.	49
2.3	OMI quality flag values from Kurosu and Chance (2014)	67
2.4	Satellite pixels remaining after filtering by active fires, smoke, and anthropogenic masking. In parenthesis are the portion of pixels filtered.	89
2.5	NO_2 averages (10^{14} molec cm^{-2}) by region before and after filtering for anthropogenic emissions using 2005 data from the OMNO2d product.	99
2.6	Smearing filters or typical slopes (S) from literature.	103
2.7	Isoprene to HCHO yields and lifetime.	106
3.1	Isoprene emissions (Tg/yr) from Australia	133
3.2	2005-2012 trend ^a in surface isoprene mixing ratio (ppbvC yr^{-1}) from simulations using a priori and a posteriori isoprene emissions.	135
3.3	Campaign measurements compared to model output [ppb].	145
3.4	Mean total column HCHO amounts in 10^{15} molec cm^{-2} at Wollongong.	147
3.5	Relative uncertainty estimates.	149
3.6	Uncertainties in satellite total column HCHO.	157
4.1	Number of sonde releases at each site over the period of analysis.	168
4.2	Total number of ozonesonde detected STT events, along with the number of events in each category (see text).	175
4.3	Seasonal STT ozone contribution in the regions near each site, in $\text{kg km}^{-2} \text{ month}^{-1}$. In parentheses are the relative uncertainties.	189
5.1	Isoprene emissions from MEGAN and top-down estimate in Tg C a^{-1} , along with ozone surface amounts in ppb.	197

Chapter 1

Introduction and Literature Review

1.1 The atmosphere

The atmosphere is made up of gases held to the earth's surface by gravity. These gases undergo transport on all scales, from barbecue smoke being blown about the garden, to smoke plumes from forest fires travelling across the world and depositing in the Antarctic snow. They take part in innumerable chemical reactions along the way, largely driven by solar input and interactions with each other. Many gases are emitted into the atmosphere by soil, trees, factories, cars, seas and oceans. They are also deposited back to the surface both directly and in rainfall.

The atmosphere is made up of nitrogen (N_2 : $\sim 78\%$), oxygen (O_2 : $\sim 21\%$), and argon (Ar : $\sim 1\%$), along with water (H_2O) and *trace gases* (those that make up less than 1% of the atmosphere). Atmospheric H_2O content can be as high as 4% depending on local conditions. Beyond these major constituents the atmosphere has a vast number of trace gases, including carbon dioxide (CO_2 : $\sim 0.4\%$), ozone (O_3 : $.000001\%$ to 0.001%), and methane (CH_4 : $\sim 0.00018\%$) (*Earth System Research Laboratory; Global Monitoring Division*; Brasseur and Jacob 2017, Ch. 2). Trace gases in the atmosphere can have a large impact on conditions for life on earth. They combine, break apart, and react with each other affecting all surface ecosystems upon which life depends.

One important trace gas is ozone, as it directly affects the climate, human health, and ecosystem productivity. The ozone budget (production, loss, and transport) is relatively uncertain over Australia. This thesis focuses on ozone in the troposphere over Australia and sites in the nearby Southern Ocean. It also estimates emissions of isoprene, one of the important precursors to tropospheric ozone production. This chapter provides background on the structure and composition of the atmosphere and introduces the key atmospheric species examined in this thesis, as well as relevant techniques used to measure and model chemistry in the atmosphere.

1.1.1 Structure

Most of the atmosphere ($\sim 85\%$) is within 10 km of the earth's surface. This is due to gravity, which causes air pressure to decrease logarithmically with altitude. Any entity is subjected to the weight of the air above it, and the structure of the atmosphere is driven by this pressure.

The atmosphere extends above the earth's surface to the edges of space. This is split into various layers, defined by the *lapse rate*: the decrease in temperature (T) with

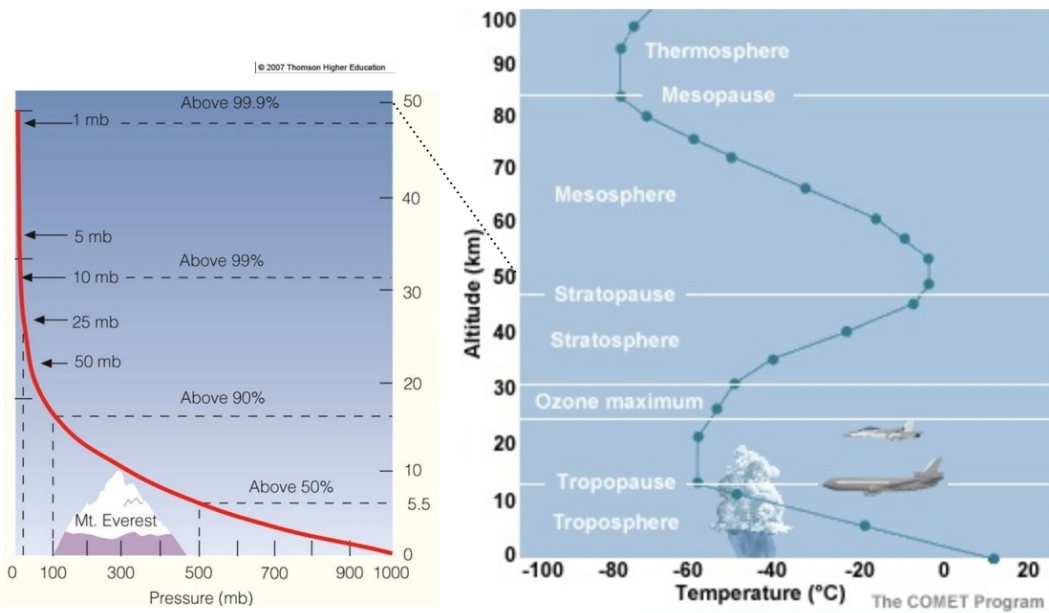


FIGURE 1.1: Pressure (red) logarithmically decreasing, shown with percentage of atmosphere below at several points. Temperature (green) changes throughout the atmosphere. Figure modified from <https://climate.ncsu.edu/edu/Structure>.

increasing altitude (z), or $\frac{-dT}{dz}$. Figure 1.1 shows the pressure and temperature profiles against altitude through the atmosphere. The first layer is the troposphere, which extends to roughly 10 km and is characterised by positive lapse rate (or decreasing temperature with altitude). At the top of the troposphere (the tropopause) the temperature stops decreasing, and then the stratosphere is defined by a negative lapse rate. This is due to ultraviolet radiation being absorbed by ozone, and leads to a very vertically stable environment.

In addition to these atmospheric layers, the troposphere can be subset into the *boundary layer* and the *free troposphere*. The *boundary layer* is the lowest layer and involves increased atmospheric mixing due to ground heating and friction effects. It generally extends from the surface up to 200 m - 1000 m, above which the ground effects have fewer direct impacts. The *free troposphere* is the remainder of the troposphere, where trace gas concentrations are more affected by transport and chemistry. Transported trace gases (and particulates) can come from the stratosphere or local to global scale winds and jet streams.

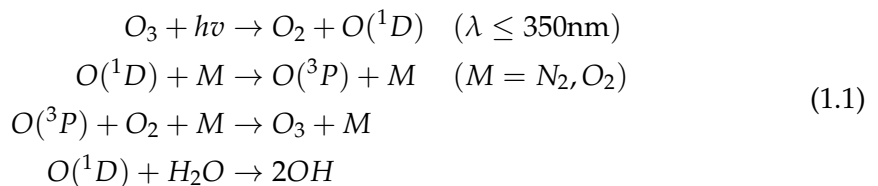
1.1.2 Composition and chemistry

There are myriad trace gases in the atmosphere, emitted by plants, animals, earth, and water. These gases react with one another and over time they either deposit back onto the earth or form more stable compounds such as carbon dioxide (CO_2). Oxidation

and photolysis (the process of being broken apart by photons) are the two main processes whereby compounds are broken down in the atmosphere. Products formed in these reactions are sometimes called child products.

Hydroxyl (OH) and hydroperoxyl (HO_2) radical^b concentrations largely determine the oxidative capacity of the atmosphere. The OH radical drives many processes in the atmosphere, especially during the day when it is produced by the photolysis of ozone (Atkinson 2000). OH is a key species that reacts with nearly all the organic compounds in the troposphere, with only a few exceptions (Atkinson 2000). Over land, isoprene (C_5H_8) and monoterpenes ($\text{C}_{10}\text{H}_{16}$) account for 50% and 30% of the OH reactivity respectively (Fuentes et al. 2000).

Since radicals are involved in all oxidative chemistry in the atmosphere it is important for models to accurately represent them. This is difficult as they are coupled with so many other species and measurements of OH are not readily available on a global scale. OH formation in the clean troposphere is driven by ozone photolysis, as excited oxygen atoms ($\text{O}({}^1\text{D})$) are created and react with water to form OH, shown in reaction sequence 1.1 (Atkinson 2000; Atkinson and Arey 2003):



where $h\nu$ represents radiation and M is an inert molecule. This shows that some of the $\text{O}({}^1\text{D})$ recycles back to ozone, while some forms OH. In the late 1990s it was thought that OH radicals were formed exclusively from photolysis of O_3 , HONO, HCHO, and other carbonyls ($\text{R}_2\text{C=O}$) (Atkinson 2000). It has been shown since that OH is recycled in various processes. For example isoprene (C_5H_8) was thought to be a sink of OH until it was shown by Paulot et al. (2009b) that the radicals are recycled. This recycling process is discussed in more detail in section 1.3.4.

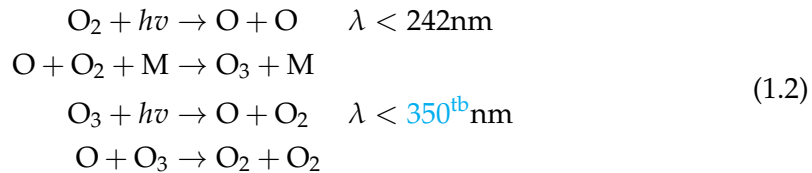
1.2 Ozone

Ozone (O_3) is an important greenhouse gas and oxidant. It is mostly located in the stratosphere and prevents much of the shorter wavelength solar radiation from reaching the earth's surface. Ozone in the troposphere is less beneficial, leading to health issues, radiative forcing, and crop death (Stevenson et al. 2013). Understanding and accurately portraying ozone concentrations in the troposphere is important to allow accurate predictions of future climate. This will become even more important as climate change alters the atmosphere (Hegglin and Shepherd 2009).

1.2.1 Stratospheric ozone

In the stratosphere, ozone production is driven by the Chapman mechanism, as high energy radiation (with wavelengths $\lambda < 242$ nm) photolyses the molecular oxygen (O_2) in the atmosphere (Brasseur and Jacob 2017, Chapter 3, section 2). The Chapman

mechanism involves several reactions that lead to rough equilibrium of O, O₂, O₃ and pressure, as follows:



The high energy photons ($\lambda < 242$ nm) are present from the top of the atmosphere but are mostly removed before reaching the troposphere as their energy is used to split the O₂ molecules. The lifetime of O against loss by O₂ is less than a second in the troposphere, and produced O₃ quickly returns to O and O₂, as *lower energy ($\lambda < 350$ nm) photons are abundant*~~low energy ($\lambda < 1180$ nm) photons and M are abundant~~^{tb}. The reduced light penetration towards the surface, in addition to the logarithmic increase in atmospheric pressure (which affects M abundance) *results in a vertical profile of ozone that peaks in the stratosphere*~~.drives the vertical profile of ozone into what is called the ozone layer.~~^{tb} This is a layer of relative ozone abundance within the stratosphere *called the ozone layer*^{tb}.

Satellite based measurements of ozone were instrumental in identifying a gap in the ozone layer (the ozone hole), where ozone concentrations were unexpectedly low. Since the Montreal Protocol on Substances that Deplete the Ozone Layer was established in August 1987, and ratified in August 1989, new satellites and measurement stations were set up to monitor ozone in the stratosphere. Detecting ozone from the surface up to the top of the stratosphere requires techniques such as remote sensing and ozonesonde releases. Ozonesondes are weather balloons (with attached ozone detectors) that detect ozone concentrations up to the mid stratosphere (~ 30 km), providing a vertical profile over a single location. Ozonesondes have been released periodically for decades over some cities, allowing long term ozone concentration profile analysis (e.g., Brinksma et al. 2002). A small network of ozonesonde release sites (including Davis, Macquarie Island, and Melbourne) is available from the world ozone and ultraviolet radiation data centre <http://woudc.org/data/explore.php> and is used in Chapter 4 to examine stratospheric impacts on tropospheric ozone (see Section 2.2.3.2 for more info on these ozonesondes).

1.2.2 Tropospheric ozone

Ozone in the lower atmosphere is a serious hazard that causes health problems (Hsieh and Liao 2013), causes billions of dollars of damage to agricultural crops (Avnery et al. 2013; Yue et al. 2017), and increases the rate of climate warming (Myhre and Shindell 2013). Around 5 to 20 percent of all air pollution related deaths are due to ozone (Monks et al. 2015), which translates to roughly 800 thousand deaths per year (Lelieveld et al. 2013). In the short term, ozone concentrations of ~50-60 ppbv over eight hours or ~80 ppbv over one hour are agreed to constitute a human health hazard (Ayers and Simpson 2006; Lelieveld et al. 2009). Long term exposure causes problems with crop loss and ecosystem damage (Ashmore, Emberson, and Murray Frank 2003), and concentrations may get worse in the future (Lelieveld et al. 2009; Stevenson et al.

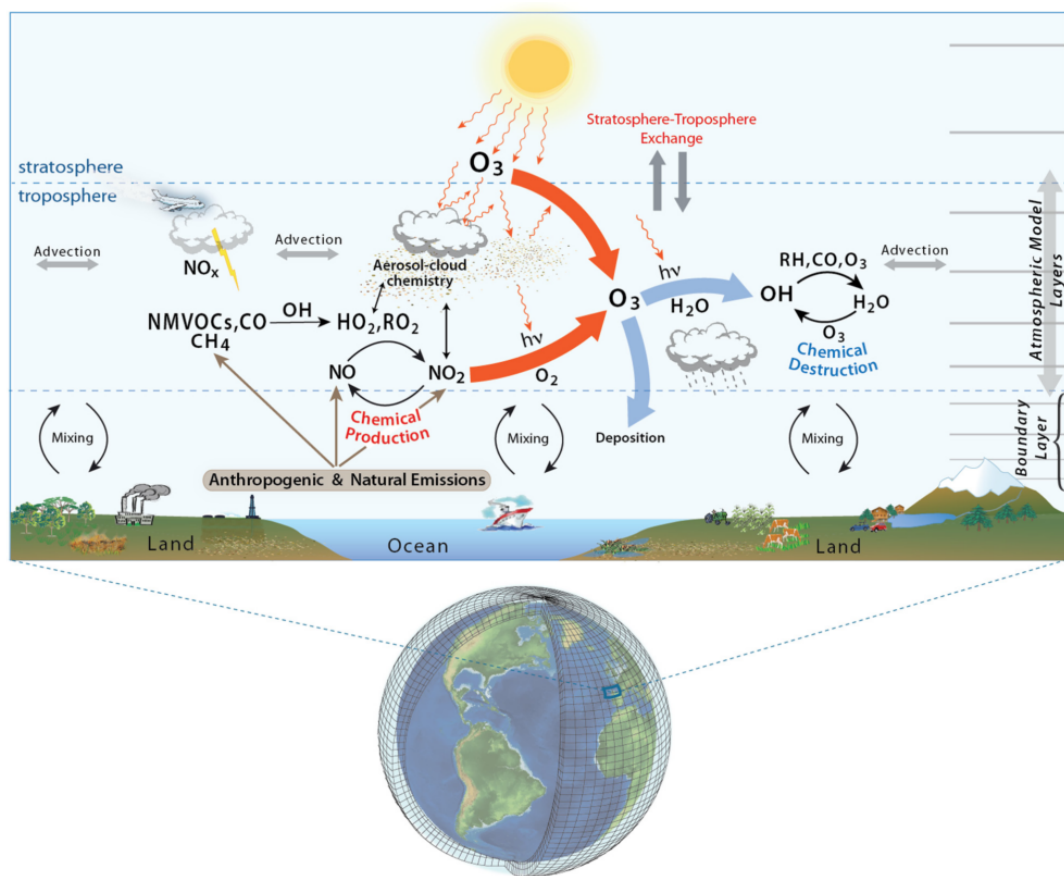


FIGURE 1.2: Tropospheric ozone processes, Figure 1 in Young et al. (2017). DOI: <https://doi.org/10.1525/elementa.265.f1>.

2013). For example, future tropospheric ozone enhancements are projected to drive reductions in global crop yields equivalent to losses of up to \$USD₂₀₀₀ 35 billion (US dollars in the year 2000) per year by 2030 (Avnery et al. 2013), along with detrimental health outcomes equivalent to ~\$USD₂₀₀₀ 11.8 billion per year by 2050 (Selin et al. 2009). Recently Yue et al. (2017) showed that the net effect of near-surface ozone is an approximately 14% decrease in net primary productivity in China. They also state that in order to wind back most of this productivity decrease, drastic measures are required.

Figure 1.2, reproduced from Young et al. (2017), shows a summary of the major processes and emissions affecting tropospheric ozone. This thesis focuses on improving the highly uncertain natural emissions of non-methane volatile organic compounds (NMVOCs) from Australia, and estimating how much ozone is transported down from the stratosphere.

Generally there are two main drivers of tropospheric ozone concentrations: transport from the stratosphere and chemical production due to emissions of precursors. Tropospheric ozone is lost via chemical destruction and dry deposition, estimated to be $4700 \pm 700 \text{ Tg yr}^{-1}$ and $1000 \pm 200 \text{ Tg yr}^{-1}$, respectively (Stevenson et al. 2006; Young et al. 2017). The main loss channel is through photolysis and collisions, and

leads to OH production (equation 1.1).

1.2.2.1 Stratosphere to troposphere transport

Historically, ozone transported down from the stratosphere was thought to contribute 10-40 ppb to tropospheric ozone levels, making up 50% of tropospheric concentrations (Atkinson 2000; Stohl et al. 2003). The proportion was revised down to around 10% over the years as measurement and modelling campaigns improved ourscientists^{mh} understanding of global scale transport, mixing, and chemistry (Guenther et al. 2006; Monks et al. 2015). Intrusions of stratospheric air into the troposphere are often called Stratosphere to Troposphere Transport (STT) events. Although most tropospheric ozone comes from production, STT enhancements of ozone are measurable and can be regionally important (e.g., Jacobson and Hansson 2000; Lelieveld et al. 2009; Kuang et al. 2017). Additionally, upper tropospheric ozone can be transported long distances (Cooper et al. 2004), affecting measurements far downwind of where stratospheric mixing may be taking place. An analysis of the Atmospheric Chemistry and Climate Model Inter-comparison Project simulations showed STT enhances tropospheric ozone by $540 \pm 140 \text{ Tg yr}^{-1}$ (Young et al. 2013), equivalent to $\sim 11\%$ of the tropospheric ozone column (Monks et al. 2015).

Ozone transported to the troposphere from the stratosphere can occur through diffusion (relatively slowly) or direct mixing (as STT). STT often occur as tongues of stratospheric air that descend into the troposphere before becoming detached. These can be due to low pressure systems and jet streams (Sprenger, Croci Maspoli, and Wernli 2003; Alexander et al. 2013). It is possible to model this process and estimate how much ozone is being transported by STT (e.g., Young et al. 2013; Ojha et al. 2016). Model based estimates require validation against actual measurements, such as those from ozonesondes or satellites. It has been estimated that climate change will lead to increased STT through acceleration of the Brewer Dobson circulation (Hegglin and Shepherd 2009), a large scale transport system that affects the structure and composition of the atmosphere, and meteorology, in the tropics. Hegglin and Shepherd (2009) estimated that ozone transport would increase by 23% globally by 2095 (relative to 1965), $\sim 30 \text{ Tg yr}^{-1}$ in the southern hemisphere and $\sim 121 \text{ Tg yr}^{-1}$ in the northern hemisphere.

STT mostly impacts the upper troposphere, although some areas are impacted down to the surface. Over both ocean and land STT can lead to seasonal enhancements of upper and lower tropospheric ozone concentrations (Lin et al. 2015; Liu et al. 2017a; Kuang et al. 2017). A confounding factor is that stratospheric based ozone enhancement can be transported horizontally, and is not confined to the area where intrusion into the troposphere occurred. Understanding of STT needs to be improved to allow source attribution of the causes of local ozone enhancements (Lin et al. 2015).

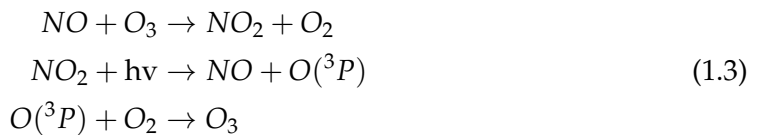
1.2.2.2 Chemical production

Tropospheric ozone concentrations are enhanced by ozone precursor emissions; including NO, NO₂, CO, and VOCs such as isoprene (Atkinson 2000; Young et al. 2013; Marvin et al. 2017). Ozone predictions are uncertain and changing climate affects

transport, deposition, destruction, and natural precursor emissions. All of these processes are tightly coupled and difficult to accurately model, as they depend on uncertain assumptions such as CO₂ dependency (Young et al. 2013). Despite significant advances over the prior decades, there remain large uncertainties about ozone precursors in the troposphere (Mazzuca et al. 2016). Tropospheric ozone is regulated by NO and NO₂ concentrations, which form an equilibrium (Cape 2008; Young et al. 2017). At all scales, pyrogenic (fire) and anthropogenic (man-made) emissions can be important; however, biogenic VOC emissions are a nearly constant source of potential production during the day. Smoke plumes from biomass burning can carry ozone precursors, creating higher ozone concentrations downwind of the plume's source. Emissions of precursors from large cities (primarily from traffic and power production) can impact ozone concentrations. These impacts are not always straightforward due to the nonlinear relationship between ozone and its precursors. Recently, modelled ozone concentrations have been shown to be most sensitive to NO_x (\equiv NO₂ + NO) sources (such as lightning and car exhaust emissions) and isoprene emissions (Christian et al. 2018).

NO_x is an important chemical family in the atmosphere, which interacts with ozone and regulates the atmospheric oxidative capacity. NO_x and VOC emissions affect the tropospheric ozone equilibrium and can lead to enhanced ozone formation, shown in figure 1.2. NO_x compounds are short-lived, with emissions from power generation and transport being the main driver of concentrations (Delmas, Serca, and Jambert 1997). NO_x is removed primarily by conversion to nitric acid (HNO₃) or alkyl nitrates (RONO₂) followed by wet or dry deposition (Ayers and Simpson 2006; Romer Present, Zare, and Cohen 2019). Ozone in rural areas is often higher than in populous cities, due to titration (removal) of ozone by NO in areas with high anthropogenic emissions (Cooper, Gilge, and Shindell 2014; Monks et al. 2015).

As discussed above, STTs are responsible for $\sim 11\%$ of the tropospheric column of ozone, with the remainder produced photochemically. A recent summary by Young et al. (2017) estimated ozone production and loss in the troposphere to be $\sim 4900 \text{ Tg yr}^{-1}$, and $\sim 4500 \text{ Tg yr}^{-1}$ respectively. These numbers are at the global scale, and it should be noted that meteorology and topography can play dominant roles at local to regional spatial scales (e.g., Kuang et al. 2017). The main processes involved are shown in figure 1.2, with ozone and NO_x concentrations regulated by the following reactions (Sillman 1999; Atkinson 2000):



VOC emissions can alter this process, essentially replacing ozone in the first stage of the above equation. The process without and with the influence of VOCs (panel A and B respectively) is summarised in Figure 1.3. Depending on local atmospheric conditions, ozone production can be limited by the presence of VOC or NO_x concentrations, and this is often referred to as the VOC limited or NO_x limited regime.

Net formation or loss of O₃ is determined by interactions between VOCs, NO_x, and HO_x, and is a complicated system of positive and negative feedbacks (Atkinson 2000).

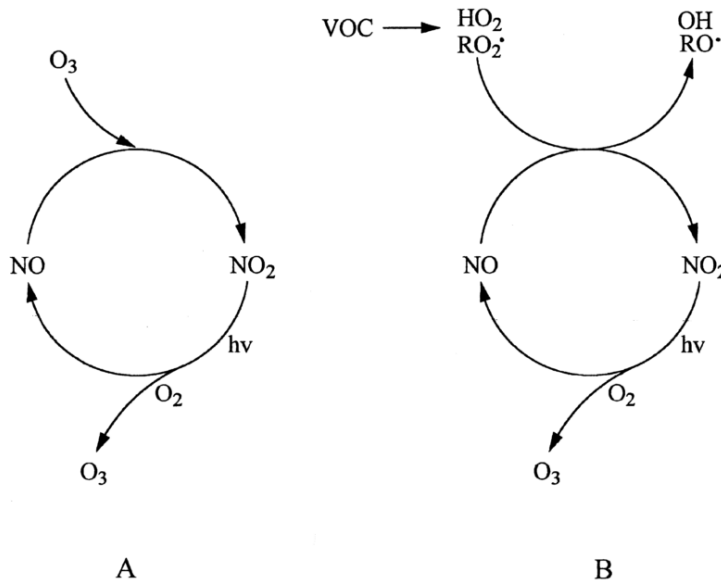


FIGURE 1.3: NO - NO₂ - O₃ photoequilibrium cycle without and with (A, B respectively) influence from VOCs. Figure reproduced from Atkinson (2000).

Figure 1.4 shows an example of this non-linear relationship between NO_x, VOCs, and ozone production as modelled in Mazzuca et al. (2016). Essentially increasing NO_x and VOC concentrations will increase ozone production; however, increasing one or the other may or may not increase production depending on current conditions. This is a short time scale relationship and ozone production can be more or less sensitive to VOCs at different hours of the day (Mazzuca et al. 2016). It is important to correctly determine the precursor concentrations in order to estimate ozone levels and production. This non-linear relationship is examined in more detail in the following section (1.3).

1.3 Volatile Organic Compounds

The least well understood precursors to tropospheric ozone production belong to a subclass of organic compounds. Organic compounds are a class of chemicals whose molecules contain carbon, with the exception of a few compounds such as carbides, carbonates, and simple oxides of carbon and cyanide. Organic compounds can be categorised based on their vapour pressure, which is the tendency of a liquid or solid to vaporise. Compounds with high vapour pressures at standard temperature are classed as volatile (volatile organic compounds: VOC), and are likely to vaporise at surface pressure. Atmospheric organic compounds are legion and differ by orders of magnitude with respect to their fundamental properties, such as volatility, reactivity, and cloud droplet formation propensity. **These properties are largely dictated by the chemical makeup of the individual compounds. A compound's atmospheric lifetime**

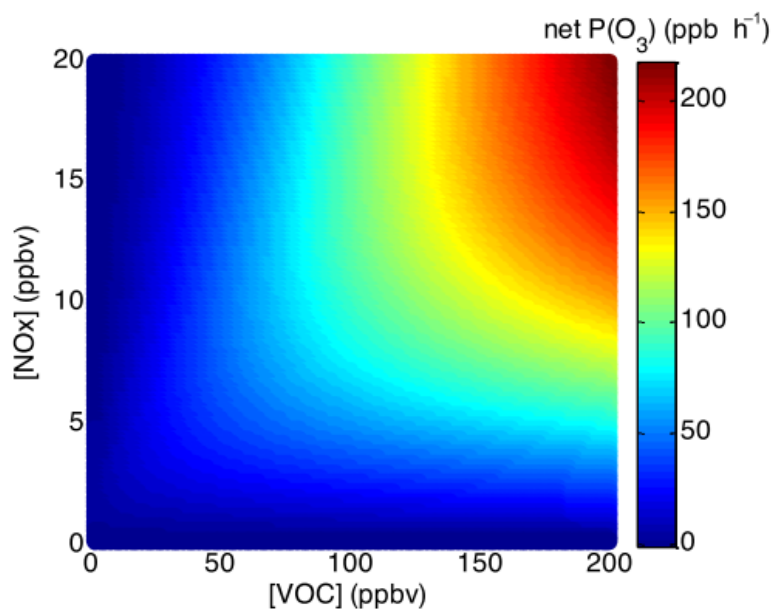


FIGURE 1.4: Dependence of ozone production rate on NO_x and VOC concentrations reproduced from Mazzuca et al. (2016).

is strongly related to its reactivity (and the concentration of reactants), with more reactive compounds having shorter atmospheric lifetimes.^{tb}

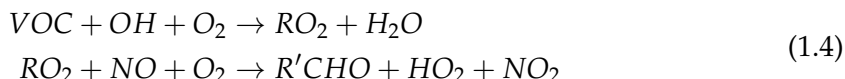
VOCs have vapour pressure greater than 10^{-5} atm, and are mostly generated naturally by plants, which emit around 1000 Tg yr^{-1} (Guenther et al. 1995; Glasius and Goldstein 2016). Due to their high volatility these compounds generally exist in the gas phase. Organic compounds with a lower volatility are classed as semi-volatile (SVOCs: vapour pressure between 10^{-5} and 10^{-11} atm) and are found in both gas and particle phase depending on temperature and pressure. Organic compounds with even lower vapour pressure are generally found in the particle phase (Glasius and Goldstein 2016). Plants contain tens of thousands of organic compounds, with fewer than 40 having high enough volatility to be emitted (Guenther et al. 2000). Gas phase compounds with higher vapour pressures can be oxidised into lower vapour pressure products that partition between gas and particle phase. For instance VOCs are oxidised in the atmosphere (mainly by OH), forming HCHO, O₃, CO₂ and many other species.

Understanding the drivers of trends in biogenic VOC emissions (BVOCs) is required in order to estimate future carbon fluxes, changes in the water cycle, ozone production, air quality, and other climate responses (Yue, Unger, and Zheng 2015). Other major emission sources of VOC (anthropogenic and pyrogenic) are also important.^{tb} For example, in China over the last 20 years, anthropogenic emissions of VOCs have been increasing while biogenic VOC emissions have decreased, due to rapid economic growth and lower annual temperatures (Stavrakou et al. 2014; Kwon et al. 2017). This thesis mostly focuses on biogenic emissions, with influences from pyrogenic and anthropogenic emissions removed (Section 2.7).^{tb}

Methane (CH₄) is one of the more abundant VOCs, however it is often classified

separately from non-methane VOCs (NMVOCs). NMVOCs include alkanes, alkenes, and aromatic hydrocarbons, with isoprene (an alkene) being the most abundant (Guenther et al. 1995). Methane is relatively long lived (years) and is well mixed in the atmosphere, while other VOCs have shorter lifetimes and therefore their concentrations are more spatially variable. VOCs with short lifetimes are generally only found in high concentrations near their emission sources.

In areas with high VOC concentrations, ozone production may be enhanced through the following reaction sequence (Sillman 1999):



with R and R' representing organic species. The reactions of VOCs with OH convert NO to NO₂, which leads to greater ozone formation as NO₂ production is bypassed in reaction 1 of Equation 1.3.

One aspect associated with VOC emissions is the production of aerosols. Aerosols are suspended particulates and liquid compounds in the atmosphere, often called particulate matter (PM). PM in the atmosphere is a major problem, causing an estimated 2-3 million deaths annually (Avnery et al. 2013; Hoek et al. 2013; Krewski et al. 2009; Silva et al. 2013; Lelieveld et al. 2015). Fine particulate matter (PM_{2.5}) penetrates deep into the lungs and is detrimental to human health. Some PM comes from small organic aerosols (OA) that are directly emitted to the atmosphere in the particulate phase, referred to as primary OA (POA).

A substantial amount of PM is due to gaseous organic compounds transforming into what is known as secondary OA (SOA) (Atkinson 2000; Kanakidou et al. 2005; Kroll and Seinfeld 2008). Formation of SOA is generally due to VOC oxidation and subsequent reactions, while removal from the atmosphere is largely due to wet or dry deposition, and cloud scavenging (Kanakidou et al. 2005). Most of the tropospheric SOA comes from biogenic precursors, and the evidence for this has grown over the last two decades (Guenther et al. 1995; Kanakidou et al. 2005; Guenther et al. 2012). Improved concentration estimates of these precursors requires a better understanding of their emissions, which is one of the foci in this thesis.

VOCs are removed mainly by photolysis and oxidation by OH, forming alkyl radicals (R'). Additional losses are caused by wet and dry deposition, reaction with NO₃, and ozonolysis (at night time or in polluted areas) (Atkinson and Arey 2003; Brown et al. 2009). Deposition only accounts for a small fraction of the VOC loss (Atkinson and Arey 2003).

1.3.1 Emissions

VOC emissions are classified as either biogenic (BVOC), anthropogenic, or pyrogenic. Global NMVOC emissions are estimated to come from (approximately) 85% biogenic, 13% anthropogenic, and 3% pyrogenic sources respectively (Kanakidou et al. 2005; Kefauver, Filella, and Peñuelas 2014). The ocean also plays a role in VOC emissions, with the Oceanic Niño Index showing positive VOC emission anomalies associated with neighbouring countries (Stavrakou et al. 2014). Due to the lack of in situ ground

based measurements, estimates of VOC emissions are uncertain, with large scale extrapolation required (Millet et al. 2006).

There is ten times as much mass of NMVOCs emitted from natural sources as from anthropogenic sources (Guenther et al. 2006; Kanakidou et al. 2005; Millet et al. 2006). Major emitters are broadleafs (notably Eucalyptus), and shrubs (Guenther et al. 2006; Arneth et al. 2008; Niinemets et al. 2010; Monks et al. 2015). NMVOC emissions are a byproduct of photosynthesis, and also a response to various environmental factors, including temperature, atmospheric CO₂, soil moisture, and drought stress. Land use changes can drastically affect isoprene (the dominant NMVOC) sources, for instance in the tropics where large scale deforestation has converted forest into crop lands (Kanakidou et al. 2005). This thesis focuses In this thesis I focus^{tb} on emissions of isoprene in Australia.

Globally around 710 - 1150 Tg C yr⁻¹ of BVOCs are emitted (Guenther et al. 1995; Lathière et al. 2006; Guenther et al. 2012; Messina et al. 2016). BVOCs are emitted by vegetation, with the most dominant emitters being tropical trees. The main VOCs emitted are isoprene (C₅H₈) (~ 50 – 70%), and monoterpenes (C₁₀H₁₆) (~ 30%), which have different emission amounts depending on the tree species(Guenther et al. 2012; Sindelarova et al. 2014). Other emissions include methanol (CH₃OH), ethanol (C₂H₆O), acetaldehyde (CH₃CHO), acetone ((CH₃)₂CO), ethene (C₂H₄) and propene (C₃H₆) (Guenther et al. 2012). Many of these estimates come from Model of Emissions of Gases and Aerosols from Nature (MEGAN), a bottom-up biogenic emissions model. MEGAN parameterises BVOC emissions as a function of temperature, land cover, plant functional type, etc., with descriptions given in Guenther et al. (2012).^{tb}

1.3.2 Biogenic emissions modelling

Biogenic emissions models generally take what is termed a bottom up approach, where the environment is simulated and then the emissions from that environment is estimated based on its interaction with the weather. The most important parameters dealing with VOC emissions are leaf area index, emission factors, plant functional type, and light density fraction (Messina et al. 2016). The estimated emission factors are built up from measured plant emissions, which can be measured from downwind (e.g., Nguyen et al. 2014) or from within a chamber (e.g., Paulot et al. 2009b; Nguyen et al. 2014). There are several models that estimate VOC emissions, such as MEGAN (created and published by (Guenther et al. 1995), with subsequent updates in Guenther et al. (2000), Guenther et al. (2006), and Guenther et al. (2012)), LPJ-GUESS (Lund-Potsdam-Jena General Ecosystem Simulator) (Arneth et al. 2007), and ORCHIDEE (Organising Carbon and Hydrology in Dynamic EcosystEm) (Messina et al. 2016). Many of the available bottom-up models have inputs and sensitivities similar to those of MEGAN. MEGAN is used within this thesis as a module within a chemical transport model (Section 2.3.4).^{tb}

There is a potential issue caused by shared underlying algorithms and assumptions between different emission models, which lead to an unrealistic convergence on isoprene emission estimation (Arneth et al. 2008). MEGAN can depend greatly on parameterised inputs such as temperature, sunlight, plant type, plant coverage, plant health, etc. (Arneth et al. 2008; Niinemets et al. 2010). Sensitivity to these factors is pervasive in bottom up emissions models (e.g., Marais et al. 2014; Miller et al.

2014; Messina et al. 2016). Relatively few Australian species are used within MEGANs plant functional type parameterisations, and those that are listed may be poorly represented (Emmerson et al. 2016). This leads to increased uncertainty for Australian emissions. Additionally there is uncertainty around the soil moisture parameterisations, with Australian isoprene emissions highly sensitive to the value and handling of this parameter (Sindelarova et al. 2014; Emmerson et al. 2019). Modelled emissions are sensitive to soil moisture, especially near the wilting point, below which trees stop emitting isoprene and other VOCs completely as they can no longer draw water (Bauwens et al. 2016).^{tb}

1.3.3 Isoprene

Isoprene (2-methylbuta-1,3-diene) is the dominant BVOC emitted to the atmosphere. It is of major importance to the atmosphere, as it is involved in various processes that alter the oxidative capacity of the atmosphere. Isoprene affects NO_x and HO_x cycling, see for example reactions 1.1, 1.3. In the presence of NO_x , isoprene forms tropospheric ozone and SOA (Wagner 2002; Atkinson and Arey 2003; Millet et al. 2006; Patchen et al. 2007). It has a short lifetime during the day, roughly an hour due to OH oxidation (Atkinson and Arey 2003). Ozonolysis and photolysis are lesser oxidation pathways, which can form similar products (Nguyen et al. 2016; Wolfe et al. 2016).

Measurements of isoprene are often uncertain, as the compound is reactive and short lived. Chamber experiments are used to determine how isoprene behaves once it is emitted into the atmosphere; however, laboratory derived reaction rates may be unsuitable when modelling the natural atmosphere, as natural air masses frequently differ from air masses used in chambers (Kanakidou et al. 2005; Nguyen et al. 2014). In the absence of extensive measurements, isoprene emissions and subsequent atmospheric oxidative chemistry are often modelled. MEGAN and other models(Guenther et al. 1995), and subsequent updates (Guenther et al. 2000; Guenther et al. 2006; Guenther et al. 2012),^{tb} have been used throughout the atmospheric community to make global estimates of isoprene emissions, at roughly 500-600 Tg yr⁻¹, emitted mostly during the day. Australia has increased uncertainty (relative to globally) due to its lack of measurements and study (see Section 1.3.2). Other models also exist which estimate similar isoprene amounts, such as LPJ-GUESS (Lund-Potsdam-Jena General Ecosystem Simulator) (Arneth et al. 2007), and ORCHIDEE (Organising Carbon and Hydrology in Dynamic EcosystEm) (Messina et al. 2016). There is a potential issue caused by shared underlying algorithms and assumptions between the models, which lead to an unrealistic convergence on isoprene emission estimation (Arneth et al. 2008). The global emission factors used to derive these estimates are based on modelling emissions from different plant species (phenotypes), and relatively few Australian species were used when forming these estimates. This leads to increased uncertainty for Australian emissions.^{tb} Due to the highly reactive nature of isoprene, modelling of related chemical products is sensitive to uncertainties, for example the diurnal pattern of isoprene emissions affects modelled ground level ozone (Fan and Zhang 2004; Hewitt et al. 2011). The global uncertainty of isoprene emission was estimated to be a factor of 2 to 5 (250-750 Tg yr⁻¹) (Kanakidou et al. 2005). Improvements over the years have been incremental, and generally localised to regions of particular interest for air quality such as China and the USA (Guenther et al. 2012; Jiang et al. 2018).

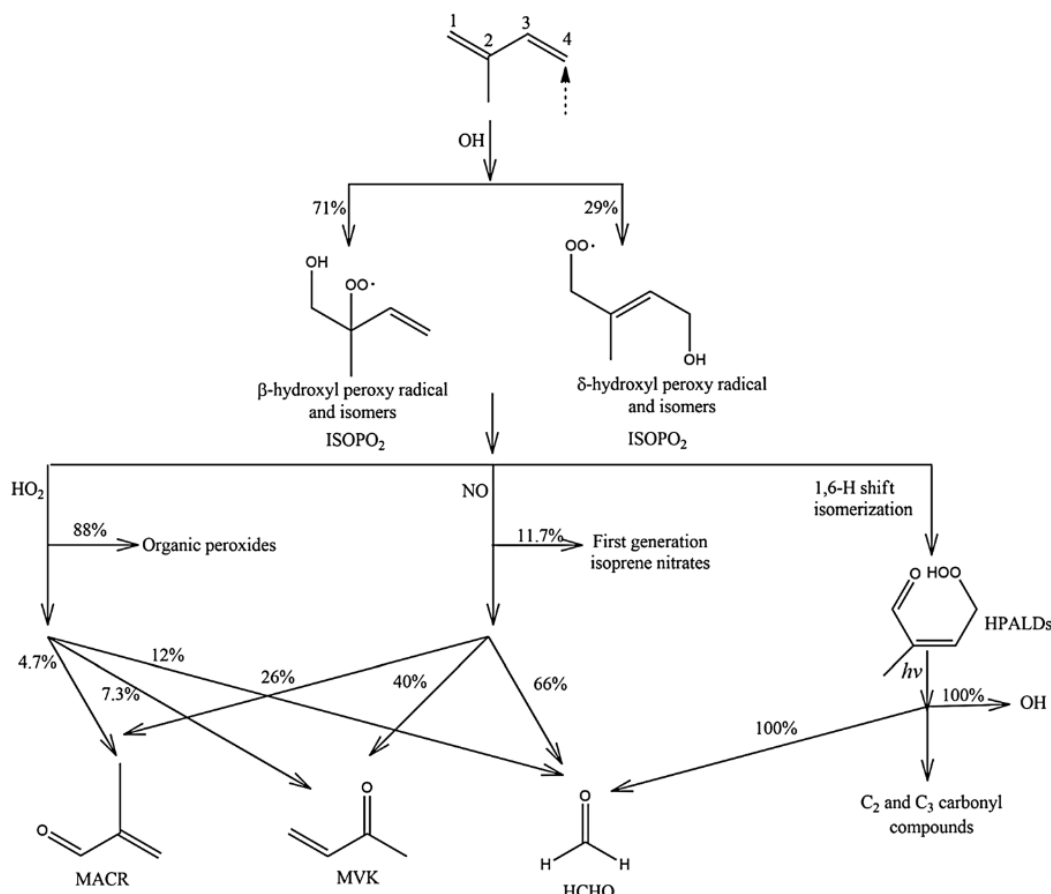
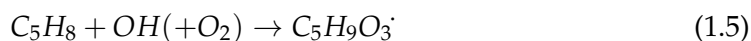


FIGURE 1.5: Simplified isoprene products following oxidation by OH, reproduced from Mao et al. (2013).

1.3.4 Isoprene chemistry

Isoprene is emitted and enters the atmosphere in the gas phase, where it reacts quickly with OH and other radicals. One common compound that is produced by these reactions is HCHO, which can be measured from satellites and is often used to estimate how much isoprene is being emitted. Isoprene reacts with OH, ozone, or NO_x, leading to organic peroxy radicals (ROO[·]). These go on to form many products and lead to (amongst other things) aerosol, formaldehyde, and ozone formation, depending on sunlight and NO_x concentrations (Atkinson 2000).

Figure 1.5 shows the first stages of oxidation of isoprene by OH. The primary first step for atmospheric isoprene is photooxidation, reacting with OH to form isoprene hydroxyperoxy radicals (ISOPPOO: C₅H₉O₃, a subset of ROO[·]), and is shown in Equation 1.5 (Patchen et al. 2007; Wolfe et al. 2016; Marvin et al. 2017).



Different isomers are formed based on which carbon the OH adducts to. The subsequent processes that begin with isoprene oxidation are often called the isoprene (photochemical) cascade (e.g., Crounse et al. 2012; Paulot, Henze, and Wennberg 2012; Wolfe et al. 2016).

ISOPOO reacts with HO₂ or NO, producing stable products. This pathway also produces HCHO (with varying yields):



During the day HCHO has a lifetime of 1-2 hrs, while ISOPOO lasts ~ 100 s, making reaction 1.5 a rate limiting factor in HCHO production (Wolfe et al. 2016). Additionally, ISOPOO can isomerise and produce hydroperoxy-methyl-buteneals (HPALDS) (see figure 1.5), which also leads to HCHO. At higher NO mixing ratios (at least a few hundred pptv), ISOPOO react mostly with NO. At low NO (less than 50 pptv), ISOPOO is more likely to either isomerise, react with HO₂, or react with another ROO.

There is uncertainty about which pathways are most important following ISOPOO production, affecting predictions by atmospheric models (Nguyen et al. 2014). This limits understanding of the relative importance of some chemical processes, such as auto-oxidation of ISOPOO (Crounse et al. 2013). The reaction pathways depend on local concentrations of NO_x: the high and low NO_x pathways are dominated by NO and HO₂ reactions respectively. HO₂ reactions predominantly produce hydroxyhydroperoxides (ISOPOOH), while NO reactions produce isoprene nitrates (ISOPN) (Crounse et al. 2006). If measured, first generation ISOPN and ISOPOOH products can be used to determine the portion of isoprene oxidation following each pathway (e.g., Yu et al. 2016). Globally around one third of ISOPOO react with HO₂, and two thirds react with NO (Paulot et al. 2009b). Most of these reaction pathways produce HCHO; however, the rate of production differs between different pathways, along with that of methyl vinyl ketone (MVK), and methacrolein (MACR), which can then be used to estimate reaction regimes (Marais et al. 2012; Liu et al. 2016b; Wolfe et al. 2016).

1.3.4.1 High NO_x pathway

In the presence of NO_x, ISOPOO reacts with NO and forms ISOPN, which affect levels of both HO_x (OH+HO₂) and NO_x. ISOPN generally act as a sink of HO_x, and can be a sink or reservoir for NO_x (Mao et al. 2013; Fisher et al. 2016). A portion of the ISOPN are recycled back to NO_x, serving as a reservoir of nitrogen and allow its transport to the boundary layer of remote regions (Patchen et al. 2007; Paulot et al. 2009a). The nitrates can also build up in the winter, when removal processes are not as dominant (Lelieveld et al. 2009).

Under high NO_x conditions there is a large and rapid yield of HCHO, with most of the ultimate HCHO production occurring within one day (Palmer et al. 2006). First generation ROO react with NO yielding MVK(~ 40%), MACR(~ 26%), and HCHO(~ 60%) which is higher than yields after reaction with OH (Liu et al. 2013; Mao et al. 2013). The MVK and MACR products form additional HCHO within a few hours due to oxidation by OH (Palmer et al. 2006).

1.3.4.2 Low NO_x pathway

In low NO_x environments, ISOPOOH is formed in yields > 70%, while MACR, MVK, and HCHO are formed at ~ 5%, ~ 7%, and ~ 12% respectively (Paulot et al. 2009b; Mao et al. 2013). This ISOPOOH mostly reacts with OH to form dihydroxyperoxides (IEPOX) while regenerating OH (Mao et al. 2013). This pathway has lower and slower ultimate yields of HCHO from isoprene when compared to the high-NO_x pathway (Palmer et al. 2006).

Isoprene oxidation and subsequent reactions are less well understood when lower concentrations of NO are present in the atmosphere. It was thought that in low NO environments, like those far from anthropogenic pollution and fires, oxidation of isoprene would create ISOPOOH and reduce local concentrations of OH and HO₂ (Guenther et al. 2000; Paulot et al. 2009b). However this reduction was not seen in measurements and HO_x levels have been shown to be largely unaffected by isoprene concentrations (Paulot et al. 2009b). HO_x is recycled through IEPOX, formed from ISOPOOH oxidation, and some HO_x is produced in the formation of MACR and MVK (Paulot et al. 2009b). Though uncertain, OH and HO₂ production or regeneration mechanisms have improved model outcomes when compared against campaigns (Peeters and Muller 2010; Crounse et al. 2012).

Uncertainties and bias from measurements have made it more difficult to understand what happens in low NO_x conditions, and many observations of OH remain under-predicted in models (Mao et al. 2012). Due to OVOC interference, measurements in low NO_x environments can lead to massively overestimated MVK and MACR yields (Nguyen et al. 2014). Nguyen et al. (2014) show preliminary estimates of low-NO yields of MVK and MACR to be 6±3% and 4±2% respectively, consistent with Liu et al. (2013), but only when cold-trapping methods are employed. Many instruments have been shown to generate OH internally, creating anomalous VOC readings due to within-instrument oxidation (Mao et al. 2012).

Improved understanding of both the chemistry and instrument sensitivities has helped closed the gap between model predictions and detected concentrations of VOCs and OH (Mao et al. 2012), but uncertainties remain in isoprene oxidation mechanisms. Examples (taken from Nguyen et al. (2014)) include:

- isoprene nitrate yields, which range from 4-15% (Fisher et al. 2016)
- 90% disagreements in MACR and MVK yields (Liu et al. 2013)
- unknown HPALD fates (Peeters, Nguyen, and Vereecken 2009; Crounse et al. 2013)
- poorly-characterised RO₂ lifetime (Wolfe et al. 2012).

1.3.4.3 Night time processes

At night when OH concentrations have dropped, isoprene can remain in the atmosphere. Typically less than half of this night time isoprene is removed through ozonolysis (Atkinson and Arey 2003). A build up of NO₃ radicals can be seen at night, when photolysis is not removing them (Atkinson 2000; Brown et al. 2009). This build up is

enhanced in polluted (high NO_x) areas. NO_3 are largely formed through ozone reactions. In these conditions isoprene is consumed by NO_3 radicals that join to one of the double bonds, producing organic nitrates (RONO_2) in high yield (65% to 85%) (Mao et al. 2013).

In areas with high NO_x levels, greater than 20% of the isoprene emitted late in the day ends up being oxidised by the NO_3 radical overnight (Brown et al. 2009). At night isoprene affects both NO_x concentrations and ozone levels, and can form harmful organic nitrates and SOA (Brown et al. 2009; Mao et al. 2013). These nitrates go on to produce further SOA, largely due to NO_3 reacting with first generation isoprene oxidation products (Rollins et al. 2009). The night-time concentrations of OH and ozone also have a complex effect on NO_x removal in high latitude winters, when photolysis and NO reactions are reduced (Ayers and Simpson 2006).

1.3.5 Radiative Forcing

Another reason for interest in VOCs is that they are a dominant source of organic aerosol, which are a major source of uncertainty in radiative forcing. VOC emissions affect ozone along with several atmospheric parameters that directly and indirectly alter radiative forcing rates (e.g., Arneth et al. 2008). This is even more important in Australia where VOCs are so poorly represented by contemporary modelling (Emmerson et al. 2016). Aerosols are particles in the atmosphere, and they affect radiative forcing in ways that are difficult to accurately quantify. For some years it has been understood that aerosols have an overall cooling effect within the atmosphere. Smaller particles can match the wavelengths of visible light, interfering with incoming radiation (Kanakidou et al. 2005). Aerosol products from gas phase emissions (or the children thereof) also play an indirect and complex role in cloud properties, with a net cooling effect (Kanakidou et al. (2005), Stocker et al. (IPCC, 2013: *Climate Change 2013: The Physical Science Basis. Contribution of Working Group I to the Fifth Assessment Report of the Intergovernmental Panel on Climate Change*, Chapter 7, 8)). Aerosol and cloud formation remain as large uncertainties in recent IPCC reports (Forster et al. 2007). Figure 1.6 shows that uncertainty from aerosol effects dominate the uncertainty in radiative forcing.

1.4 Formaldehyde

In conjunction with atmospheric chemistry and radiative models, satellite measurements quantify the abundance of HCHO in the atmosphere. Isoprene is hard to measure directly due to its short lifetime and weak spectral absorption, instead HCHO is often used as a proxy (Millet et al. 2006; Fu et al. 2007; Dufour et al. 2008; Marais et al. 2012; Bauwens et al. 2013; Kefauver, Filella, and Peñuelas 2014; Bauwens et al. 2016; Surl, Palmer, and Abad 2018). The existence of satellite data covering remote areas provides an opportunity to improve VOC emissions estimates leading to more robust models of global climate and chemistry. This method is implemented within this thesis (Section 3.2), and relevant information dealing with HCHO is provided here.

Formaldehyde (HCHO), also known as methanal, methyl aldehyde, or methylene oxide, is part of the aldehyde family. HCHO is an oxygenated VOC that is toxic,

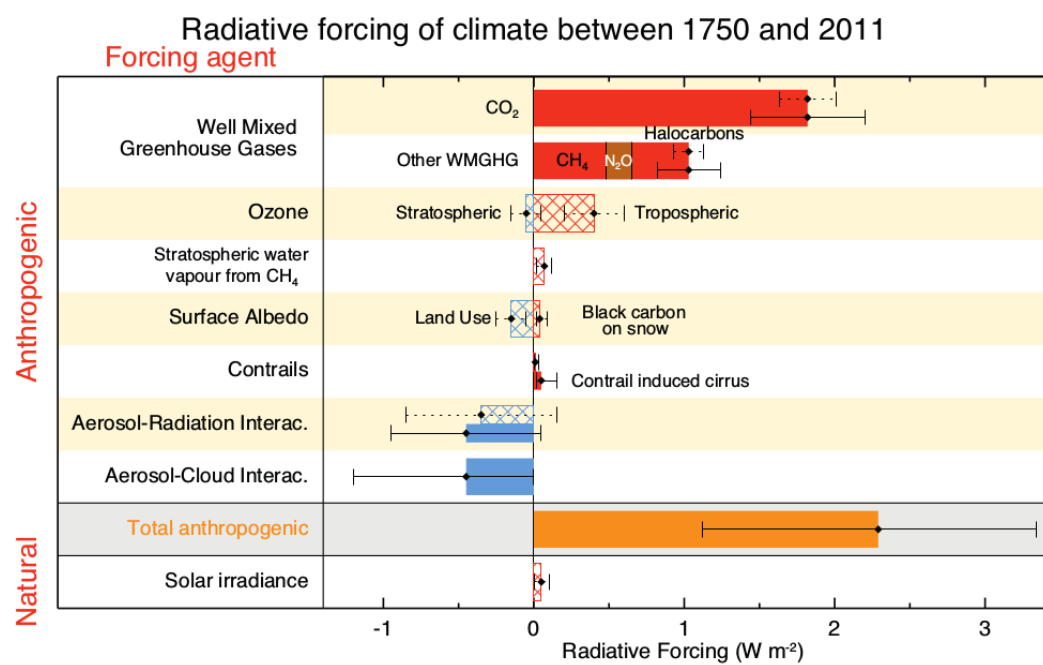
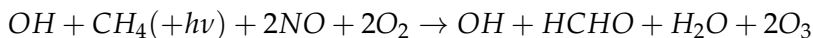


FIGURE 1.6: The overall radiative forcings and uncertainties of several atmospheric constituents. Reproduced from Stocker et al. (*IPCC, 2013: Climate Change 2013: The Physical Science Basis. Contribution of Working Group I to the Fifth Assessment Report of the Intergovernmental Panel on Climate Change*), chapter 8.

allergenic, and a potential carcinogen. Generally, HCHO is not dangerous at low background atmospheric levels. Globally, HCHO production is mainly due to the oxidation of methane; however, over continental regions, HCHO enhancement above the background level is largely due to isoprene emissions. HCHO production also depends on NO_x concentrations, which affect the yield from isoprene oxidation. Isoprene reactions yield more HCHO in the high-NO_x pathway (compared to the low-NO_x pathway) (Marais et al. 2012). HCHO measurements are often used to evaluate how well isoprene chemistry is simulated by models, as HCHO levels depend on initial VOCs and oxidants (Marvin et al. 2017).

1.4.1 Sources and sinks

Background levels of HCHO in the atmosphere are driven by the oxidation of CH₄ by the OH, which produces $\sim 970 \text{ Tg yr}^{-1}$ (Fortems-Cheiney et al. 2012). Atkinson (2000) summarised the background formation of HCHO with the following reaction:



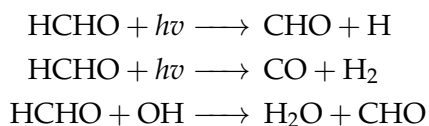
This shows that photolysis and oxidation of methane forms HCHO and ozone in a process that regenerates the OH radicals. CH₄ concentrations are relatively well constrained in models, with the Atmospheric Chemistry and Climate Model Inter-comparison Project showing only $\sim 3\%$ inter-quartile range (Young et al. 2013).

Within the continental boundary layer, HCHO is enhanced above background levels due to NMVOC emissions reacting with OH radicals in the presence of NO_x (Wagner 2002; Millet et al. 2006; Kefauver, Filella, and Peñuelas 2014). The total contribution from NMVOC oxidation is $\sim 358 \text{ Tg yr}^{-1}$ (Fortems-Cheiney et al. 2012). Enhancements to regional and continental HCHO are largely driven by emissions of isoprene (Guenther et al. 1995; Palmer et al. 2003; Shim et al. 2005; Kefauver, Filella, and Peñuelas 2014). The exception is where emissions of HCHO or precursors occur due to fires or anthropogenic activities such as fossil fuel combustion, natural gas flaring, ethanol refining, and agricultural activity (Guenther et al. 1995; Kefauver, Filella, and Peñuelas 2014; Wolfe et al. 2016). Other terpenoids (monoterpenes, sesquiterpenes, etc.) can also produce HCHO, although generally to a lesser extent than isoprene, methane and biomass burning (Guenther et al. 2012). Anthropogenic sources of HCHO are largely negligible; however, their signals can be seen in very large cities or near large industrial sources (Millet et al. 2008; Zhu et al. 2014).

In the past, HCHO levels were underestimated by models, often with large discrepancies, due to the poor understanding of methyl peroxy radical (CH₃OO) chemistry (Wagner 2002). Now HCHO concentrations are better understood, however precursor emissions are one of the main unknowns (e.g., Emmerson et al. 2016; Marvin et al. 2017). Another source of discrepancy between modelled and measured HCHO concentrations is second and later generational isoprene oxidation chemistry (Marvin et al. 2017).

HCHO has two major sinks totalling $\sim 1210 \text{ Tg yr}^{-1}$, reactions with OH (oxidation), and photolysis (Levy 1972; Crutzen, Lawrence, and Poschl 1999; Wagner 2002; Fortems-Cheiney et al. 2012; Kefauver, Filella, and Peñuelas 2014). The other sinks are

wet and dry deposition, although these are not as significant ($\sim 32 \text{ Tg yr}^{-1}$) (Atkinson 2000; Fortems-Cheiney et al. 2012). Oxidation and photolysis reactions begin as follows (Ayers et al. 1997):



These reactions lead to a daytime lifetime of a few hours (Atkinson 2000; Millet et al. 2006). Both these loss processes (photolysis, oxidation) form CO, and lead to production of hydroperoxyl radicals (HO_2). These products have global significance to radiative forcing and oxidative capacity (Franco et al. 2015).

1.4.2 Measurement techniques

HCHO measurements are used extensively throughout this thesis, and a brief introduction to the relevant techniques is provided here. HCHO data used in this thesis have been measured using two different techniques: Fourier Transform Infra-Red (FTIR) Spectrometry and Differential Optical Absorption Spectroscopy (DOAS). FTIR uses the Fourier transform of a measured spectrum to quantify species which interfere with the spectrum in the infra-red region. DOAS methods are based on light interference and absorption through air masses.

The DOAS technique takes advantage of the optically thin nature of HCHO in order to linearise the radiance differential through air masses with and without HCHO, using the Beer-Lambert intensity law. This method is used globally both from ground-based and space-based instruments for HCHO detection (Guenther et al. 1995; Gonzalez Abad et al. 2015; Davenport et al. 2015). As a trace gas, HCHO absorbs light over a few wavelength bands, which allows instruments to detect concentrations between a known light source and a detector. Figure 1.7 shows the interference spectrum of HCHO along with a typical band used to examine interference in the DOAS technique. FTIR and DOAS measurements have a range of uncertainties, including systematic and random measurement errors and uncertain a priori shape factors and water vapour profiles (e.g., Franco et al. 2015). One difficulty is that this interference is relatively small (HCHO is optically thin) and other compounds absorb light at similar wavelengths (Davenport et al. 2015).

Other types of measurement involve directly measuring the air, and determining chemical compounds through their physical properties such as by mass spectrometry analysis of mass to charge ratios (m/z) of ionised air masses. Two examples of this include proton transfer reaction mass spectrometers (PTR-MS), and gas chromatography mass spectrometers (GC-MS). These instruments can be also used to determine the gas phase evolution of other isoprene and monoterpene products (e.g., Lee et al. 2006; Nguyen et al. 2014; Wolfe et al. 2016; Lerner et al. 2017). Reasonable agreements between different instruments and techniques can be achieved, although titration and calibration differences can lead to large ($\sim 30\%$) discrepancies (e.g., Hak et al. 2005). These differences and non-uniformity between measurements (even among identical

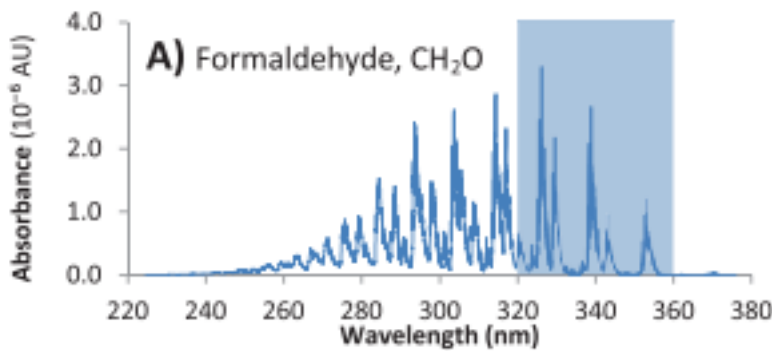


FIGURE 1.7: HCHO spectrum, with a typical band of wavelengths used for DOAS path measurements. Reproduced from Davenport et al. (2015).

instruments) are part of the reason HCHO does not have a consistent network for global measurements like those for greenhouse gases or ozone (Fortems-Cheiney et al. 2012).

1.4.2.1 Satellite measurements

Satellites remotely sense atmospheric HCHO through irradiance measurements of solar light that has reflected off the earth's surface. These irradiances are affected by gases that absorb radiation along the reflected path of light between the detector, earth, and sun. The irradiance is then used to estimate how much of a particular gas exists along this path, which gives an estimate called the slant column. The retrieved slant column of a particular gas (species) can be transformed into a vertical column by scaling the path length in conjunction with accounting for the light scattering properties of the trace gas. The scaling coefficient created to transform from slant to vertical column is called the Air Mass Factor.

Several satellites provide long term HCHO observations with near complete global coverage. Some of these are:

- ERS-2 launched in April 1995, housing the GOME ultraviolet and visible (UV-Vis) spectrometer
- AURA launched in July 2004, housing the OMI UV-Vis spectrometer
- MetOp-A and B launched in October 2006 and September 2012 respectively, both housing a GOME-2 UV-Vis spectrometer.

These satellites are on low earth orbit trajectories and overpass any area up to once per day. Satellites use DOAS techniques (Section 1.4.2.2) with radiative transfer calculations on solar radiation absorption spectra to measure column HCHO. An example of a spectrum retrieved from the GOME-2 instrument is given in figure 1.8.

Satellite observations often require both remote-sensing and in situ measurements combined with modelled data for validation (Marais et al. 2014). There is less information available from satellite measurements at higher latitudes due to increased error in measurements over the more slanted column paths (De Smedt et al. 2015). Validation

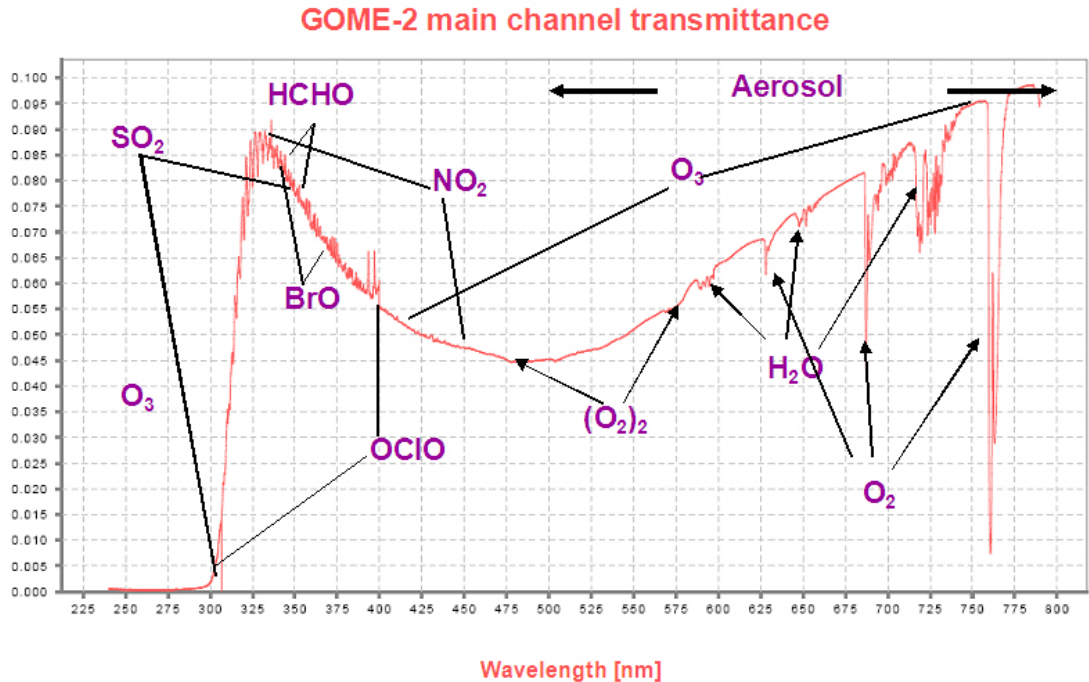


FIGURE 1.8: An example spectrum showing absorption features used for species concentration measurements by GOME-2. Image reproduced from EUMETSAT and ESA (EUMETSAT 2015).

is important due to the various uncertainties in the satellite remote sensing process. This can be done using aircraft data to provide model validation (e.g., Zhu et al. 2016). Satellites use an assumed shape factor to improve the vertical column estimate; however, this can lead to a bias between satellite data and other measurements (Zhu et al. 2016). Different satellites, instruments, or techniques that measure HCHO (or any trace gas) can give different results due to differing a priori assumptions (Lorente et al. 2017). The concept of differences that arise between datasets based on measurement techniques or underlying instrument biases is called structural uncertainty.

1.4.2.2 DOAS

The DOAS technique uses solar radiation absorption spectra to measure trace gases through paths of light. Beer's law states

$$T = I / I_0 = e^{-\tau} \quad (1.7)$$

with T being transmittance, τ being optical depth, and I, I_0 being radiant flux received at instrument and emitted at source respectively. The Beer-Lambert law of extinction allows spectroscopic measurement of absorbing chemical species (absorbers) in the atmosphere:

$$I_B = I_{B_0} e^{-\tau_s} \quad (1.8)$$

where I_B , I_{B_0} is backscattered intensity with and without the absorber respectively, and τ_s is the optical thickness of the absorber along the measured path between source and instrument.

τ can be described using the scattering and absorption cross section area (α , cm^2) and density (η , molec cm^{-3}) of an absorber as follows:

$$\tau = \int \alpha(s) \eta(s) ds \quad (1.9)$$

Here τ represents the sum of optical thicknesses of each absorber within the measured path (s) through a medium. Substituting Equation 1.9 into Equation 1.8 leads to

$$I = I_0 \exp \left(\sum_i \int \eta_i \alpha_i ds \right) \quad (1.10)$$

Where i represents a chemical species index, and the integral over ds represents integration over the path from light source to instrument.

Another way of describing optical depth (also called optical thickness) is the natural logarithm of the ratio of incident radiant power to transmitted radiant power through a material (from Equation 1.8). In the atmosphere, the optical depth of various chemical species can be determined using incoming solar radiation. we are interested in the optical depth of various chemical species, and we use incoming solar radiation to determine this.^{mh} The difference between solar radiation at the top of the atmosphere and the earth's surface defines the atmospheric optical depth along the path of observation.

$$\tau = \ln \frac{\phi_e^i}{\phi_e^t} \quad (1.11)$$

where ϕ_e^i is radiant flux at the surface, ϕ_e^t is the solar radiant flux that arrives at the top of the atmosphere. In the atmosphere, optical depth can be due to several factors including scattering, chemical absorbance, and aerosols.

1.5 Atmospheric Chemistry Modelling

Models can fill the gaps (both spatial and temporal) in measurement records, and ~~can help us~~^{mh} improve ~~peoples our~~^{mh} understanding of the natural world. For example, they can be used to examine future outcomes resulting from changing ~~our~~^{mh} emissions. They can be used to increase measurement accuracy (for instance in satellite measurements) and determine where ~~information is lacking we lack information~~^{mh}, while also evaluating the performance of new instruments. Precisely representing various chemicals and reactions in the atmosphere allows efficient mitigation of pollution, since proposed scenarios can be compared against one another. Currently, models require improved isoprene emissions and subsequent chemistry for effective air quality determination (Marvin et al. 2017).

1.5.1 Box models

Box models simulate chemistry in a singular set of conditions without transport or spatial gradients. These models often parameterise things such as transport and emissions that would realistically take place at the edges of the box. Box models can be used to test chemical mechanisms in specific scenarios, such as high or low NO_x environments. For example, Marvin et al. (2017) used a box model matching conditions in southeast USA to evaluate isoprene mechanisms from several models.

By allowing for interactions between boxes this concept can be extended to multiple-box models. Multiple-box models are simply multiple instances of single boxes with the addition of transport between them. Transport requires meteorological fields such as wind velocities and turbulence. The meteorology fields can be modelled, and/or input as parameters.

1.5.2 Chemical transport models

Chemical transport models (CTMs) provide a simulation of chemical densities and transport over time, through the atmosphere. Chemistry in the atmosphere is a complex system of coupled reactions and dynamics, which can be solved using numerical partial differential equation solvers. Chemical models require many inputs such as meteorological conditions and emissions. Initial (atmospheric starting state) and boundary (inputs and outputs at the edge of the modelled system) conditions are required, and models or inventories of emissions often make up inputs at the surface of the atmosphere.

CTMs simulate production, loss, and transport of chemical species. This is generally calculated using one or both of the Eulerian (box) or Lagrangian (puff) frames of reference. Eulerian models use equations of chemistry within and transport between volumes in a gridded spatial coordinate system, while Lagrangian models evaluate behaviour within a potentially changing frame of reference (for example within a cloud). CTMs normally solve continuity equations simultaneously for many coupled species. The continuity equations describe transport of a conserved quantity such as mass or energy, which, solved together with production and loss of a chemical can provide detailed simulations of natural processes.

The general continuity equation links a quantity of a substance (q) to the field in which it flows and can be described by the formula:

$$\frac{\partial \rho}{\partial t} + \nabla \cdot j = \sigma$$

where ρ is density of q in the field, t is time, ∇ is divergence, j is the flux (q per unit area per unit time entering or leaving the field), and σ is the generation or loss of q per unit volume per unit time.

The type of model best suited to modelling the entire earth uses the Eulerian frame of reference, where the atmosphere is broken up into 3-D boxes with densities and transport calculated and stored for sequential steps in time at each location. The mass

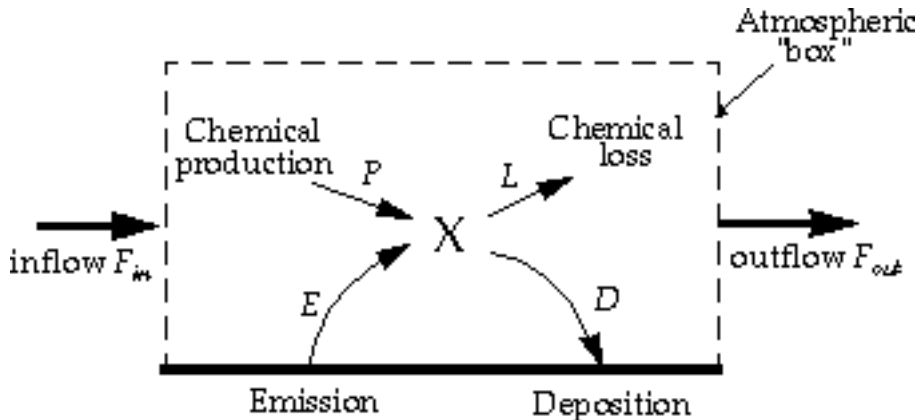


FIGURE 1.9: Standard box model parameters, reproduced from Jacob (1999).

balance equation must be satisfied in any realistic long term model and is as follows:

$$\begin{aligned}\frac{dm}{dt} &= \sum \text{sources} - \sum \text{sinks} \\ &= F_{in} + E + P - F_{out} - L - D\end{aligned}$$

where m is mass of a chemical, E and D are emission and deposition, P and L are production and loss, and F is chemical transport in and out, as shown in figure 1.9. Any large chemical model will solve this mass balance equation over highly coupled arrays of partial differential equations, which becomes computationally expensive as complexity increases.

Contemporary models generally use mathematical differential solving tools of various complexity (often called chemical mechanisms) to solve chemical equations in order to predict chemical species evolution over time. Different solvers may be slower or faster, and some are more suited to particular situations. The choice of chemical mechanism is normally driven by the mathematical properties of the equations and systems being modelled (such as stability and stiffness), as well as limitations around processing power. Grouping together subsets of model equations or chemical species is often performed and it is possible to use different solvers on each grouping. For example: since $[O] \ll [O_3]$ the chemical family O_X ($O_X \equiv O + O_3$) can be used to simplify chemistry simulations and approximate O_3 concentrations (Brasseur and Jacob 2017, Chapter 3). Different chemical mechanisms may find different solutions to the same problems, due to how the numerical solvers are implemented, which can affect model output (Zhang et al. 2012).

1.5.3 Emissions

The general formula governing modelled emissions E for a species i (from Brasseur and Jacob (2017)) is as follows:

$$E_i = A \times EF_i \times S_i \quad (1.12)$$

with A the activity rate, EF_i being the emission factors, and S_i is a scaling factor accounting for meteorology and other effects not included in A or F (e.g., seasonal temperature). For example, to estimate isoprene emission E_{isop} per second for an area, the equation becomes $A = \text{how many trees in an area multiplied by } EF_{isop} = \text{isoprene emitted per tree per second multiplied by } S_{isop}$ = a scaling factor based on temperature and soil moisture. This is a simplified example of a bottom-up estimate, one commonly used technique for estimating isoprene emissions. Bottom-up emission estimates use information about the flora that emit isoprene, along with the rates of emissions and meteorological parameters that affect these rates. The other common emission estimation technique is termed top-down. Top-down emissions estimates are derived from measurements of the child products of emitted VOCs. For example, GOME satellite HCHO and a Bayesian inversion technique have been used to estimate isoprene emissions of $\sim 566 \text{ Tg C yr}^{-1}$ globally (Shim et al. 2005).

1.5.4 Uncertainties

This section summarises the major uncertainties models have in relation to VOCs, and ozone. Atmospheric chemical models by necessity use simplifications of real world processes, and also utilise information that may be itself uncertain or extrapolated. Uncertainty is introduced through both of these channels as well as through computational limitations.

1.5.4.1 Emissions Inventories

Model results can be greatly affected by the choice of emissions inventory used to provide boundary conditions. Natural (biogenic or pyrogenic) and anthropogenic emissions often drive a large fraction of atmospheric oxidation and radical chemistry, especially in the continental boundary layer. Emissions inventories have been found to be reliable at larger (regional to global) scales, as long as they are derived from accurate input measurements (Zeng et al. 2015). Modelled ozone concentrations have been found to be sensitive to isoprene emissions and NO_x sources, both of which are uncertain within approximately a factor of 2 (Christian, Brune, and Mao 2017). Bottom up inventories of BVOCs (Section 1.3.2)^{tb} remain largely uncertain due to missing or extrapolated plant functional type information, changing land cover, and parameterised environmental stressors (Guenther et al. 2000; Kanakidou et al. 2005; Millet et al. 2006). Global emissions inventories like MEGAN often implement data extrapolation, which also introduces uncertainties (Miller et al. 2014).

Modelled surface ozone may be overestimated if NO_x emissions are too high, due to their affects on the oxidative capacity of the atmosphere (Travis et al. 2016). NO_x and isoprene emissions have been shown to be the most significant sources of uncertainty for ozone concentrations near the surface over the US, while isoprene-derived products and lightning NO_x drives uncertainty in the upper atmosphere (Christian, Brune, and Mao 2017).

Estimates of isoprene emission are based on a few algorithms that ~~may be heavily influenced by parameterised inputs (see Section 1.3.2). can depend greatly on parameterised inputs such as temperature, sunlight, plant type, plant coverage, plant health, etc. (Arneth et al. 2008; Niinemets et al. 2010).~~^{tb} Sensitivity to these factors is pervasive in

bottom up emissions models (e.g., Marais et al. 2014; Miller et al. 2014; Messina et al. 2016). Arneth et al. (2008) argue that the monopoly of isoprene emission estimates may be leading us^{mh} to an incorrect understanding of isoprene chemistry. VOC emissions form an integral part of many chemistry models, and poor characterisation of these can lead to many more problems in other models (e.g., Yue, Unger, and Zheng 2015). Models that depend on VOC emissions acquire the uncertainties and sensitivities (for example, to light and temperature parameters) found in VOC emissions (Yue, Unger, and Zheng 2015). This can be mitigated where measurements are used to constrain parameters (e.g., Stavrakou et al. 2014). ~~Modelled emissions are sensitive to soil moisture, especially near the wilting point, below which trees stop emitting isoprene and other VOCs completely as they can no longer draw water (Bauwens et al. 2016). MEGAN accounts for soil moisture through a parameterisation that drops plant emissions to zero below a prescribed soil moisture level (the wilting point).~~^{tb} For example,^{tb} Jiang et al. (2018) found that improving ~~MEGAN~~^{the}^{tb} parameterisation of drought based on a measurement campaign in the U.S. would lower isoprene emissions globally by ~ 17%.

Chamber studies are often used to inform modelled isoprene reactions (e.g., Paulot et al. 2009b). However these results come with their own uncertainties, not the least of which comes from the difficulty of reproducing ambient air in laboratory conditions (Nguyen et al. 2014). Structural uncertainties (differences between different measurement techniques) in measurements also occur, which increases the difficulty of assessing isoprene datasets.

1.5.4.2 Resolution

Atmospheric chemistry simulations are somewhat sensitive to the gridbox resolution. Reducing model resolution can increase OH concentrations and ozone production rates (Wild and Prather 2006). Increasing model resolution can also impact OH, HO₂, and ozone concentrations (e.g., Christian, Brune, and Mao 2017). Yu et al. (2016) show that only at higher resolution (0.25 by 0.3125°) does isoprene oxidise under the correct NO_x pathway (through high or low NO_x pathways, see Section 1.3.4) in variable NO_x environments. This leads to an increase of high NO_x pathway oxidation of isoprene at the lower resolutions, which leads to an overestimation of HCHO but not ozone at coarser resolutions. However, for many global scale analyses, errors from resolution are less important than those from chemistry, meteorology, and emissions (Christian, Brune, and Mao 2017; Christian et al. 2018).

1.5.4.3 Chemistry mechanisms

Chemical mechanisms in several contemporary models are likely inadequate (Marvin et al. 2017), especially for isoprene oxidation, with changes to reaction rates being inadequate to fix discrepancies from measurements. Ozone uncertainties are also affected by inadequate mechanisms, for example, ozone concentrations simulated by GEOS-Chem are most sensitive to NO₂ photolysis, the NO₂ + OH reaction rate, and precursor emissions (Christian, Brune, and Mao 2017).

1.5.4.4 Clouds

One of the major uncertainties in chemical models is cloud formation and dynamics. Clouds are remarkably complex at a much finer scale than can be accurately modelled by global chemistry models (with current processing power). Globally over half (50-60%) of the world is covered by clouds, with $\sim 10\%$ of them being rain-clouds (Kanakidou et al. 2005). Wet scavenging in clouds not only depends on large scale cloud processes, but also on the microphysics of aerosols being scavenged, and these processes must be parameterised in coarse resolution models.

1.6 Australia and the southern hemisphere

Australia is unique, with its own climate, soil moisture, clay content, plant species, ecosystem life-cycles, agricultural and mining practices, transport corridors, and many other important properties that affect emissions, atmospheric chemistry, and ultimately atmospheric composition. Many regions in Australia are difficult or expensive to reach, and measurement campaigns are limited. In Australia, most long term air quality or composition measurements are performed in or near large cities. Australia is dominated by areas with little anthropogenic influence, and few ground based measurements of natural emissions take place (VanDerA et al. 2008). Since many Australian cities are on the edge of regions with rich VOC emissions, it is very important to clarify the quantity, type, and cause of VOC emissions. Understanding of emissions from these areas is necessary to inform national policy on air pollution levels.

Ozone enhancements above the background levels are most sensitive to emissions (of precursor gases), with meteorology, and atmospheric composition also important. Anthropogenic emissions of ozone precursors are important but relatively stable, while pyrogenic sources are greatly variable and dependent on weather, fuel, and fire intensity (e.g., Lawson et al. 2017). Biomass burning in southern Africa and South America has previously been shown to have a major influence on atmospheric composition in Australia (Oltmans et al. 2001; Gloudemans et al. 2006; Edwards et al. 2006), particularly from July to December (Pak et al. 2003; Liu et al. 2016a). Local fires are even more influential and the burning season for Australia can be all year, although distinct burning seasons for different regions are also apparent (Russell-Smith et al. 2007). Bushfire severity depends on regional vegetation, recent and current weather, and El Niño phase.

1.6.1 Ozone

Surface ozone levels over Australia are relatively low (~ 20 ppb) (Young et al. 2017). It remains unclear how ozone will change in the future as relatively little is known about precursors and influx for the continent. Australian air quality is monitored independently within each state. Measurement stations are generally located in population centres, which means there is a lack of natural emissions. Natural emissions can be important in urban regions as they can characterise the inflow, and affect air quality through production of O_3 and other pollutants. Overall in the southern hemisphere there are relatively few records of ozone (Huang et al. 2018). This affects scientists

our^{mh} ability to accurately determine sources of ozone in the troposphere, with current southern hemisphere trends lacking full explanation (Zeng et al. 2017).

Generally STT of ozone over Australia only affects the upper troposphere; however, ozone enhancements can reach low altitudes during heavy storms and cyclonic weather patterns (Alexander et al. 2013). The contribution of STT to overall tropospheric ozone budgets remains uncertain, especially in the southern hemisphere (Škerlak, Sprenger, and Wernli 2014). STT can enhance surface ozone concentrations above legal air quality limits (e.g., Lelieveld et al. 2009; Lin et al. 2015). Detecting ozone enhancements over the background profile in the relatively clean southern ocean atmosphere is simple. However, measurements of ozone over this region are sparse (Škerlak, Sprenger, and Wernli 2014), and quantification of transported ozone is difficult without large scale extrapolations. Ozone enhancements over the southern ocean signify either transported pollution or stratospheric influx (Jacobson and Hansson 2000). Quantifying ozone processes over the southern ocean could improve **our^{mh}** understanding of chemistry in the “clean background environment”, while additionally helping to validate model and satellite datasets. This poorly understood background composition forms the inflow of air into urban areas, and an improved understanding is required in order to model and attribute pollution and composition in these areas also.

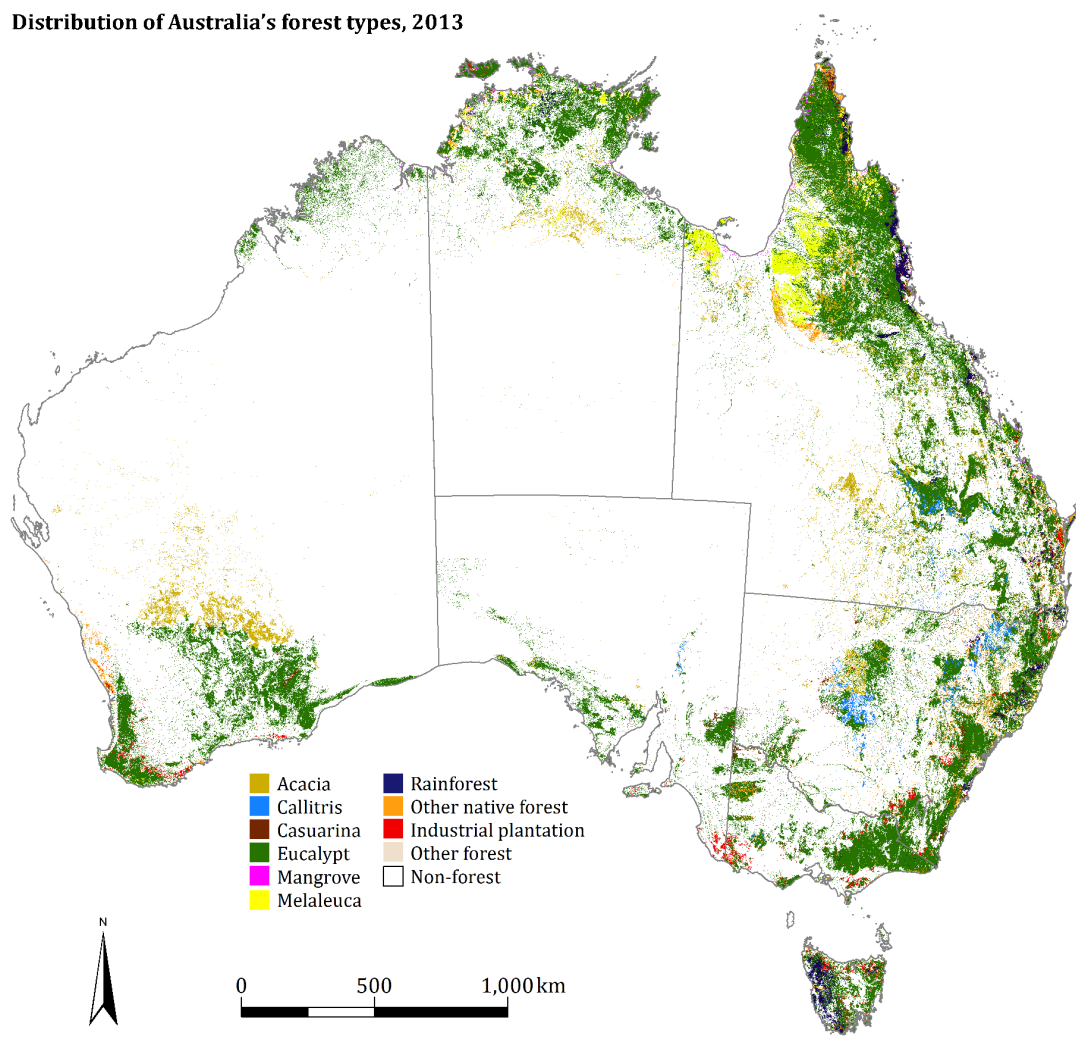
1.6.2 Biogenic VOCs

The vegetation in Australia is diverse. Figure 1.10 shows the different forest types and their locations within Australia, highlighting that much of **the-our^{mh}** forested lands are frequently found near population centres along the east coast. 16% of Australia is covered by forest, most (75%) of which is Eucalyptus, a major emitter of VOCs (Guenther et al. 2012).

It has been estimated by MEGAN that Australian vegetation is among the world’s strongest isoprene emitters, with forests in SE Australia having emission factors greater than $16 \text{ mg m}^{-2} \text{ h}^{-1}$ (see figure 1.11) (Guenther et al. 2006; Guenther et al. 2012). Measurement campaigns in SE Australia have since cast doubt on the emission factors used by MEGAN, potentially due to poor characterisation of Eucalyptus trees and soil moisture (Emmerson et al. 2016; Emmerson et al. 2019). These emissions factor estimates are not well verified and measurements of isoprene (or other BVOC) emissions are sparse and infrequent in Australia (Sindelarova et al. 2014; Bauwens et al. 2016).

Australia has a much greater diversity of tree species than is represented by MEGAN, however sparse measurements of emissions and BVOC concentrations makes model improvement difficult. Uncertainties in isoprene emissions could explain why models of HCHO over Australia are poor at reproducing satellite measurements (Stavrakou et al. 2009).

Australia suffers from poor characterisation of plant emissions, partly because many of the emission factors are based on northern hemispheric data. Many plant emissions rates have not been published, such as those for any Australian acacias. Some Eucalypt emissions are based on samples from young trees, which may emit more isoprene than older trees (Emmerson et al. 2016). Changes in parameterisation



Source: ABARES (2016) Map compiled by ABARES 2016

© Commonwealth of Australia 2016. This material is licensed under a Creative Commons Attribution 3.0 Australia Licence.

FIGURE 1.10: Forest types in Australia reproduced from <http://www.agriculture.gov.au/abares/forestsaustralia/australias-forests>.

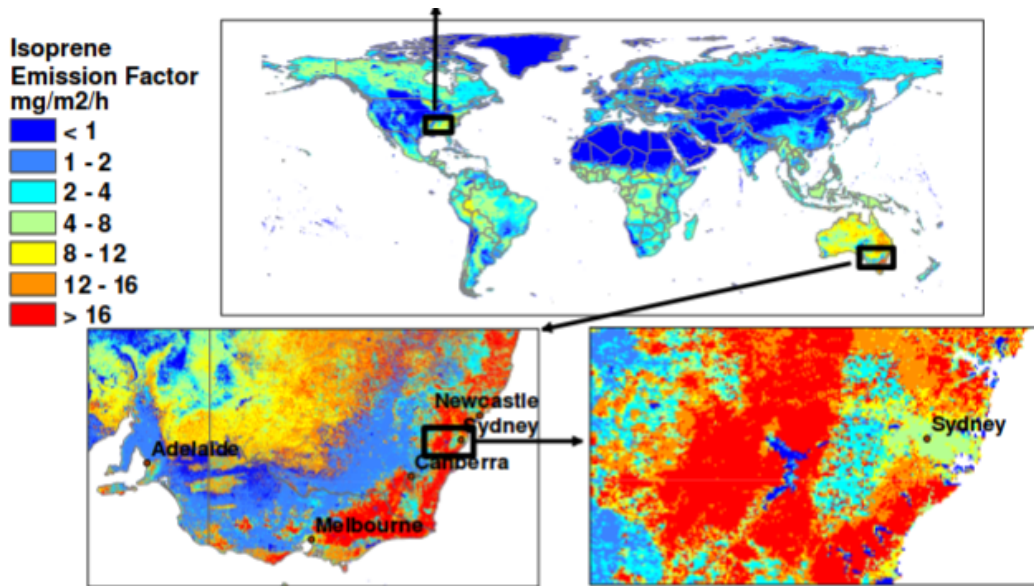


FIGURE 1.11: Global and Australian isoprene emission factors modified from Guenther et al. (2006).

of soil moisture in the MEGAN model lead to large reductions (38 – 58%) in Australian isoprene emission estimates, although errors remain (Sindelarova et al. 2014; Emmerson et al. 2019).

The only VOC emission information currently available come from three campaigns: the Measurements of Urban, Marine and Biogenic Air (MUMBA), and the two Sydney Particulate Studies (SPS1 and SPS2) (see Section 2.2). These measurements take place in south eastern Australia, and have suggested lower isoprene emissions than seen in models (by a factor of 2-6) (Emmerson et al. 2016). Several improvements are required as no simple scaling factor can completely fix the misrepresentation of isoprene emissions (Emmerson et al. 2016). These measurements focus on air quality and biogenic VOCs and use several different instruments (including PTR-MS and GC-FID) to detect metrics such as air particulates, HCHO, isoprene, and meteorological information. There is also an instrument at University of Wollongong (see Section 2.2.3.3) that provides 20 years of HCHO measurements, which is the only available long term HCHO vertical column measurement record in Australia comparable to satellite data. Satellite HCHO column measurements can be limited by various factors including interfering species, water, clouds, orography, etc, and independent in situ measurements are required to validate the data. For further details on these campaigns and measurements, see Section 2.2.

Improvements to emissions models require improved understanding of emissions from Australian vegetation and how they respond to meteorological and chemical parameters. However, constraining these processes is difficult given the lack of available isoprene measurements. Satellite measurements of HCHO can instead be used to estimate and improve Australian isoprene emissions without costly measurement campaigns. This is due to the near-linear relationship between HCHO and isoprene emissions (e.g., Palmer et al. 2001; Millet et al. 2006; Bauwens et al. 2016). This method

is explored in this thesis as described in Chapter 3.

1.7 Aims

This thesis aims In this thesis I aim^{mh}to improve understanding of natural contributions to ozone over Australia and the southern ocean. The two largest contributors to tropospheric ozone concentrations are chemical production (driven by precursor emissions) and transport from the stratosphere. **This thesis aims I aim^{mh}to improve understanding of both of these sources using existing satellite and ground-based datasets along with modelled outputs from the GEOS-Chem chemical transport model.**

Estimation of BVOC emissions in Australia can be improved through satellite measurements of HCHO, one of isoprene's primary oxidation products. Satellites that overpass daily record measurements over all of Australia. Combining satellite data with model outputs provides a platform for the understanding of natural processes, which are uncertain over Australia. Satellite measurements require modelled a priori vertical profiles of HCHO to estimate total column amounts. **This thesis aims I aim^{mh}to recalculate satellite vertical columns of HCHO using updated model a priori information.** In this effort **I aim to improve the understanding of**^{mh} the importance of relevant parameters (within GEOS-Chem) in calculating vertical columns of HCHO measured by satellite **is analysed^{mh}**. This includes an examination of how well GEOS-Chem simulates several species such as NO_x, isoprene, and HCHO compared to both in situ and remote measurement data that exists for Australia. Additionally, **I detail^{mh}the construction and effects of satellite data filters is examined^{mh}**. The work towards this aim is detailed in Chapter 2.

The technique of determining isoprene emissions from satellite detected HCHO is called satellite inversion. **This thesis aims I aim^{mh}to determine isoprene emissions in Australia using a top-down inversion of satellite HCHO, through a modelled yield from isoprene to HCHO.** HCHO amounts and the yield of isoprene to HCHO over Australia is required to create top-down estimates. This process also requires careful examination of when the assumptions required within the inversion process are not valid. Due to the low availability of in situ data over most of the Australian continent, a combination of modelled and satellite data can reduce the uncertainties of isoprene emissions from Australian landscapes. Improved emissions estimates will in turn improve the accuracy of CTMs, providing better predictions of atmospheric composition and its response to ongoing environmental change. The work towards fulfilling this aim is in Chapter 3.

Stratospheric transport is the second largest driver of tropospheric ozone concentrations, and an improved understanding of transported ozone can be determined from ozonesonde measurements. **This thesis aims I aim^{mh}to improve understanding of ozone transported to the troposphere from the stratosphere in Australia and the southern ocean.** Ozonesondes provide a glimpse of the vertical ozone profile up to ~ 30 km. **In this thesis , and I use^{mh}a Fourier filter is used^{mh} to determine how often stratospheric transport is occurring at three sites: Melbourne, Macquarie Island, and Davis Station. Transport event frequency analysis combined with modelled ozone**

distributions is used to derive a new method of detection and quantification of transported ozone as described in Chapter 4.

Overall, **this thesis aims I-aim^{mh} to describe relative importance of sources of tropospheric ozone in Australia, as well as their seasonality. This includes a description of I-will-describe^{mh} how modelled ozone is affected by updated isoprene emissions, a comparison of comparing^{mh} changes in GEOS-Chem outputs, and an analysis of by^{mh} ozone transport from the stratosphere..^{mh}** This thesis will provide new insight into tropospheric ozone in Australia.

Chapter 3

Biogenic Isoprene Emissions in Australia

3.1 Introduction

Biogenic volatile organic compounds (BVOC) affect the oxidative capacity of the atmosphere and their emissions are largely driven by what type of vegetation is in the area (Kefauver, Filella, and Peñuelas 2014). In the troposphere, BVOC emissions affect hydroxyl radical (OH) cycling, ozone (O_3) production, secondary organic aerosol (SOA) production, and methane lifetime. Australian forests are strong emitters of isoprene, the primary BVOC emitted globally (Guenther et al. 2006; Messina et al. 2016). Isoprene is relatively difficult to measure due to its high reactivity and short lifetime. Poor measurement coverage of isoprene, isoprene products, and isoprene emissions within Australia means that emissions are poorly understood. The lack of knowledge about emissions makes it difficult to estimate the subsequent atmospheric processes.

Emission models used to derive estimates of isoprene fluxes are based on understanding the emissions from different plant species (phenotypes) in varying conditions. Guenther et al. (2012) estimated global biogenic isoprene emissions at roughly 535 Tg yr^{-1} , while Sindelarova et al. (2014) estimated around 411 Tg yr^{-1} . Reactions following emissions are complex, and are sensitive to other trace gases in the atmosphere. Uncertainties in several important products such as ozone and SOA are increased due to both isoprene measurement difficulties and its complicated subsequent chemical mechanisms. Isoprene emissions in the frequently used MEGAN model may be overestimated in Australia since they are based on measurements taken from a few young trees (Winters et al. 2009) that may emit more than older trees (Emmerson et al. 2016). The sample of trees used to construct the MEGAN emissions model included 4 types of Eucalyptus, which are not representative of the hundreds of species that make up Australian forests. Additionally, how these species react to biological and meteorological stresses is unclear (Winters et al. 2009; Fortems-Cheiney et al. 2012). Emissions estimates are necessary inputs for atmospheric chemistry models and improving these estimates for Australia is a primary goal of this thesis.

This chapter describes and implements *In this chapter, I describe and implement^{mh}* a *top-down* technique using satellite measurements of HCHO to calculate surface isoprene emissions. HCHO is a primary product of most BVOC (including isoprene) oxidation, and is measured by satellites via remote sensing. In situ isoprene concentration measurements are costly and sparse within Australia, while satellite HCHO data are

plentiful and freely available, making this technique very attractive. Top-down techniques have informed isoprene emission inventories in North America (Abbot 2003; Palmer et al. 2003; Palmer et al. 2006; Millet et al. 2006; Millet et al. 2008), South America (Barkley et al. 2013), Europe (Dufour et al. 2008; Curci et al. 2010), Africa (Marais et al. 2012), Asia (Fu et al. 2007; Stavrakou et al. 2014), India (Surl, Palmer, and Abad 2018), and even globally (Shim et al. 2005; Fortems-Cheiney et al. 2012; Bauwens et al. 2016). In this thesis ~~the technique is applied~~^{I apply the technique^{mh} focusing solely on Australia for the first time.}

3.1.1 Aims

Recent work suggests that modelled emissions may be overestimated in southeast Australia (Emmerson et al. 2016). This chapter aims to improve the understanding of isoprene emissions over the whole of Australia, clarifying the spatial distribution of bias and how these biases impact modelled chemistry. ~~Isoprene emissions are estimated~~^{I estimate isoprene emissions^{mh} in Australia using a top-down technique based on OMI HCHO measurements and GEOS-Chem modelled yields. This a posteriori top-down estimate is evaluated against bottom-up a priori estimates and also briefly compared against available ground-based measurements. The GEOS-Chem model is modified to run with the a posteriori isoprene emissions to determine potential impact on modelled chemistry. Goodness of fit between in situ, satellite, and modelled HCHO is determined before and after scaling emissions estimates.}

First ~~an outline is provided showing~~^{I outline^{mh} why current isoprene emissions estimates are inadequate and how they can be improved. ~~This thesis discusses~~^{I discuss^{mh} literature that shows how the estimates may be too high, and describes^{mh} how emissions may be calculated using satellite datasets. Section 3.2 lays out how new isoprene emissions are estimated, with results examined in Section 3.3. Section 3.3 includes a comparison of updated satellite HCHO columns (Chapter 2) to available measurements, and an examination of how these changes in emissions would affect ozone concentrations in Australia. Uncertainties for each step along the way are quantified in Section 3.4.}}

3.1.2 Existing emissions estimates

MEGAN is one of the most widely used sources for estimating biogenic isoprene emissions. However, along with other models that rely on measured plant emission rates, it is poorly calibrated for Australian conditions. Emissions of isoprene (C_5H_8) appear to be overestimated within Australia (Sindelarova et al. 2014; Stavrakou et al. 2014; Emmerson et al. 2016), although the lack of measurements of isoprene emission rates in Australia makes this overestimation difficult to characterise. Bauwens et al. (2016) showed that isoprene emissions were overestimated by up to a factor of 3 over Australia. Emmerson et al. (2016) suggest isoprene emission estimates are 2-6 times too high compared against available measurements of isoprene concentrations. They compared modelled data to campaign measurements from multiple sites over different seasons and found that scaling emissions did not universally improve model outputs.

Recently Bauwens et al. (2016) estimated isoprene emissions with a top-down technique using the IMAGESv2 global CTM. They calculated emissions that create the closest match between model and OMI satellite vertical columns, and compared these a posteriori data with their a priori (model) data and independent datasets. For Australia they found MEGAN based estimates ranging from 38 Tg C yr⁻¹- 94 Tg C yr⁻¹, and a posteriori emissions of 36 Tg C yr⁻¹. In this thesis ~~I develop and analyse~~^{mh} a top-down emission estimate ~~is developed, analysed and, which is~~^{mh} then compared against MEGAN. ~~Hi also look at h~~^{mh}ow changed emissions affect modelled ozone levels over Australia ~~is also looked into~~^{mh}.

3.1.3 Top-down isoprene emissions estimates

In the remote troposphere HCHO production is dominated by methane oxidation, while in the continental boundary layer production is largely due to non-methane VOCs (NMVOCs) (Abbot 2003; Kefauver, Filella, and Peñuelas 2014). This leads to a causal relationship between enhanced HCHO concentrations and NMVOC emissions at low (< 1 km) altitudes. NMVOCs are generally short lived (< 1 hr), and the most prominent of these is isoprene. Isoprene is emitted and enters the atmosphere in the gas phase, where it begins a complex series of reactions. HCHO is produced with high yield in many reactions beginning with isoprene oxidation (discussed in more detail in Section 1.3.4) and it has a lifetime of a few hours (Kefauver, Filella, and Peñuelas 2014).

Top-down estimates determine emissions of a particular species through careful analysis of the measurable products of that species. This generally takes advantage of longer-lived products that may reach an equilibrium in the atmosphere. Continental tropospheric HCHO enhancements can be directly linked to biogenic isoprene emissions. Since 1997, when the Global Ozone Monitoring Experiment (GOME) satellite measurements were first used to measure HCHO, satellites have been used to provide a total column measurement of HCHO, enabling isoprene emissions estimation by top-down methods (Thomas et al. 1998; Palmer et al. 2001; Bauwens et al. 2016). Using satellite information to improve estimates of biogenic emissions has been highlighted as a valuable use of satellite derived datasets (Streets et al. 2013). Here NASA's OMHCHO product based on measurements from the OMI instrument onboard the Aura satellite (see Section 2.4) is the basis for a top-down biogenic isoprene emission estimate over Australia.

There are two top-down isoprene emission estimation techniques, Bayesian and linear, which are discussed briefly here. Both the linear and Bayesian techniques assume that modelled chemistry is accurate and only try to correct precursor emissions. This is an additional source of uncertainty given existing uncertainties in chemical mechanisms.

3.1.3.1 Bayesian inversion

Bayesian inversion optimises model parameters in order to minimise the difference between model output and an (ideally) independent dataset such as satellite measurements. Emissions of isoprene (and other precursors to HCHO) will form part of the set of model parameters that are adjusted to make the model HCHO output most closely

match satellite measurements. These inversions can be set up to account for effects from transport and allow source attribution (e.g., Curci et al. 2010; Fortems-Cheiney et al. 2012).

In general, a model (the forward model) is used to determine the relationship between HCHO (y) and the state variable x , which represents isoprene emissions (and other variable parameters of interest):

$$y = \mathbf{K}\mathbf{x} + b + \epsilon \quad (3.1)$$

where ϵ are the (assumed) independent errors in measurements. K is the Jacobian matrix determined from the forward model representing the sensitivity of y to the state variable x . Essentially the K matrix is the modelled estimation of how y responds to each of the driving parameters represented by elements of x . This K matrix is used in conjunction with error covariance in x to determine the most likely solution to x , given what is known about y .

This method was used by Shim et al. (2005) to optimise isoprene emissions in areas with high HCHO concentrations. They showed model underestimation of isoprene emissions by 14-46%, which was reduced to 3-25% after applying satellite based improvements. More recently Kaiser et al. (2018) showed a 40% bias in MEGAN isoprene emissions over the southeast US using a Bayesian inversion based on OMI HCHO.

An advantage (over the linear method described below) of the Bayesian method is that it can account for pyrogenic and anthropogenic emissions, as these form part of the state variable x as well as transport. However, biases in the underlying model will still propagate through to the a posteriori emission estimation (Curci et al. 2010). More limiting is the fact that the Bayesian method is computationally expensive. In this work [the Bayesian method is not used](#)^{I do not use the Bayesian method}^{mh} due to the computational costs surpassing the resources available.

3.1.3.2 Linear inversion

The linear technique is performed in this thesis. Vertical columns of HCHO from satellite and modelled yield from isoprene allow the inference of local (grid space) isoprene emissions (Palmer et al. 2003; Millet et al. 2006; Marais et al. 2012; Surl, Palmer, and Abad 2018). The primary assumption of the linear inversion technique is that HCHO and its precursors (primarily isoprene) are in a linear steady state relationship. This allows one to link isoprene emissions to HCHO measurements using production and loss rates. Essentially a linear relationship between total column HCHO (Ω) enhancement above a background level (Ω_0) and isoprene emissions (E_{isop}) is determined:

$$\Omega = S \times E_{isop} + \Omega_0$$

This uses modelled vertical columns and emissions to estimate the slope (S). Then this modelled S is applied to satellite measurements of Ω (Ω_{sat} and $\Omega_{sat,0}$) to determine \hat{E}_{isop} :

$$\hat{E}_{isop} = \frac{\Omega_{sat} - \Omega_{sat,0}}{S}$$

This is described further in Section 3.2, with an outline in Section 3.2.1.

The calculation requires reaction rates and yields from isoprene to HCHO, which can be determined most readily using chemical modelling. The method for calculating isoprene emissions from HCHO is laid out in Palmer et al. (2003), taking into account the expected lifetime and reaction rates of the precursor VOCs and HCHO. In their work, isoprene emissions fluxes over the US were derived using the GOME satellite instrument. The method has since been applied to many regions using GOME, SCIAMACHY, OMI, and GOME-2 satellite data (e.g., Abbot 2003; Barkley et al. 2013; Stavrakou et al. 2014; Surl, Palmer, and Abad 2018).

The linear inversion assumes fast HCHO yield from isoprene and no precursor transport, which is unrealistic in certain scenarios. For example, high wind speeds can transport precursors, or low NO_x concentrations can slow HCHO production (Palmer et al. 2006; Surl, Palmer, and Abad 2018). Filtering out data that do not match assumptions is required but can limit the utility of this technique, and leads to some dependence on environmental factors. Uncertainties in the technique are discussed in more detail in Section 3.4.1. Nonetheless, a major benefit is that the simple nature of the inversion requires very little computational power after acquiring satellite and model datasets, even over large amounts of gridded data. This allows an inversion using more than 8 years of satellite and model data, capturing inter-annual variability over all of Australia. With the computational resources available this would not have been possible using the Bayesian inversion.

3.2 Methods

The method of Palmer et al. (2001) is broadly followed^{mh} to create a biogenic isoprene emissions estimate over Australia. A relationship is modelled between biogenic-only midday tropospheric columns of HCHO and GEOS-Chem midday biogenic isoprene emission rates, and then this relationship is applied to satellite measured HCHO total columns to derive a new isoprene emissions estimate. Daily modelled values averaged between 13:00–14:00 LT are used to match the overpass time of the Aura satellite. Then the slope is calculated using reduced major axis regression between the a priori isoprene emissions (those from GEOS-Chem, E_{GC}) and tropospheric HCHO columns in each model grid box each month. There is very little HCHO above the tropopause, so differences between total and tropospheric column are negligible. In this work total and tropospheric column HCHO are used interchangeably and referred to using Ω .

3.2.1 Outline

This section provides an overview of the steps involved in creating a top-down emissions estimate. This process is summarised in Figure 3.1.

1. Corrected vertical columns (Ω_{OMI} ; saved in the OMHCHORP dataset) are calculated (see Section 2.6) using level two OMI HCHO satellite data (see Section 2.4), along with GEOS-Chem model runs (see Section 2.3.6). Satellite columns are binned into both $0.25^\circ \times 0.3125^\circ$ and $2^\circ \times 2.5^\circ$ horizontal resolutions. In this step model background values (columns over the remote Pacific) are used to correct the vertical columns, which is explained in Section 2.6.5.

2. Level three satellite data are used to make anthropogenic, fire, and smoke influence masks (see Section 2.7). These are applied to remove Ω_{OMI} that may be influenced by pyrogenic or anthropogenic sources.
3. A mask is created showing where the HCHO production is not dominated by local isoprene emissions. This is determined by calculating smearing over Australia using two model runs with differing isoprene emissions. The smearing value is determined as $\hat{S} = \Delta\Omega_{GC}/\Delta E_{OMI}$: the ratio of the differences between model runs of HCHO columns and isoprene emissions. A full description of the creation of this smearing filter is given in Section 2.7.3.
4. GEOS-Chem modelled biogenic emissions of isoprene (E_{GC}) along with biogenic columns of HCHO (Ω_{GC}), both averaged over $2^\circ \times 2.5^\circ$ horizontally and 13:00–14:00 LT temporally, are used to calculate a reduced major axis linear regression slope S ($\Omega_{GC} = S \times E_{GC} + \Omega_{GC,0}$). Calculation of this modelled slope is explained in Section 3.2.4.
5. Satellite HCHO Ω_{OMI} and S then form the basis for the top-down estimate of biogenic isoprene emissions (E_{OMI} atoms C $\text{cm}^{-2} \text{ s}^{-1}$). This is the product is our^{mh} a posteriori, and calculation details are given in Section 3.2.7.
6. A posteriori top-down emissions E_{OMI} are compared against a priori emissions, and analysed in conjunction with independent observations from in situ measurements (MUMBA and SPS). Results are examined in Section 3.3.
7. GEOS-Chem is run using the a posteriori emissions (see Section 3.2.8), and HCHO, O₃, isoprene, and NO_x outputs are compared to a priori values and to campaign and satellite measurements where possible (Sections 3.3.3).

3.2.2 Masks and reprocessed satellite HCHO

Satellite data pixels are read from OMHCHO, the level 2 OMI HCHO dataset, AMFs are recalculated, and then pixels are gridded daily into $0.25^\circ \times 0.3125^\circ$ horizontal bins. This forms the intermediate product OMHCHORP, which is fully described in Section 2.6.1. This dataset includes gridded satellite HCHO columns (Ω_{OMI}), along with pixel counts (how many satellite data points were used for each grid box) to allow averaging, re-binning, and uncertainty analysis. In this thesis the OMI product is usedI-use the OMI product^{mh} as the overpass time (13:30 local time) is closer to peak isoprene emissions than that of GOME or GOME-2.

In order to determine biogenic HCHO enhancements from Ω_{OMI} , filters for non-biogenic sources are required. These masks are described in Section 2.7, and a brief recap is provided here. Methane oxidation is a major part of the formation of background HCHO; however, the linear regression used to estimate isoprene emissions effectively removes this source (by assuming a constant background), which means a methane contribution filter is not required. Anthropogenic, pyrogenic, and smoke influence masks are created from three satellite products: NO₂ from OMNO2d, fire counts from MOD14A1, and AAOD from OMAERUVd, respectively.

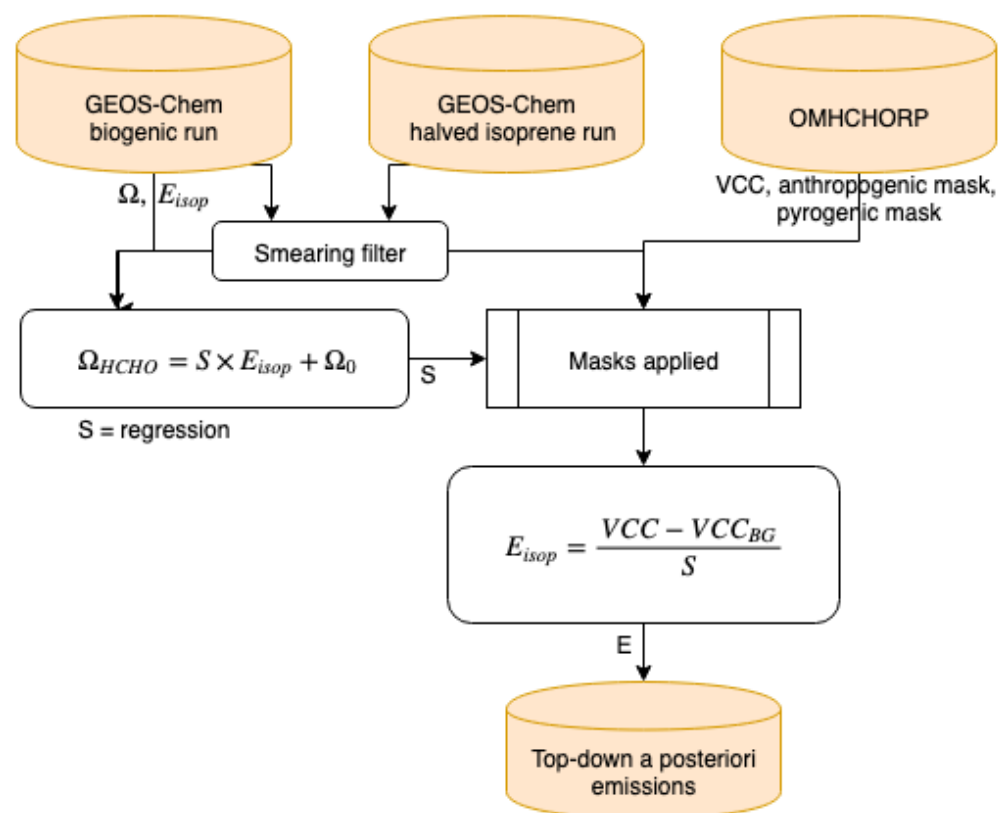


FIGURE 3.1: Top-down isoprene emissions estimate formation using OMHCHORP and GEOS-Chem outputs.

1. The fire mask is created daily using non-zero MODIS fire counts over the prior 2 days that occur in local or adjacent grid squares at $0.25^\circ \times 0.3125^\circ$ horizontal resolution.
2. Influence from transported smoke plumes is removed by flagging grid squares where OMI aerosol absorption optical depth (AAOD, from OMAERUVd) is greater than 0.03.
3. A filter for anthropogenic influence is created daily using OMNO2d NO₂ tropospheric column amounts, masking any grid squares with greater than 2.0×10^{15} molec cm⁻² on any particular day, along with grid squares where the yearly average is above 1.5×10^{15} molec cm⁻².

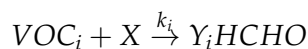
The recalculated corrected vertical columns are saved to OMHCHORP dataset both before and after applying the filters to allow filter analysis.

3.2.3 GEOS-Chem emissions

In this work MEGAN (version 2.1) is run as a module within GEOS-Chem (version 10.01). The chemical model is driven by GEOS-5 meteorological fields at $0.5^\circ \times 0.666^\circ$ horizontal resolution. GEOS-Chem output is averaged onto 47 vertical levels at $2^\circ \times 2.5^\circ$, based on chemistry and transport calculated every 30 and 15 minutes respectively. Isoprene emissions from the default *tropchem* simulation are referred to as the a priori emissions. When shown as part of a formula the a priori emissions are denoted as E_{GC} .

3.2.4 Relationship between isoprene emissions and formaldehyde

Tropospheric HCHO production is primarily due to the oxidation of VOC precursor species (VOC_i). Background concentrations are driven by methane; a longer lived (~ 8 yr) VOC. Over continental land masses, the variability in HCHO is driven by shorter lived precursor emissions (Chance et al. 2000; Palmer et al. 2003). HCHO is then produced quickly from short-lived intermediates:



where X is an oxidant, Y_i is HCHO yield (per C atom in VOC_i), and k_i is the reaction rate constant. In specific conditions described below, HCHO total columns (Ω ; molec cm⁻²) can be linearly related to isoprene emissions. In Australia the effective molar HCHO yield from isoprene has not been extensively studied, while in other continents this value varies from 1-3 depending on local NO_x concentrations (e.g., Palmer et al. 2006; Millet et al. 2006; Bauwens et al. 2016; Surl, Palmer, and Abad 2018).

The isoprene to HCHO relationship is derived using several assumptions that are outlined here. The first assumption is that HCHO is at steady state, which implies production (P_{HCHO}) and loss (L_{HCHO}) are equivalent:

$$\frac{d\Omega}{dt} = 0 = P_{HCHO} - L_{HCHO} \quad (3.2)$$

This is reasonable during midday when isoprene emissions are steady and Ω has had time to stabilise. The second assumption is that loss (with loss rate constant k_{HCHO}) is only first order, such as from photolysis and oxidation:

$$L_{HCHO} = k_{HCHO}\Omega \quad (3.3)$$

This assumption means that loss due to transport must be negligible as it is not first order. This assumption is reasonable for large enough grid boxes as transport becomes negligible relative to the linear (first order) terms. Production and loss are on the order of minutes, and grid box sizes in this work are rectangular with ~ 200 km edge lengths. Monthly averaged wind speeds rarely exceed 20 km hr^{-1} over Australia, meaning HCHO and precursor transport remain minor. Transport can still be an issue, however, and is handled by applying a smearing filter described in Section 2.7.3.

Another assumption is that Ω production above the background level is due only to precursor emissions (E_i ; atoms $C\ cm^{-2}s^{-1}$) multiplied by their yields to HCHO (Y_i):

$$P_{HCHO} = \sum_i Y_i E_i \quad (3.4)$$

By combining Equations 3.2, 3.3, and 3.4, Ω can be related to ~~we can relate Ω to~~^{mh} precursor emissions:

$$\begin{aligned} k_{HCHO}\Omega &= \sum_i Y_i E_i \\ \Omega &= \frac{1}{k_{HCHO}} \sum_i Y_i E_i \end{aligned} \quad (3.5)$$

Finally, it is assumed isoprene emissions are driving changes in Ω (as assumed elsewhere, e.g., Palmer et al. 2003; Millet et al. 2008; Marais et al. 2014; Stavrakou et al. 2015) and lump other terms together:

$$\sum_i Y_i E_i = Y_{isop} E_{isop} + \sum_{i \neq isop} Y_i VOC_i \quad (3.6)$$

This assumption is reasonable only over continental land masses, and can be false when pyrogenic or anthropogenic emissions influence the HCHO column. These scenarios are filtered to remove pyrogenic and anthropogenic influence using independent satellite measurements (see Section 2.7). The linear relationship between isoprene emissions and Ω is determined by equating P_{HCHO} and L_{HCHO} from Equations 3.4 and 3.3, substituting Equation 3.6, and assuming that the lumped terms make up the background:

$$\begin{aligned} k_{HCHO}\Omega &= Y_{isop} E_{isop} + \sum_{i \neq isop} Y_i VOC_i \\ \Omega &= \frac{Y_{isop}}{k_{HCHO}} E_{isop} + \Omega_0 \\ &= S \times E_{isop} + \Omega_0 \end{aligned} \quad (3.7)$$

Here S is the slope of the regression between E_{isop} and Ω : $S \equiv \frac{Y_{isop}}{k_{HCHO}}$.

3.2.5 Calculation of modelled slope

To determine S , the link between biogenic isoprene and midday column HCHO, GEOS-Chem is used. The term E_{GC} is used when discussing isoprene emissions estimated within GEOS-Chem and Ω_{GC} is used to represent simulated HCHO total column. The method to calculate S using GEOS-Chem follows roughly the following three stages:

1. Hourly gridded model outputs E_{GC} (atoms C cm $^{-2}$ s $^{-1}$), along with Ω_{GC} (molec cm $^{-2}$) at 13:30 LT daily are extracted from the biogenic-emissions-only run.
2. Filtering removes gridded output on days where grid squares are likely to be affected by smearing (see Section 3.2.5.1).
3. A reduced major axis regression slope is determined between Ω_{GC} and E_{GC} for every month of modelled output (one value per day) for each grid square (Figure 3.2).

Modelled background concentrations can be ignored here as they do not affect slope calculation. This effectively provides the monthly gridded slope (S) between biogenic isoprene emissions and HCHO columns, in units of seconds.

Figure 3.2 (top left) shows how S varies spatially over Australia for an example mid-summer month. High S values suggest high sensitivity of HCHO to isoprene emissions. Some areas can be seen to be very sensitive to emissions, such as the west coast and Eyre basin, which is likely due to the low isoprene and HCHO levels in those areas. The regression coefficients also vary spatially (top right), and some areas show little correlation. It is likely that this is due to weather, transport, and a lack of local emission sources. The slopes in the bottom panel show a small sample of scatter and regression plots. These can range widely due to differences in emission and yield parameters, which plays a role in the smearing filters described in Section 2.7.3. Due to the $2^\circ \times 2.5^\circ$ horizontal resolution of GEOS-Chem, calculations over coastal grid boxes that are mostly oceanic are often discarded as the change in HCHO is not dominated by emissions of isoprene, as is assumed for equation 3.7.

3.2.5.1 Smearing

One issue with slope calculation is potential transport (also known as smearing), either of isoprene transported in from outside the local grid box (before any HCHO is formed), or of HCHO formed by local emissions but transported out of the local grid box. A *smearing* filter is created (see Section 2.7.3) which filters out grid squares on days when transport is likely. Days where smearing is expected to affect local levels of HCHO are removed before calculating S , and a simple analysis is performed on how the filter affects monthly slope, correlation, and uncertainty. Figure 3.3 shows the calculated slope for 2005–2012, along with its 95% confidence interval for the $2^\circ \times 2.5^\circ$ grid box containing Sydney. The monthly and multi-year monthly averages are shown before and after the smearing filter is applied. The filter slightly reduces the amplitude of the seasonal cycle, raising the January minimum and lowering the June and July maximum. Filtering slightly improves the correlation coefficient throughout the year. This is likely due to smearing being prevalent in areas where the relationship between a priori emissions and HCHO columns is already weak (due to low emissions or

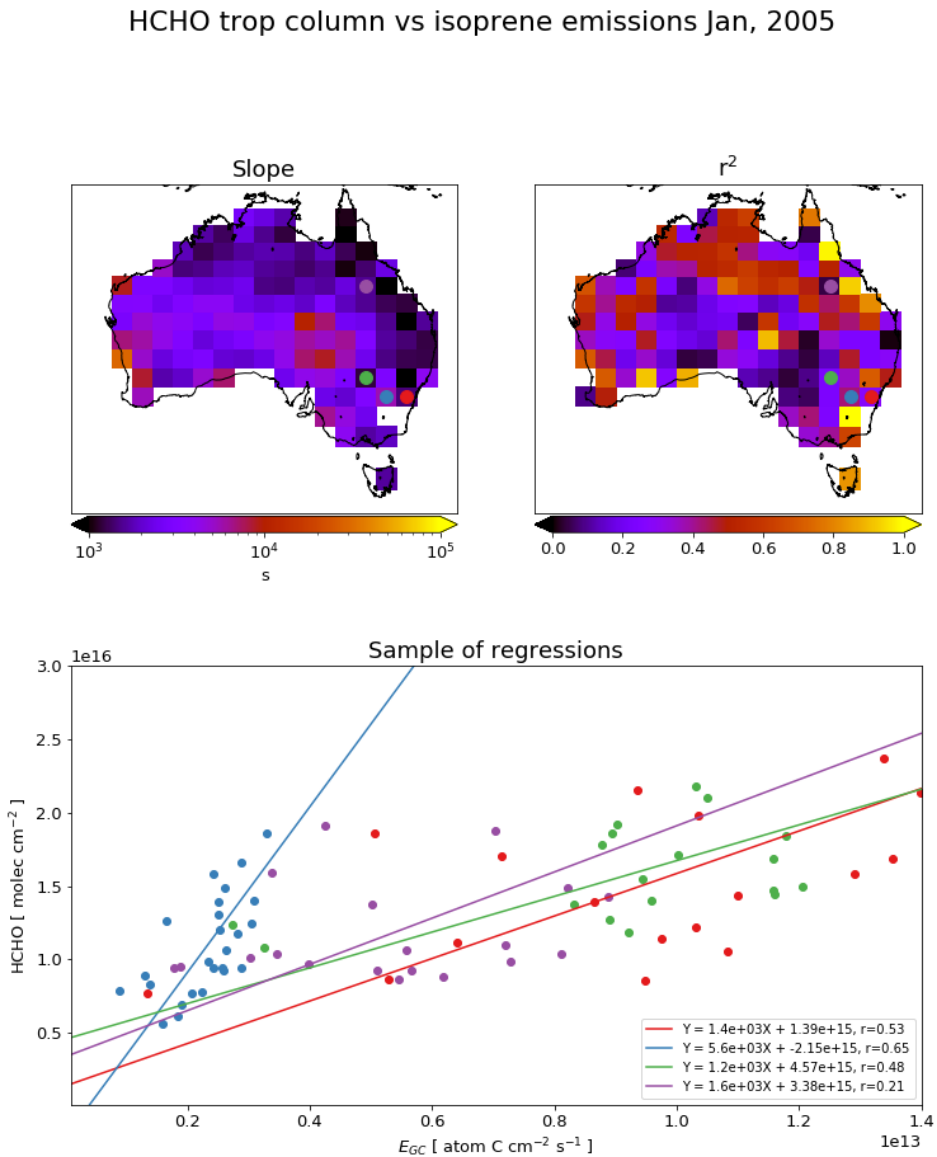


FIGURE 3.2: Top left: reduced major axis slope between modelled tropospheric column HCHO and isoprene emissions (E_{GC}) using mid-day (13:00-14:00 LT) values over for January 2005, per grid square at $2^\circ \times 2.5^\circ$ horizontal resolution. Top right: Squared reduced major axis correlation coefficient for regression in top left. Bottom: Sample of correlations from four grid squares. Coloured dots in top panels correspond to the colour of the regressions shown in bottom panel.

unsuitable meteorological conditions). More data are filtered in summer, presumably due to higher biogenic isoprene emissions over summer, making transport more noticeable on windy days. Anthropogenic precursor emissions are not halved between the two runs, and they make up relatively more of the total HCHO precursor concentration in winter (when biogenics are lower). This may lower the smearing filter signal over Sydney and other densely populated areas (especially in winter). This plot has been repeated for several grid squares over Australia (not shown) sometimes showing more filtering throughout winter months, and sometimes over summer months. When calculating top-down emissions the smearing-filtered slope (S) is generally used for each grid square month. The multiple year monthly averaged slope is used instead when the regression coefficient (r) is less than 0.4, or the number of data points used in the regression (n) is less than 10. When r for the multiple year slope is also lower than 0.4 (does not happen in the example grid square), no estimation is performed. This happens only infrequently, and only in locations with very limited isoprene emissions such as the lake Eyre basin.

Smearing can be dependent on local or regional weather patterns, as greater wind speeds will reduce the time any emitted compound stays within the local grid box. As such smearing can vary both spatially and temporally. Smearing is also sensitive to time of day, season, and latitude, as lower insolation results in slower photolysis. Figure 3.4 shows smearing and how frequently grid squares are filtered using the smearing filter. The smearing filter is more active in winter and spring, especially at higher latitudes. Grid squares along the east coast are filtered frequently in all seasons, as well as grid squares in the high smearing lake Eyre region in northeastern South Australia. Data loss from smearing is approximately 30% over the entirety of Australia during summer, and 40% during winter. The data loss is generally higher towards the north east and southern coastlines, and at lake Eyre.

3.2.6 Modelled background HCHO

There are two simple ways to determine the modelled background HCHO, one of which involves running the model with no isoprene emissions. Since variation in HCHO columns is assumed to only depend on isoprene emissions, theou^{mh} background term is theoretically identical to the simulated HCHO without isoprene emissions. The other method uses HCHO over the remote Pacific Ocean at matching latitudes and times, which emulates how the background is determined for the satellite measured HCHO. Figure 3.5 shows the background total column HCHO calculated in these two different manners, and how they compare to each other and normal levels for an example month (January, 2005). The difference between these definitions is approximately 15%, and is mostly caused by non-isoprene HCHO precursors (such as monoterpenes). Non-isoprene HCHO precursor emissions are neglected in the top-down estimation technique used in this work, which introduce some uncertainty (Section 3.4.2). Generally in summer months the continental HCHO levels are over 3 times higher than background levels, so the choice of background definition has only a very small impact on the final results. For consistency with the satellite data, backgrounds are determined using the remote Pacific. Background HCHO for any latitude in this thesis is calculated by averaging longitudinally (140°W to 160°W) the matching latitudes over the remote Pacific.

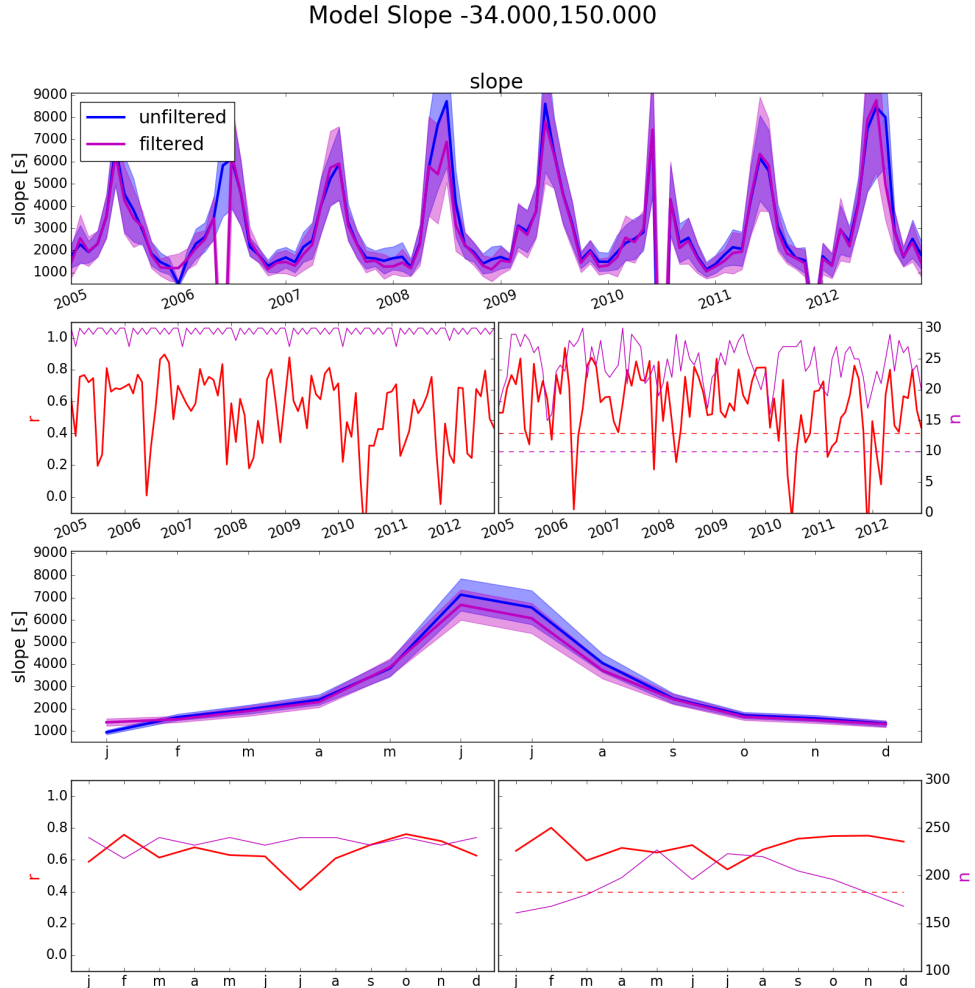


FIGURE 3.3: Row 1: monthly slope along with 95% confidence interval both before (blue) and after (magenta) applying the smearing filter for the model grid square containing Sydney over 2005-2012. Row 2: regression coefficient and data point counts before (left) and after (right) performing filtering for slopes shown in row 1. Additionally, limits for r and n used in slope utilisation (see text) are shown with dashed lines. Row 3: slope and confidence interval using the multi-year dataset for each month. Row 4: regression coefficient and data point counts for row 3.

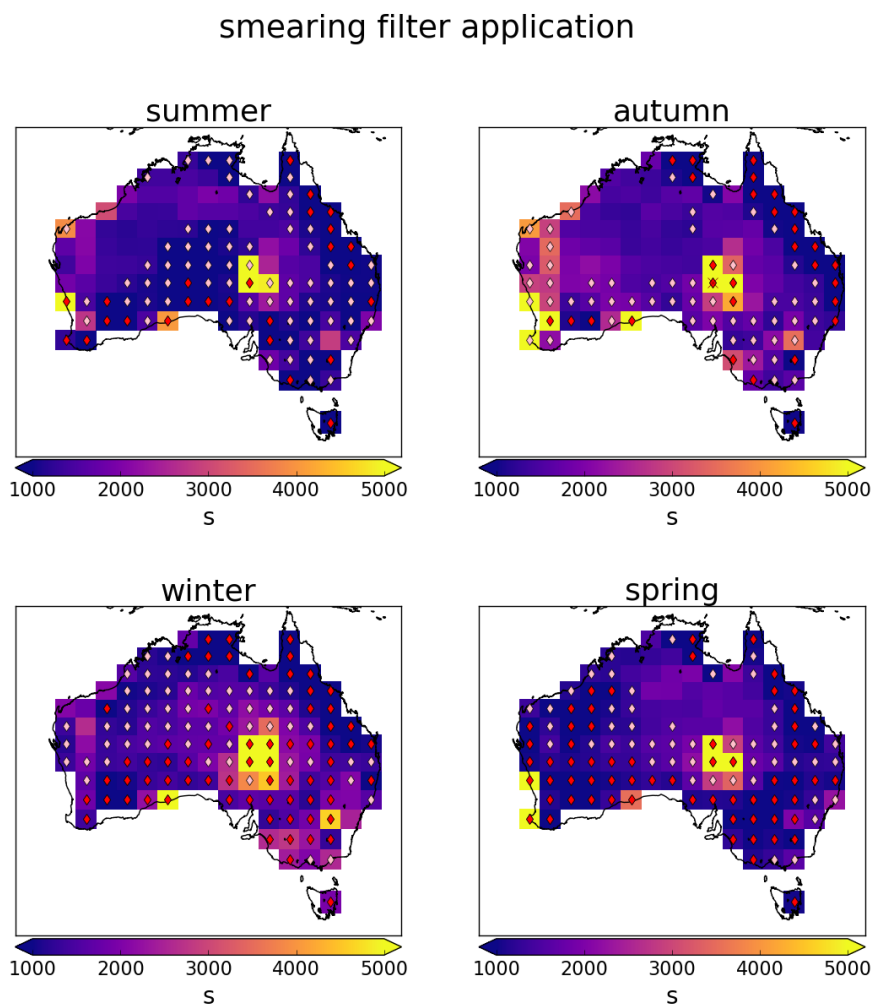


FIGURE 3.4: Seasonally averaged smearing (\hat{S} , see text) over 2005. Diamonds represent grid squares which have had at least 10 (pink) or 30 (red) days removed due to the smearing filter over the season. Red crosses show where the filter has removed all data.

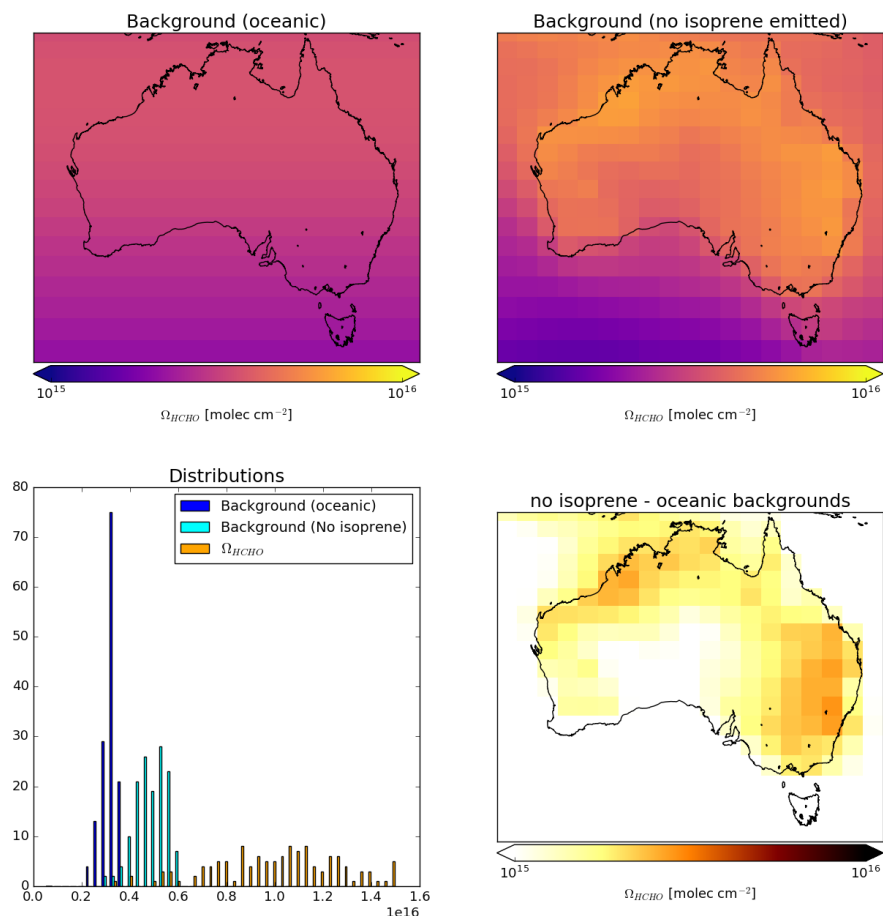


FIGURE 3.5: Top left: Background total column HCHO based on longitudinally averaged values over the remote Pacific Ocean. Top right: Background total column HCHO based on GEOS-Chem output with isoprene emissions set to zero. Bottom left: Distributions of column amounts over land squares in Australia from the two background definitions and the monthly HCHO average from GEOS-Chem (standard tropchem run). Bottom right: Absolute difference between the two background defined value maps.

3.2.7 Calculation of Emissions

Top-down emissions estimates are calculated using OMHCHO (see Section 2.4) slant columns and an updated AMF calculated using code written by Paul Palmer and Randal Martin, with modifications by Luke Surl (see Section 2.6.3.2). In Chapter 2 there are three calculations of the AMF referred to as AMF_{OMI} (the original OMI AMF), AMF_{GC} (AMF recalculated with GEOS-Chem shape factors), and AMF_{PP} (AMF recalculated using GEOS-Chem shape factors and scattering weights). The new emissions are calculated (using the AMF_{PP}) are referred to as the a posteriori from here onward, or E_{OMI} in formulae.

A posteriori emissions are calculated using the linear relationship described in Section 3.2.4 using the modelled slope S calculated in the prior section and satellite HCHO columns recalculated in 2.6:

$$\begin{aligned}\Omega_{OMI} &= S \times E_{OMI} + \Omega_0 \\ E_{OMI} &= \frac{\Omega_{OMI} - \Omega_0}{S}\end{aligned}\quad (3.8)$$

This is the same as equation 3.7, except now the satellite HCHO (Ω_{OMI} and Ω_0) is used. Ω_0 is calculated using Ω_{OMI} in the remote Pacific averaged monthly and longitudinally, for each latitude. This leaves E_{OMI} as the only unknown once the satellite measurements are processed to match the temporal and horizontal resolution of S .

One potential issue in this top-down estimation technique is the low number of valid satellite measurements that may occur due to the higher solar zenith angles in winter and at higher latitudes. Another issue is that negative emissions are commonly calculated in areas wherever measured HCHO columns are lower than background amounts (as $E_{OMI} = \frac{\Omega_{OMI} - \Omega_0}{S}$) due to uncertainty in the background calculation. These negative calculated emissions are set to zero, as negative emissions physically meaningless in this calculation. Relative uncertainty in these grid squares is set to 100% for later estimations of uncertainty (Section 3.4.1).

3.2.8 Running GEOS-Chem using a posteriori emissions

After creating the a posteriori isoprene emissions estimate (at monthly resolution), GEOS-Chem is re-run with biogenic emissions scaled to match the new estimate. This is performed by applying a seasonal scaling factor α , based on the multi-year monthly average difference between midday a priori and a posteriori emissions at $2^\circ \times 2.5^\circ$ horizontal resolution. α is the ratio between the multi-year averaged monthly emissions from GEOS-Chem E_{GC} and the a posteriori E_{OMI} :

$$\alpha = \frac{E_{OMI}}{E_{GC}}\quad (3.9)$$

This seasonal scaling retains shorter time-scale variability and meteorological dependencies built into the parameterisations of the MEGAN model, while ensuring the multi-year monthly averaged emissions match the a posterior totals. This method provides a preliminary estimate of the effects of scaling isoprene emissions towards the satellite based estimate, and running this analysis at a finer temporal resolution

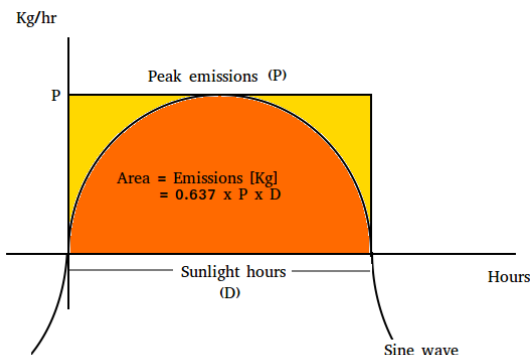


FIGURE 3.6: Total daily isoprene emissions (in kg) is represented by the area under the sine wave.

could be performed in future work. Initially α is uniformly set to 1 globally. Where top-down emissions exist and E_{GC} is non-zero, α is set using Equation 3.9. α is applied through the emissions module in GEOS-Chem where isoprene emissions are calculated. First, the new midday (13:00-14:00 LT) emissions (per grid box) are combined forming a multi-year monthly mean, which can be compared to the a priori equivalent. Missing values for α when E_{GC} are zero are a negligible issue since the dominant discrepancies between estimates occur during summer when high emission rates are overestimated.

To create the α scaling factor, modelled and top-down emissions are compared, which requires a change of units. Top-down emissions calculated in this work are in units of atom C $\text{cm}^{-2} \text{ s}^{-1}$, while modelled emissions are in $\text{kg cm}^{-2} \text{ s}^{-1}$. In order to calculate the top-down emissions in kg, each grid square is multiplied by its area, and then daily emissions are assumed to follow a sine wave peaking at the mid-day value. The sine wave approximates a daily insolation amplitude, allowing one to convert peak emission rates into daily emission amounts through integration. Figure 3.6 shows how the daily approximation of total emitted isoprene per grid square is calculated. Daytime hours are estimated per month, from 14 hrs (Jan) to 10 hr (Jul) (<https://en.wikipedia.org/wiki/Daytime>). This approximation is required since OMI observations occur at midday, when isoprene emissions are at their diurnal peak. GEOS-Chem emissions are similarly multiplied by area, but then integrated over time using hourly output to derive emissions in kg.

3.3 Results

Australia covers roughly $7.7 \times 10^6 \text{ km}^2$, with heterogeneous environmental conditions. The results presented in this section are therefore frequently split into five regions that are differentiated by colour, as shown in Figure 3.7. These regions are large enough to reduce the uncertainty with at least 10 grid squares in each area, and small enough to be somewhat homogeneous at the continental scale. Oceanic grid squares are filtered out of regional averages that follow.

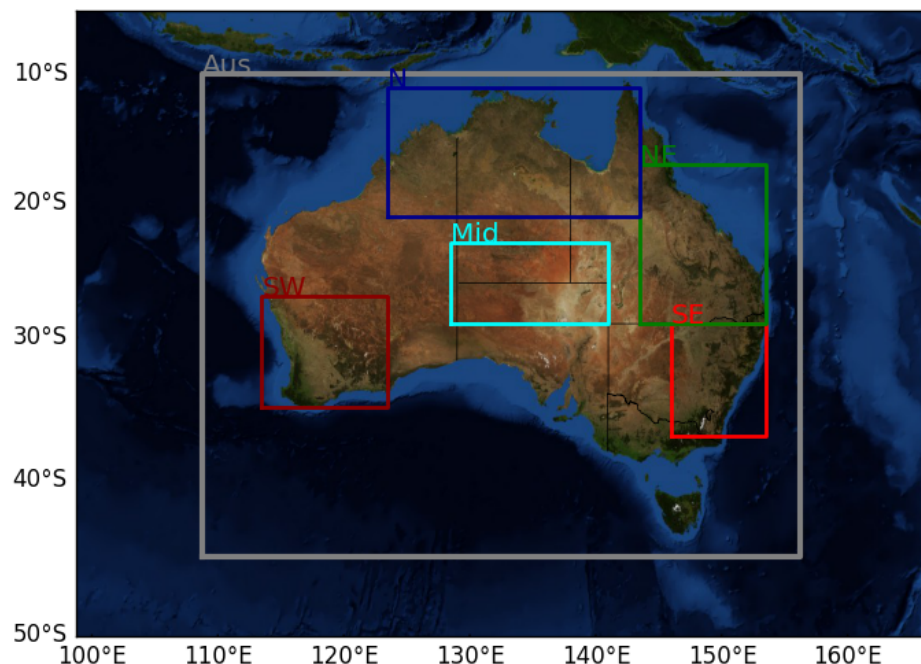


FIGURE 3.7: Sub-regions used in subsequent figures: Northern, North Eastern, South Eastern, South Western, and Middle. Australia-wide averages will be black or grey, while averages from within the coloured rectangles will match the colour shown here. Oceanic grid squares are filtered out from any area averages made in this chapter.

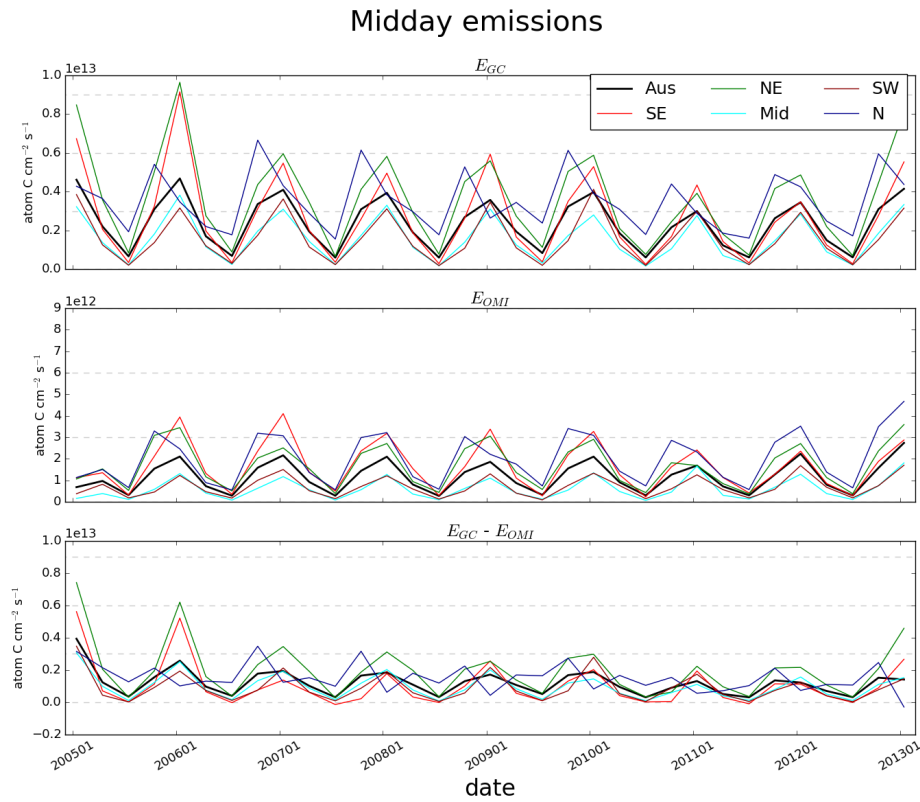


FIGURE 3.8: Row 1: Biogenic emissions of isoprene from GEOS-Chem (a priori, E_{GC}). Row 2: Emissions calculated using the OMI top-down inversion (a posteriori, E_{OMI}). Row 3: Absolute differences between the first two rows. Midday emissions are averaged for each season (DJF, MAM, JJA, SON), and colours represent averaged areas from subregions shown in Figure 3.7. Grey dashed horizontal bars are added to highlight the scale differences between rows.

3.3.1 A posteriori emissions

Figure 3.8 shows a priori emissions over Australia along with a posteriori emissions calculated as described in the prior sections. This figure shows the time series of seasonal area averaged midday emissions, and their absolute differences. Differences between a priori and a posteriori estimates are seasonally and spatially diverse. A seasonal overestimate peaking in summer can be seen in all regions except for the northern region, which is generally overestimated but less so in summer.

Figure 3.9 shows the multi-year seasonal emissions for each region for the a priori and a posteriori emissions side by side. The a priori is approximately twice that of the a posteriori. Absolute differences are highest in spring and summer, when emissions are generally greatest. The exception is the northern region, where the largest overestimates occur in spring, and large differences are seen in all seasons. Uncertainty is summarised for the a posteriori using the mean monthly uncertainty per grid square (calculated as described in 3.4.1) within each region, divided by the square root of 24 (8 years times 3 months per season). The uncertainty shown for each region is the

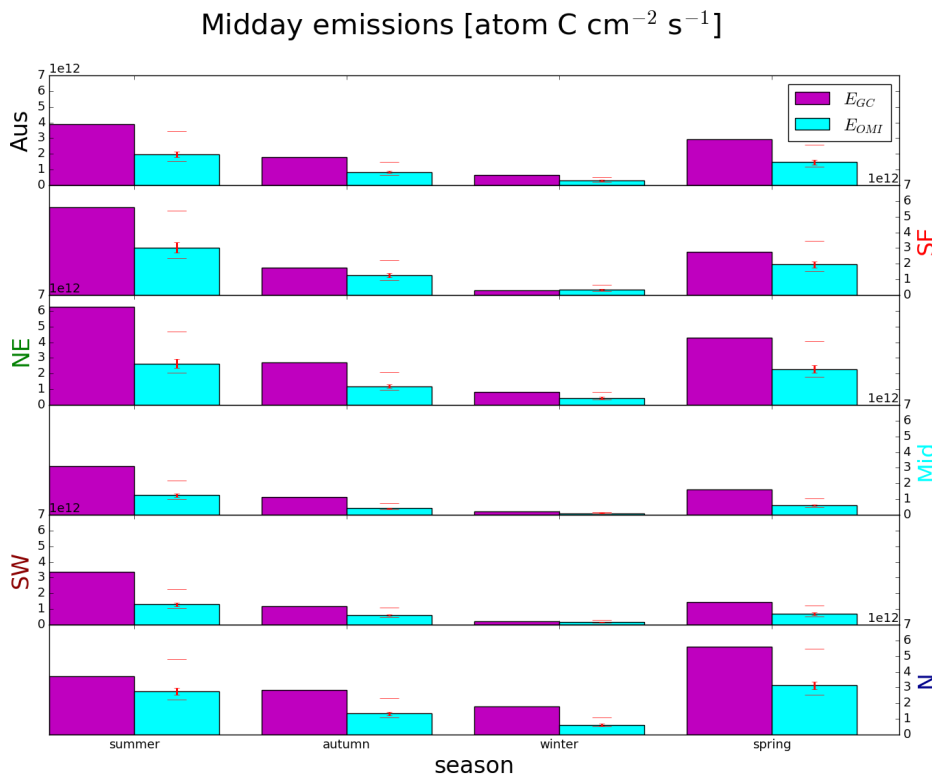


FIGURE 3.9: Regional multi-year seasonal mean a priori emissions (magenta) compared to a posteriori emissions (cyan). Error bars show the regionally averaged uncertainty (calculated as described in 3.4.1). Additional horizontal dashes show the uncertainty plus effects from potential HCHO biases (discussed in Section 3.4.1) from satellite underestimation (40%) and monthly clear sky overestimation (13%).

average over the grid squares within that region, without reduction by the square root of the number of grid squares. Uncertainty is relatively small since 8 years of data are combined into the seasonal mean. The potential bias (see Section 3.4.1) is added to the uncertainty and displayed using horizontal bars. The highest over-estimates (occurring in spring in the Northern region, and summer in all others) lie outside the potential bias caused by satellite underestimates of HCHO (Section 3.4.1). However, many overestimated seasons within each region are within this wide range of potential bias and uncertainty. Some monthly grid squares are very uncertain (> 200%) and these are removed for this plot, causing an increase in a posteriori emissions of < 1%. There are very few of these grid squares, and they appear to be grid squares with very low emission rates and low pixel counts. The cause for these highly uncertain grid squares is not analysed further, but may be worth examining in future work.

Figure 3.10 shows the multi-year monthly mean and inter-quartile range of mid-day isoprene emissions estimates in each region. Months from September to April show the most difference between a posteriori and a priori. The most overlap is seen in the south-eastern region, where high summer emissions along with high variance

occur in both the a priori and a posteriori. The highest variance is seen in both eastern regions, potentially due to diversity within the regions which include high density cities, large forests, and rural areas. This overestimate by the a priori may be caused by some mixture of overly high emission factors and high emission sensitivity to temperatures and soil moisture (Emmerson et al. 2016; Emmerson et al. 2019). Over the entirety of Australia the seasonal cycle of emissions is shown to be overestimated by the a priori, and further analysis and measurements are required to determine the cause.

While most regions show similar overestimates, the northern region of Australia follows a different cycle of bias. Northern Australian emissions appear to be overestimated throughout the year, with the smallest bias in early summer. One potential reason is that during the wet season (November-April) there are fewer satellite measurements due to increased cloud coverage, along with a different ecosystem response to sunlight and temperature (e.g., Surl, Palmer, and Abad 2018). This is evidenced by the approximately 20% lower summer OMI pixel count (before filtering) in both northern regions (see Section 3.4.3). Low measurement counts in summer in the northern region could lead to a low bias in the a posteriori emissions estimate from the drier regions associated with lower biogenic emissions being over-represented. In situ measurements in both monsoon and non-monsoon seasons are required before robust conclusions can be drawn in this region.

There is only weak correlation between daily estimates of the a priori and a posteriori ($r < 0.2$), and a priori distributions show more variance (figure in Appendix B.1). This is likely due to the filtering applied to satellite data (e.g., whenever cloud coverage exceeds 40%) which reduces the count and spread of a posteriori emission calculations. Figure 3.11 shows how the distributions of a posteriori emissions compare to a priori emissions in each region during summer months (December - February) with zeros removed from both distributions. This figure also shows the regressions between monthly averages of the same data. In the summer monthly averages, the linear regression coefficient r ranges from 0.2 to 0.81 depending on which region is being compared. The highest correlations between a priori and a posteriori emissions are in the southeast ($r = 0.81$) and southwest ($r = 0.79$) regions, followed by the northeast ($r = 0.61$) region. This is likely due to isoprene emissions in these regions being dominated by the biogenic sources (large forests) that the top-down emission estimate is based upon. Although the northern region also contains large areas of forest, the correlation is the worst. In part this is due to misrepresented forest emissions in the model, exacerbated by unrepresented responses to moisture and poorly modelled environmental stresses in this region which lies within the tropics and undergoes monsoonal weather and intense heat and drought seasons (e.g., Emmerson et al. 2016; Surl, Palmer, and Abad 2018; Emmerson et al. 2019). If the same analysis is performed over winter months, the regression in the northern region is greatly improved (to $r = 0.66$), while other regions remain approximately the same. If the modelled emissions distributions are correct (even if the absolute magnitudes are not), this suggests that satellite measurements are not capturing representative samples of monthly grid square averages in the north in summer, likely because of cloud coverage, and the summer inversion in this region may be biased.

When comparing total a priori emissions summed over Australia to the a posteriori

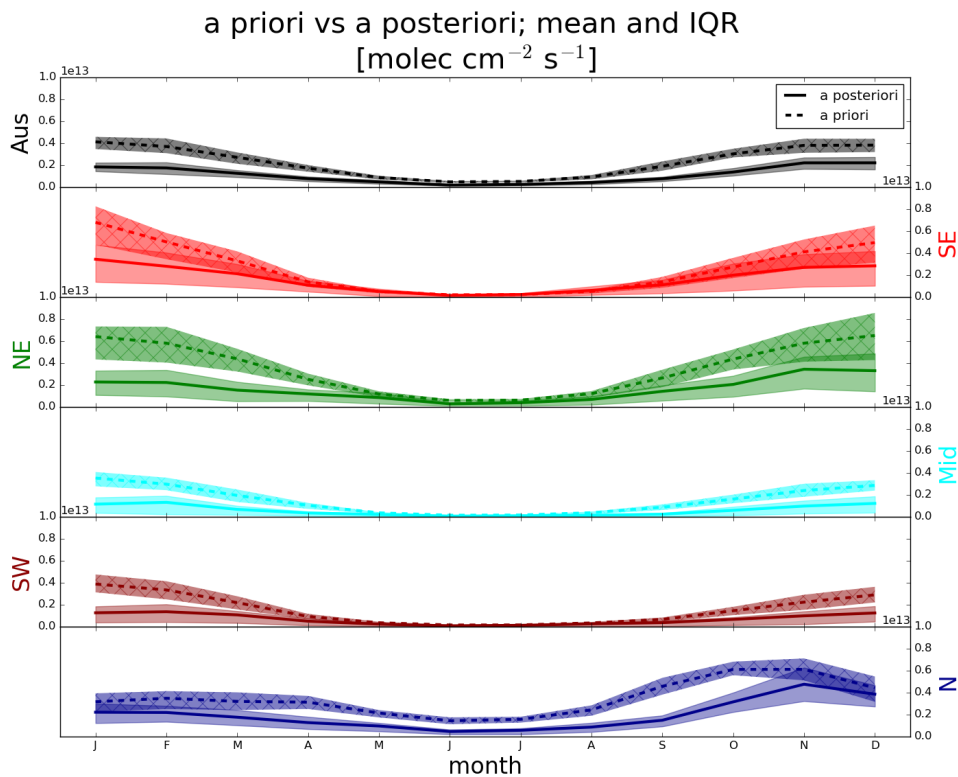


FIGURE 3.10: The multi-year monthly mean (lines) and inter-quartile-range (shaded) of midday (13:00-14:00 LT) isoprene emissions estimates. A priori emissions are shown by the dashed lines and hatched shaded areas show the inter-quartile-range. A posteriori emissions are shown using the solid lines, with inter-quartile-range shown by un-hatched shaded areas. Colours denote the region over which the multi-year monthly average was taken, as in Figure 3.7.

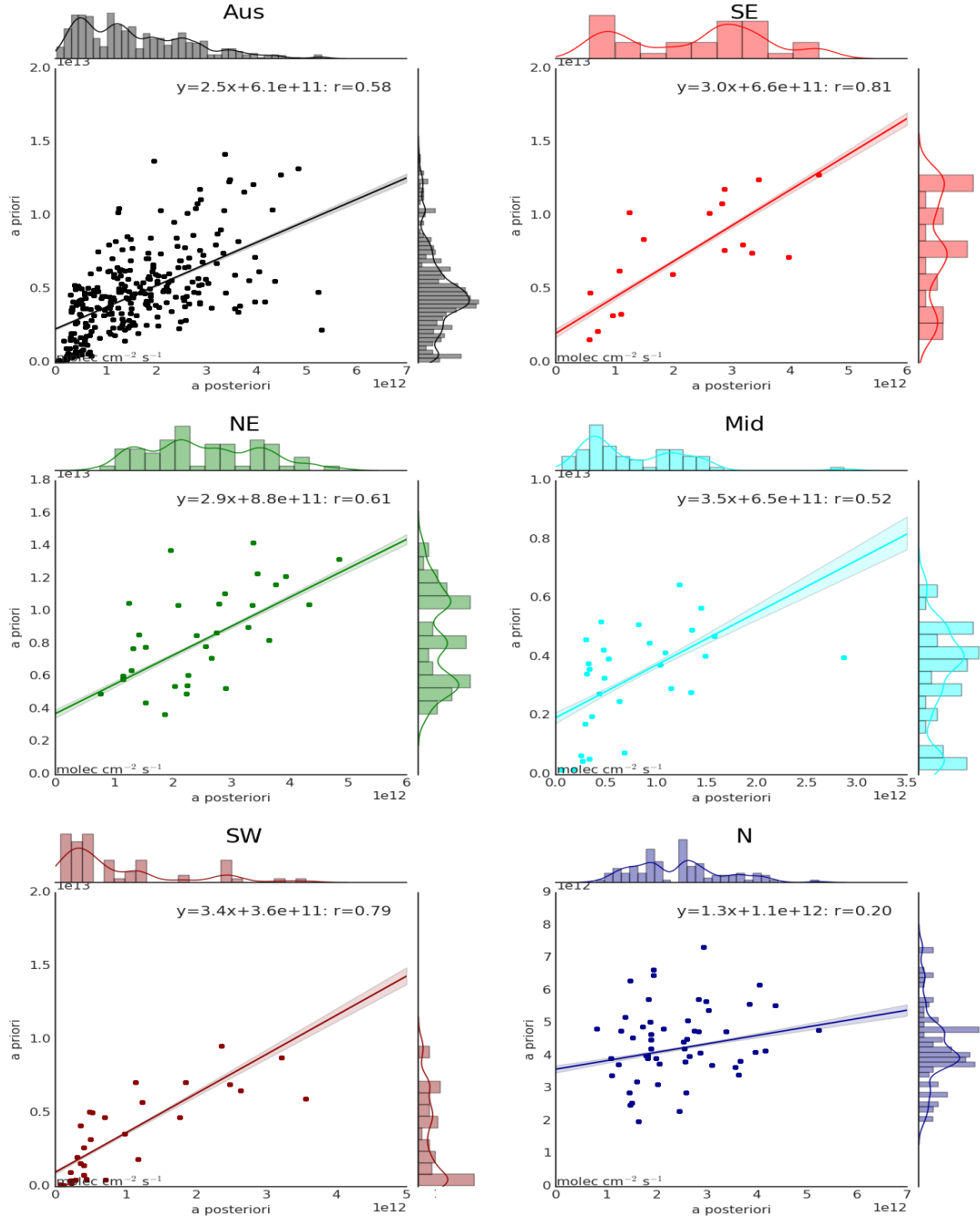


FIGURE 3.11: Scatter plot of a priori emissions against a posteriori emissions using monthly averaged grid squares as regression data points. Data points are created using monthly averages (of midday emissions) for each grid box for each month of summer (DJF) within each region shown. Multiple years of data are used, meaning if a region has 10 grid boxes, the 8 years of data will add up to $10 \text{ boxes} \times 3 \text{ months} \times 8 \text{ years} = 240$ data points minus filtered and zero emission squares. Plots are coloured by regions shown in Figure 3.7. The linear best fit regression is inset into each plot along with the line equation and regression coefficient. The normalised distribution of each population is shown at the top and right spine of each subplot, with the right spine (facing the a priori axis) using the a priori axis and scale, and the top spine using the a posteriori axis and scale.

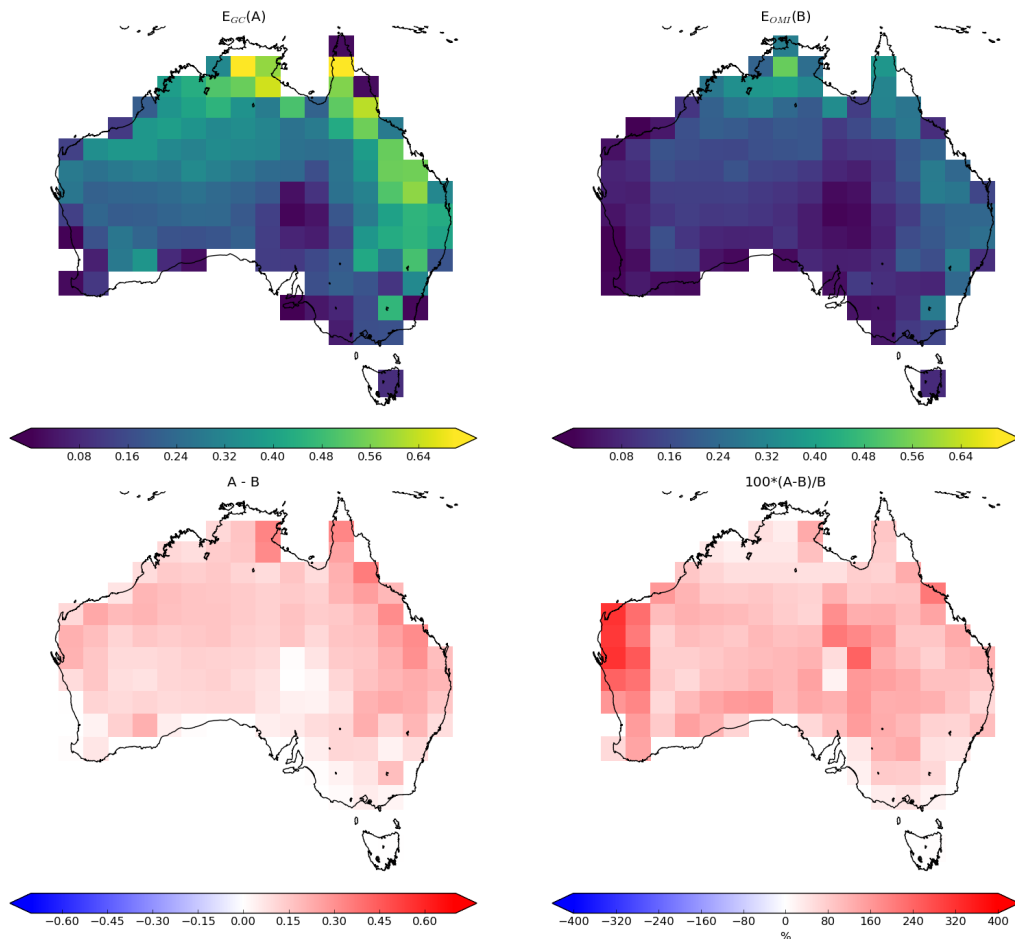


FIGURE 3.12: Top row: multi-year mean a priori emissions in Tg yr^{-1} from E_{GC} (GEOS-Chem; running MEGAN) and from E_{OMI} (top-down emissions) respectively. The total flux from E_{OMI} is calculated assuming a sinusoidal daily cycle, with daylight hours prescribed for each month as described in Section 3.2.8). Bottom left and right show the absolute and relative differences, respectively.

calculated using the top-down inversion, a decrease of $\sim 46\%$ from 39 Tg yr^{-1} to 21 Tg yr^{-1} is apparent. Table 3.1 compares annual Australian isoprene emissions estimated in this work to previously published values. The a posteriori estimated here to be 21 Tg yr^{-1} suggests isoprene emissions may be lower than all prior bottom up estimates. This, and is close to the lowest top-down estimate of Bauwens et al. (2016) of 26 Tg yr^{-1} . Figure 3.12 shows how this decrease is distributed spatially, with E_{GC} and E_{OMI} in Tg yr^{-1} calculated as a multi-year mean. Across all of Australia large reductions of total emissions are seen using the new top-down estimate.

TABLE 3.1: Isoprene emissions (Tg/yr) from Australia

Estimate ^a	Source	Year	Reference
39.2(4.0)	bottom-up	2005-2012	This thesis ^b
~ 80	bottom-up	1980-2010	Sindelarova et al. (2014) ^c
26-94	bottom-up	2005-2013	Bauwens et al. (2016) ^d
20.7(1.6)	top-down	2005-2012	This thesis ^e
36	top-down	2005-2013	Bauwens et al. (2016) ^f

a: Interannual standard deviation shown in parentheses.

b: GEOS-Chem with MEGAN diagnostics based on 3-hourly averages.

c: MEGAN run using MERRA meteorology.

d: Range shown here based on three models, two of which implement MEGAN.

e: Based on daily peak emissions integrated over a sinusoidal daily curve.

f: OMI based top-down inversion.

3.3.1.1 Diurnal variability

Figure 3.13 shows the a priori daily emissions cycle for Australia compared to the estimated a posteriori emissions cycle over Australia. The conversion of midday a posteriori emissions ($\text{molec cm}^{-2} \text{ s}^{-1}$) into Tg yr^{-1} involves integration over an assumed sinusoidal diurnal emission cycle as described in Section 3.2.8. A priori emissions peak from approximately 11:00 LT to 16:00 LT, while outside these hours there is a non-sinusoidal drop in emissions to below the assumed a posteriori diurnal emission cycle. This means the conversion may be biased by this consistent difference between modelled a priori diurnal emission cycles and the assumed diurnal a posteriori cycle. This potential bias is not analysed further, and should be relatively small compared to other uncertainties as it only affects emissions towards the daily minima.

3.3.1.2 Trends

Figure 3.14 shows monthly deseasonalised a priori and a posteriori midday emission anomalies for each region. First the emissions are spatially averaged within each region to form a daily time series of midday emission rates. These are averaged into monthly data, and then the multi-year monthly mean is subtracted to form the anomaly time series. Any anomaly greater than three standard deviations from the mean is removed (crosses in Figure 3.14). An ordinary least squares linear regression is then performed to look for any significant trend. A trend is considered significant if the p-value from a Wald test (equivalent to a t-test) is less than 0.05. Trend results for isoprene are summarised in Table 3.2. The a priori midday surface isoprene concentrations show a small decline outside of the southwest region over the 8 year period from 2005-2012. This decline reduces in scale by approximately a factor of 2-3 in the a posteriori emissions. There is no significant change in trend due to scaling isoprene emissions. Since the scaling factor α is applied to each grid square seasonally and not changing each year, changing trends are not expected.

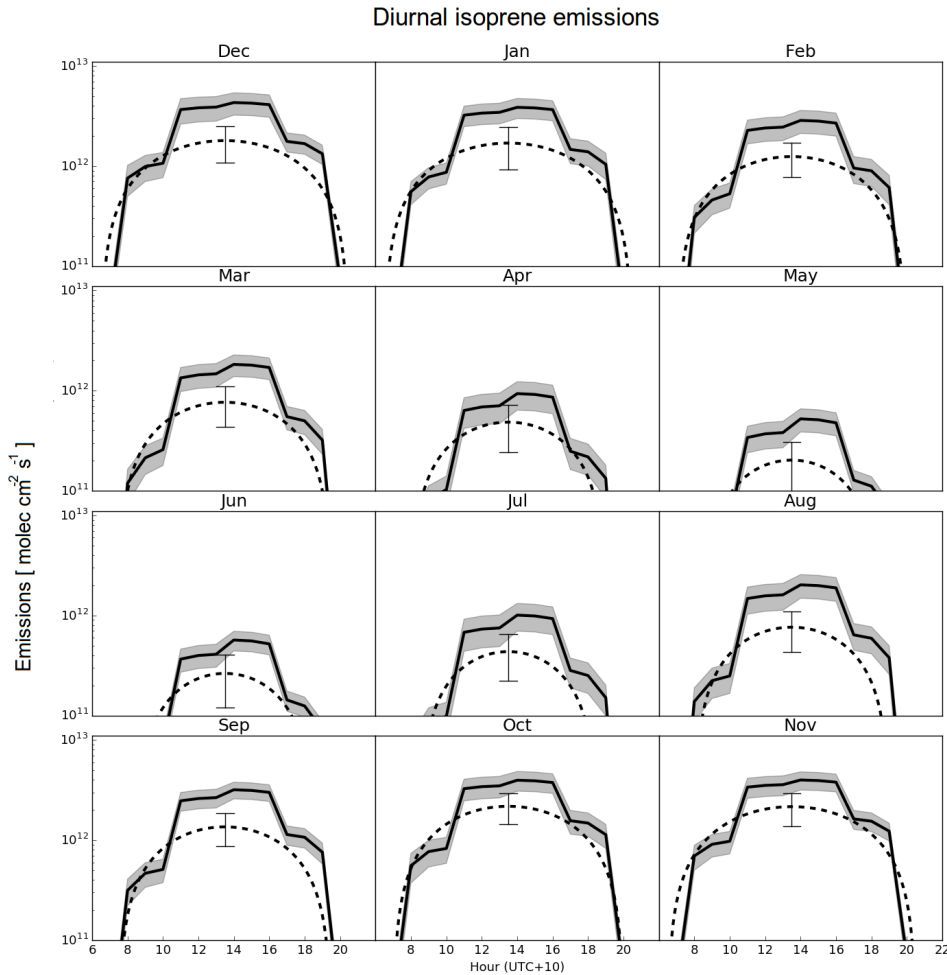


FIGURE 3.13: The diurnal cycle of GEOS-Chem a priori emissions (solid line) averaged by month into hourly bins over from 2005 to 2013 along with top-down a posteriori (dashed line) emissions. Standard deviations for the monthly average are shaded for the a priori, and shown with error bars at 13:30 LT for the a posteriori. Top-down emissions shown here are based on monthly midday emissions being the peak of a sine wave which drops to zero after and before daylight hours (see Section 3.2.8).

TABLE 3.2: 2005-2012 trend^a in surface isoprene mixing ratio (ppbvC yr⁻¹) from simulations using a priori and a posteriori isoprene emissions.

Region	a priori	a posteriori
Aus	-.04	-.02
SE	-.15	-.07
NE	-.13	-.04
Mid	-.07	-.02
SW	-.01	-.01
N	-.06	-.02

a: Statistically significant (two sided test with $\alpha = 0.1$) trends are bolded.

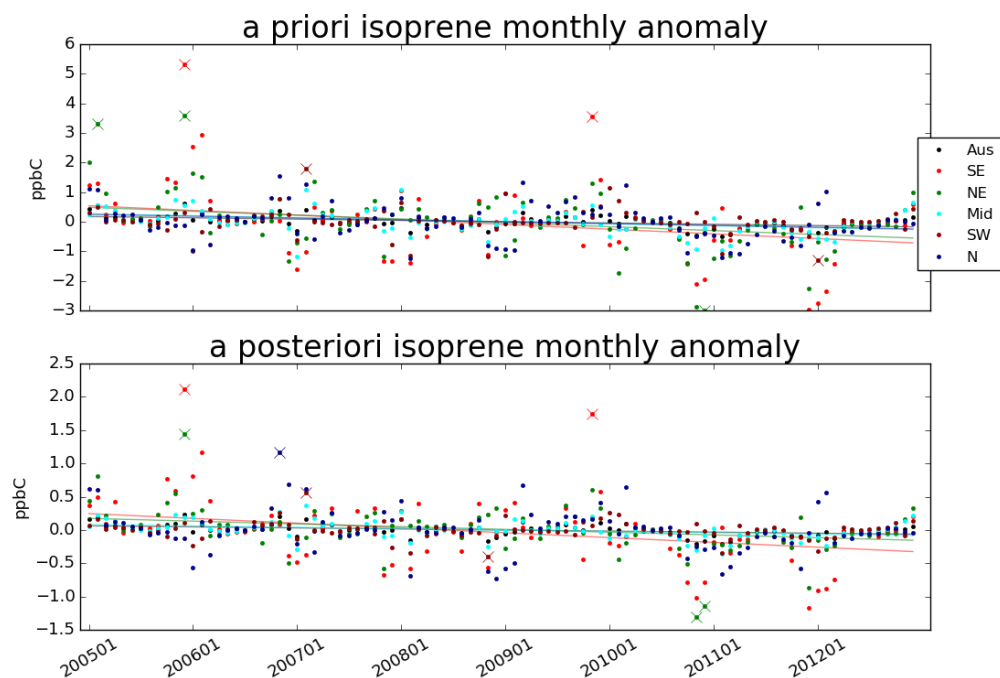


FIGURE 3.14: A priori (row 1) and a posteriori (row 2) monthly emissions anomalies from multi-year monthly mean, split by region (see Figure 3.7).

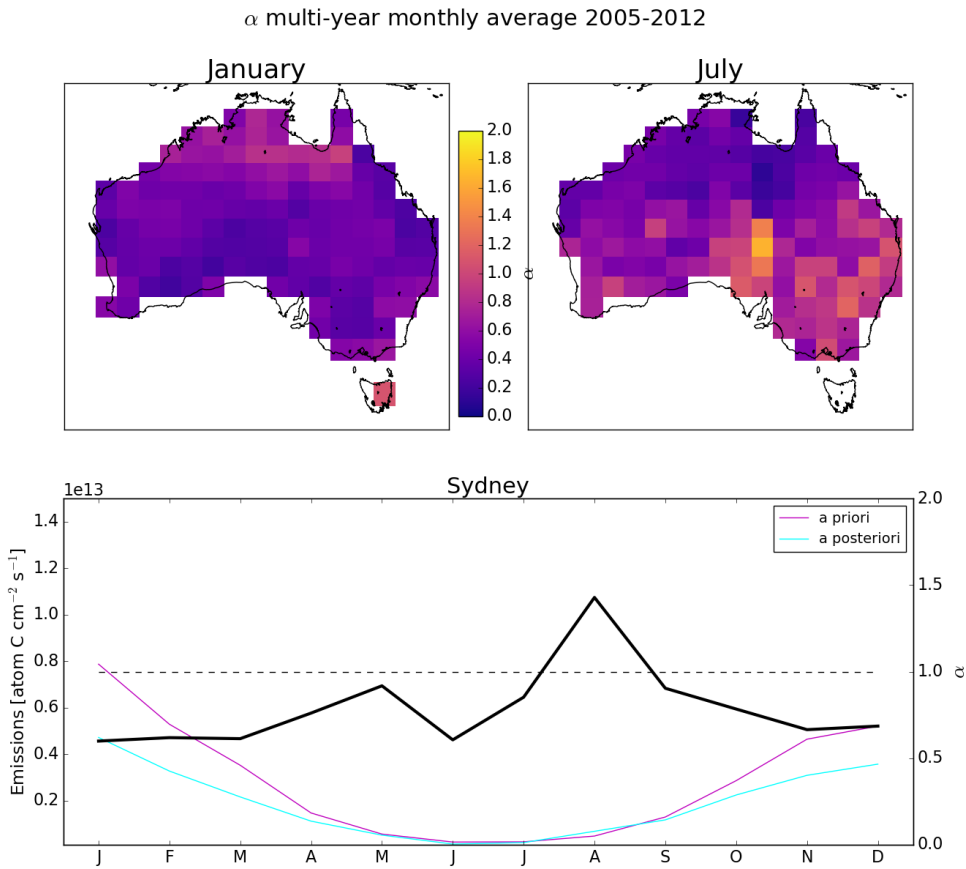


FIGURE 3.15: Row 1: Isoprene emissions scaling factor α for the average January (left) and July (right) over 2005-2012. Row 2: a priori (magenta, left axis), a posteriori (cyan, left axis), and α (black, right axis) multi-year monthly averages calculated for the $2^\circ \times 2.5^\circ$ grid box containing Sydney.

3.3.2 Modelled impacts of reduced isoprene emissions

This section uses GEOS-Chem to determine how the improvements to biogenic isoprene emissions impact subsequent atmospheric chemistry and composition. A posteriori emissions are implemented in GEOS-Chem as described in Section 3.2.8. Outputs from the scaled GEOS-Chem run using the a posteriori are denoted by superscript α . For example, column HCHO from GEOS-Chem before and after scaling are denoted Ω_{GC} and $\Omega_{\text{GC}}^\alpha$ respectively. Figure 3.15 shows α for January and June averaged over 2005-2012, along with the time series of E_{GC} and E_{OMI} and α calculated for the $2^\circ \times 2.5^\circ$ grid box containing Sydney and their multi-year seasonal average. GEOS-Chem emissions are scaled according to this multi-year averaged gridded α , which is seasonal and spatially diverse.

3.3.2.1 Implications for HCHO

As a preliminary check on the GEOS-Chem output, simulated Ω_{GC} and Ω_{GC}^α are compared to Ω_{OMI} over January and February, 2005 in Figure 3.16. In every region, Ω_{GC}^α is closer to Ω_{OMI} with biases decreasing from $\sim 100\%$ to $\sim 50\%$ everywhere except the northern region, which has biases decreasing from $\sim 50\%$ to $\sim 25\%$. Note that this is not an independent validation as Ω_{OMI} drive the creation of Ω_{GC}^α , and as is expected the relationship is much improved. The remaining differences are most likely driven by filtering and temporal averaging of the applied scaling factor α . When looking over all of Australia from 2005-2012, the summer mean decreases from 9.8×10^{15} to 7.4×10^{15} molec cm $^{-2}$ after scaling isoprene emissions, while the satellite column is 4.9×10^{15} .

Figure 3.17 shows HCHO is most reduced in summer for the majority of Australia. In winter, a reduction is seen along the northern coast of Australia, most likely because emissions in this area are less affected by the seasonal decline. Seasonal means and the standard deviations (between all grid boxes and days used in averaging) for each region are summarised in Figure 3.18. Both mean and variance are reduced after running GEOS-Chem with scaled isoprene, although the mean is lower still in OMI vertical columns. Model output standard deviations in summer range from $\sim 20 - 30\%$, while OMI standard deviations range from $\sim 32 - 41\%$. The highest OMI standard deviations occur in winter, ranging over $\sim 46 - 73\%$, which is the opposite of model output with standard deviations between $\sim 12 - 27\%$. This could be an effect of the increased winter uncertainty in satellite output, which is amplified by the low column amounts in the season. Overall the standard deviation within model output appears to be too low in all regions, ranging from three quarters (south eastern region) to one fifth (middle region) of the standard deviations within the OMI HCHO column output. These standard deviations are formed from the monthly averaged grid boxes used to create each multi-year seasonal mean. Their low value (relative to satellite measurements) suggests that the model does not capture the full range of variance over time and space of HCHO levels over Australia; however, variance is heightened in satellite measurements due to the filtering that reduces the number of grid squares that form the multi-year seasonal mean.

Decreasing isoprene emissions in the model lead to reduction in HCHO concentrations as one would expect. Figure 3.19 shows an example (over Wollongong) of the modelled HCHO profile before and after scaling isoprene emissions. This reduction of HCHO is greatest at the surface, and is highly correlated ($r > .8$) in all regions to the reduction in isoprene emissions. The high correlation is effectively a sanity check of the top-down method used in this thesis to estimate isoprene emissions.

3.3.2.2 Implications for ozone

Isoprene oxidation can eventually lead to ozone formation, especially when isoprene-enriched air masses mix with polluted urban air masses that contain high NO_x. Figure 3.20 shows surface level (up to ~ 150 m altitude) ozone concentrations over 2005 before and after scaling modelled isoprene emissions. Reducing isoprene emissions lowers surface ozone concentrations by ~ 1 ppbv in all regions in all seasons. The largest reductions (~ 3 ppbv) occur in the northern region in spring. A regression between

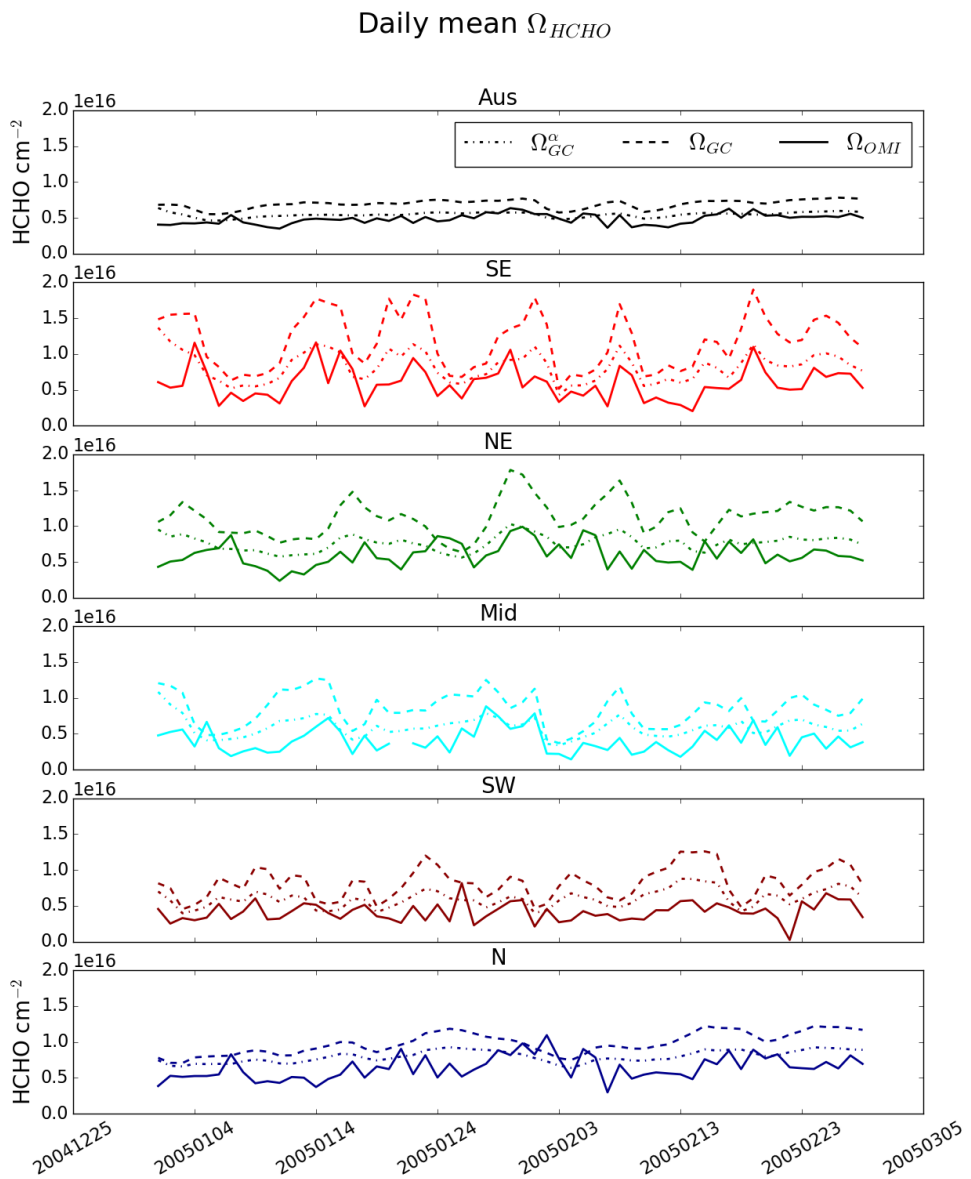


FIGURE 3.16: Daily mean total column HCHO amounts from GEOS-Chem with a priori (new emissions run) and a posteriori (tropchem run) a posteriori scaled isoprene emissions, along with the recalculated OMI HCHO columns. Each row shows the average over regions in Figure 3.7.

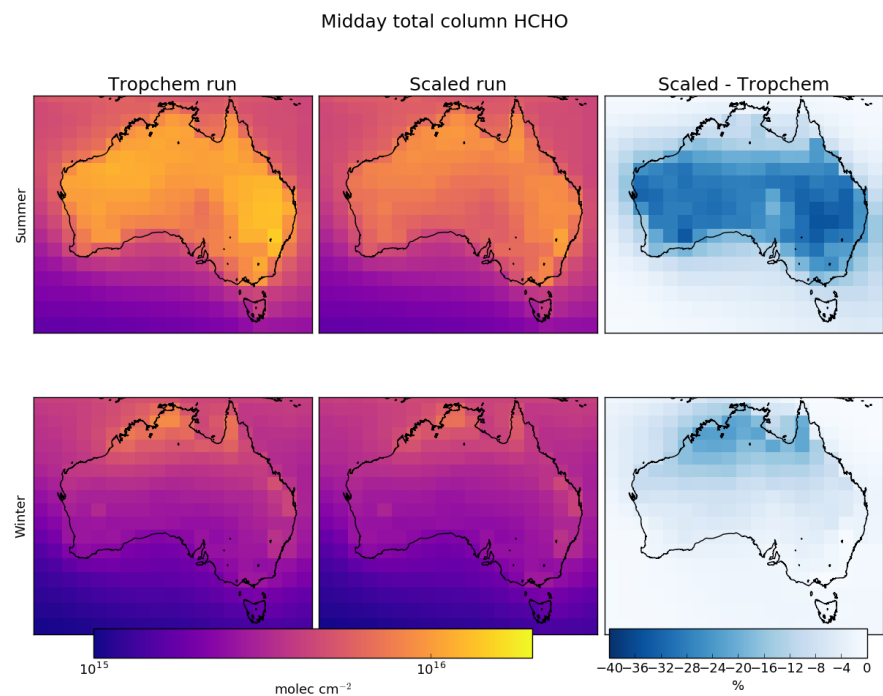


FIGURE 3.17: Total column HCHO a priori (left) and a posteriori (middle) isoprene emissions, and their relative differences (right). Top row shows summer (DJF) averaged total columns, while bottom row shows the winter (JJA).

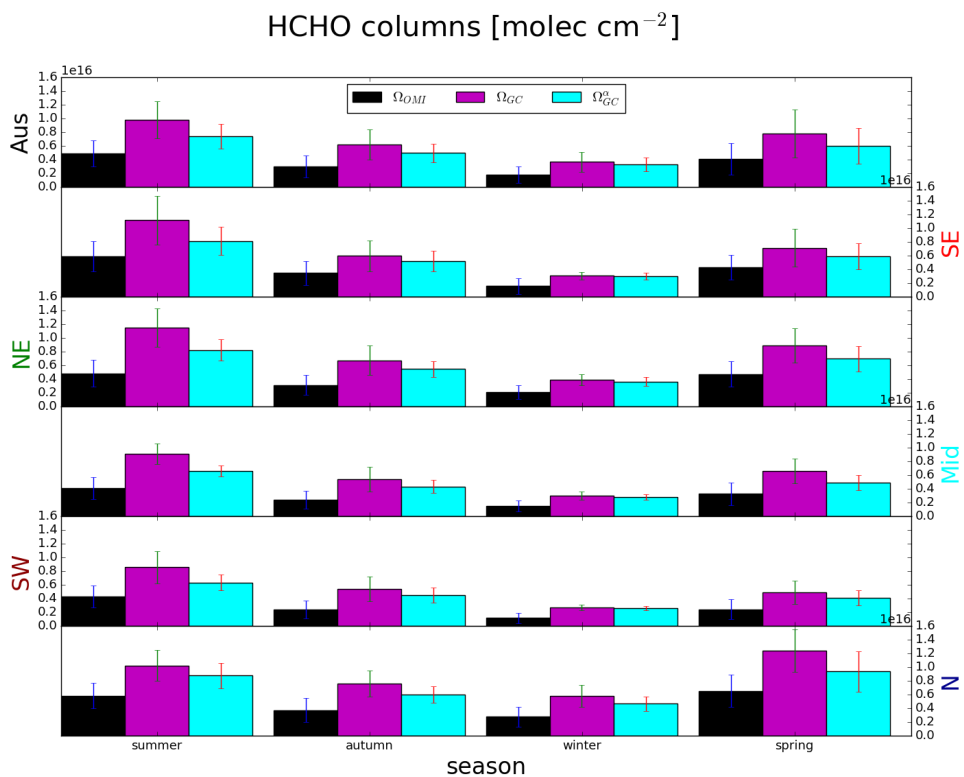


FIGURE 3.18: Regionally and seasonally averaged HCHO total columns from GEOS-Chem (Ω_{GC} , and Ω_{GC}^a) and recalculated OMI measurements (Ω_{OMI}) side by side. Each row represents one region within Australia, while each column represents from left to right: summer, autumn, winter, spring. Standard deviations between grid boxes used to form the multi-year seasonal average are shown with error bars.

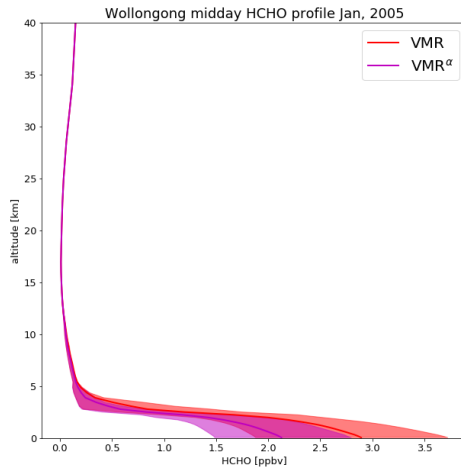


FIGURE 3.19: Monthly averaged HCHO profile over the $2^\circ \times 2^\circ$ grid box containing Wollongong modelled by GEOS-Chem before (VMR) and after (VMR^α) scaling isoprene emissions. Shaded areas represent the inter-quartile range over the month.

the change in isoprene emissions, and the change in surface ozone was performed (as in the prior section with HCHO); however, only very weak correlations between reductions are apparent. While the overall decrease in surface ozone is clear, there is no direct correlation between monthly grid square averaged reductions in isoprene emission and surface ozone concentrations in the same grid square. This suggests that changes in isoprene emissions affect ozone in non-local grid squares due to transport, including grid squares where absolute emission reductions are not as strong.

Ozone and fine particulate concentrations in Australian cities have not reduced over the last 10 years, unlike other atmospheric pollutants such as CO, NO₂, and SO₂ (Keywood, Emmerson, and Hibberd 2016). This could be in part due to the downwind effects of isoprene emission, which are most likely to affect suburban fringes (e.g. western Sydney) of Australian cities which are surrounded by vegetation (Millet et al. 2016). Outside of densely populated regions, Australia is likely to be NO_x-limited and changes in VOC emissions will have less of an impact on ozone production. Here the modelled ozone output is averaged over large areas that are mostly non-urban, which means detected ozone sensitivity to isoprene emissions is likely underestimated for cities. Figure 3.21 shows how ozone is reduced in summer and winter after scaling isoprene emissions. In summer, reductions are strongest in Sydney and Melbourne, but can also be seen in the west coast and central Australia. Winter reductions are more uncertain (relatively); however, they are strongest in the coastal and oceanic regions around Darwin. In future work, the estimated emissions will be downscaled to better evaluate their impacts on ozone in different NO_x regimes (for instance over cities).

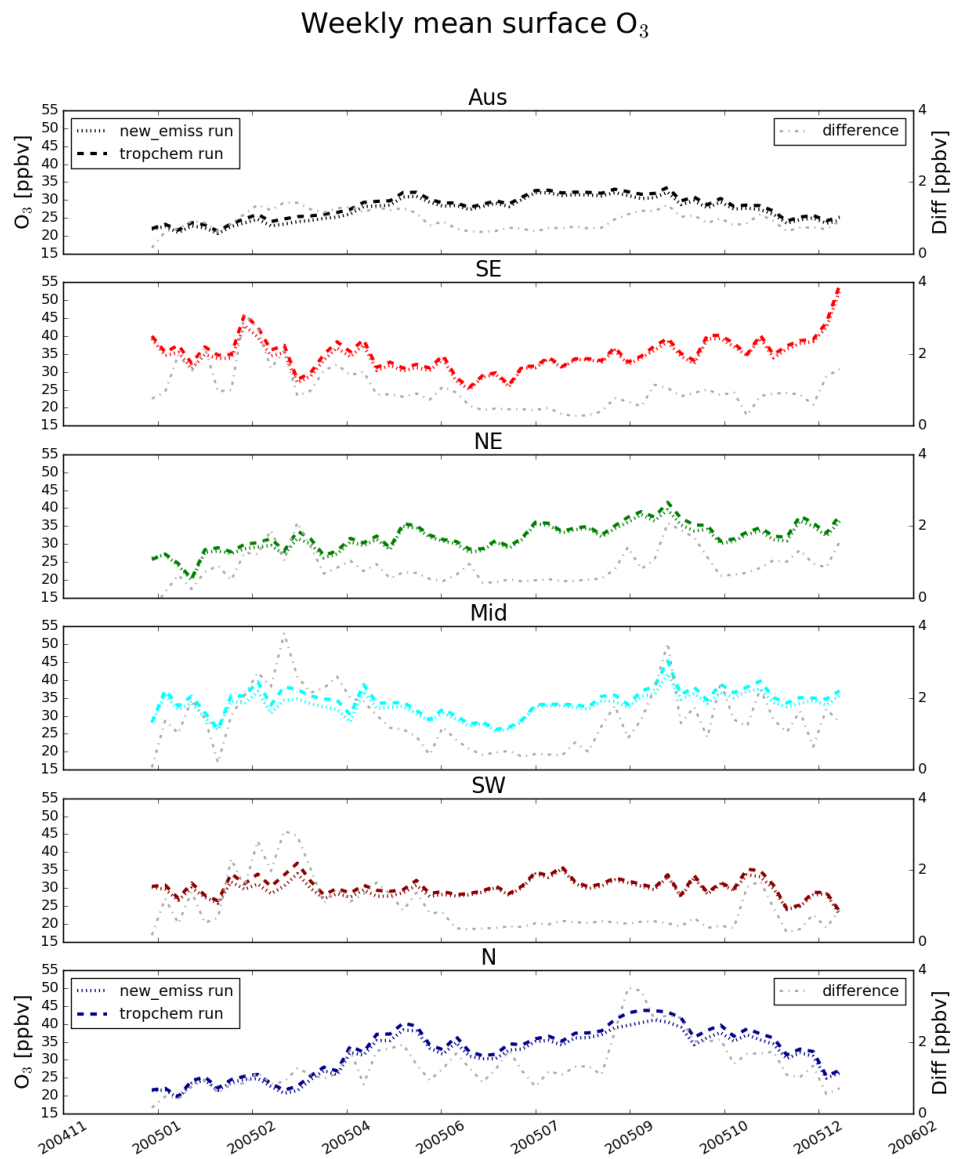


FIGURE 3.20: Surface ozone concentrations (ppb) per region over 2005. Concentrations are shown using the left axis, and absolute differences (tropchem run - scaled run) shown in grey using the right axis.

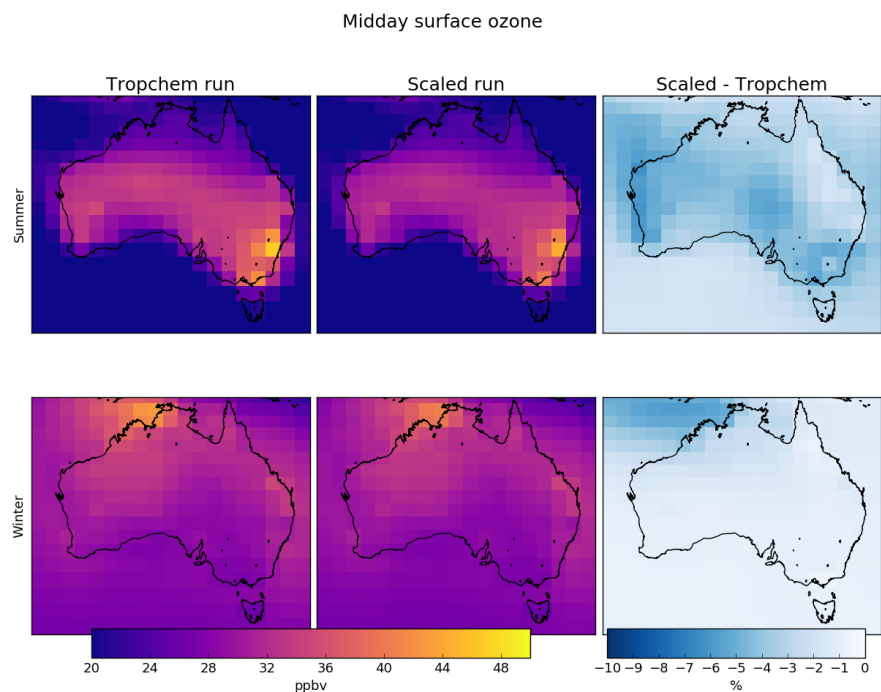


FIGURE 3.21: Multi-year seasonal surface (up to ~ 150 m) ozone before (left) and after (middle) scaling isoprene emissions, and their relative differences (right). Top row shows summer (DJF) averaged total columns, while bottom row shows the winter (JJA).

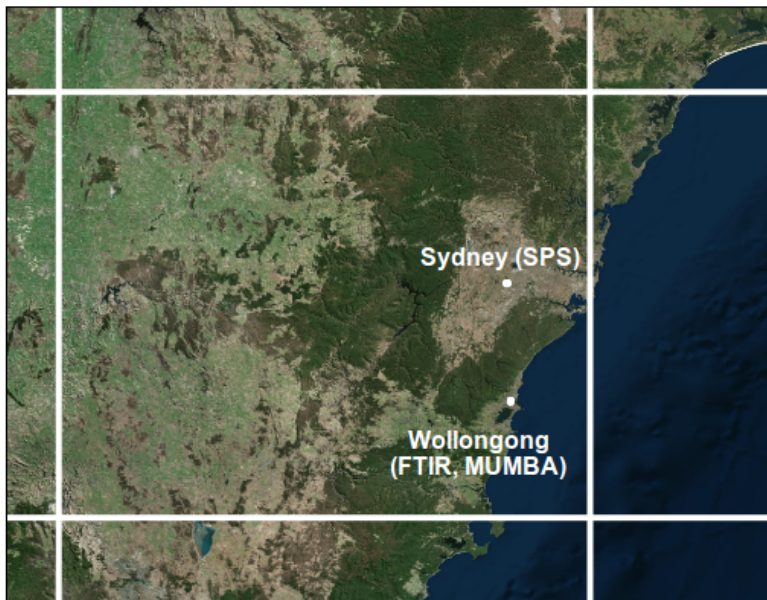


FIGURE 3.22: GEOS-Chem grid box ($2^\circ \times 2.5^\circ$) containing Wollongong FTIR, SPS, and MUMBA campaign data.

3.3.3 Comparison with in situ measurements

Comparison between ground-based measurements and large ($2^\circ \times 2.5^\circ$) averaged model output suffers from representation error. Figure 3.22 shows the SPS and MUMBA measurement campaigns (see Section 2.2), along with the extent of the relevant $2^\circ \times 2.5^\circ$ GEOS-Chem grid box, a rectangle with edge lengths of roughly 200 km^2 . The urban footprint of Sydney and Wollongong can be seen, along with ocean, forest, and rural regions, which will all affect the model output as it is based on the average of inputs within the grid box. Due to high uncertainty in components of the top-down emissions estimate, temporal resolution is also limited. MUMBA (Section 2.2.3.1), SPS1 and SPS2 (Section 2.2.3.1) provide approximately one month (two for MUMBA) of hourly or daily data, which are compared in this section against surface level concentrations from GEOS-Chem (midday output) before and after scaling the biogenic emissions.

Figure 3.23 shows GEOS-Chem output in the grid square containing Sydney and Wollongong campaign measurements. Measurements between 13:00 and 14:00 are averaged daily. In order to minimise introduced bias, any measurements below the instrument detection limit are set to half of the detection limit, as performed in Lawson et al. (2015). Midday measurements from MUMBA (summer, Wollongong) compared against SPS (summer, autumn, Sydney) show lower isoprene and HCHO levels, and similar ozone levels, and also lower variance across all three species. Variation in SPS

TABLE 3.3: Campaign measurements compared to model output [ppb].

	SPS1			SPS2			MUMBA		
	mean	RMSE	r	mean	RMSE	r	mean	RMSE	r
Isoprene									
Meas	1.16			0.46			0.47		
GC	1.34	0.89	0.83	0.24	0.36	0.44	1.87	1.66	0.52
GC ^a	0.67	1.15	0.84	0.18	0.39	0.43	0.93	0.73	0.49
HCHO									
Meas	3.92			2.02			1.41		
GC	2.38	2.63	0.47	1.28	1.28	0.77	3.00	1.97	0.44
GC ^a	1.83	3.01	0.54	1.19	1.35	0.78	2.21	1.17	0.47
Ozone									
Meas	30.14			22.71			24.59		
GC	40.91	15.46	0.52	33.75	13.59	0.35	49.97	28.01	0.34
GC ^a	39.20	14.23	0.54	32.81	12.69	0.36	47.14	24.91	0.36

Meas: Measurements (midday means)

GC: GEOS-Chem (tropchem run)

GC^a: (GEOS-Chem scaled run)

data are higher than modelled, which is likely due to a dependence on local meteorology, as plumes of HCHO or isoprene enriched air can be detected as they pass by while the modelled grid square averages these out. This higher variance is not seen in the MUMBA midday observations; however, this may be due to the small sample size of the measured data.

Coincident measured and modelled means and comparison statistics for each campaign for isoprene, HCHO, and ozone are summarised in Table 3.3. Isoprene correlations are greatest during the SPS1 campaign at $r = 0.83, 0.84$, nearly double those of SPS2 and MUMBA. The root mean square error (RMSE) in MUMBA is 1.7 ppb ($\sim 300\%$) and approximately 0.9 ppb and 0.4 ppb in SPS1, SPS2 respectively ($\sim 100\%$), before isoprene scaling is applied. In MUMBA the reduced isoprene emissions improves the model drastically, bringing the RMSE down to $\sim 100\%$, however this improvement is not seen in either of SPS1 or SPS2. Similarly for HCHO, the MUMBA RMSE is reduced from 2.0 ppb ($\sim 130\%$) to 1.2 ppb ($\sim 80\%$) by bringing down the mean modelled amounts. Modelled HCHO is low compared against measurements from Sydney (SPS1 and SPS2), and is further lowered through scaling. Without improved model resolution or further measurements, this is assumed to be due to local influences seen in the measurements but not captured by the model, such as HCHO enriched air from local sources. Modelled ozone concentrations are slightly reduced (3 – 8%) when scaling isoprene emissions, however the concentrations remain 30 – 50% too high for Sydney and approximately 100% too high for Wollongong. This is likely due to the reduced ozone concentrations in cities compared to regional areas, as the modelled ozone concentrations are averages over the larger area which is mostly non-urban.

A spectrometer (FTIR) on the roof of the Chemistry building at the University of

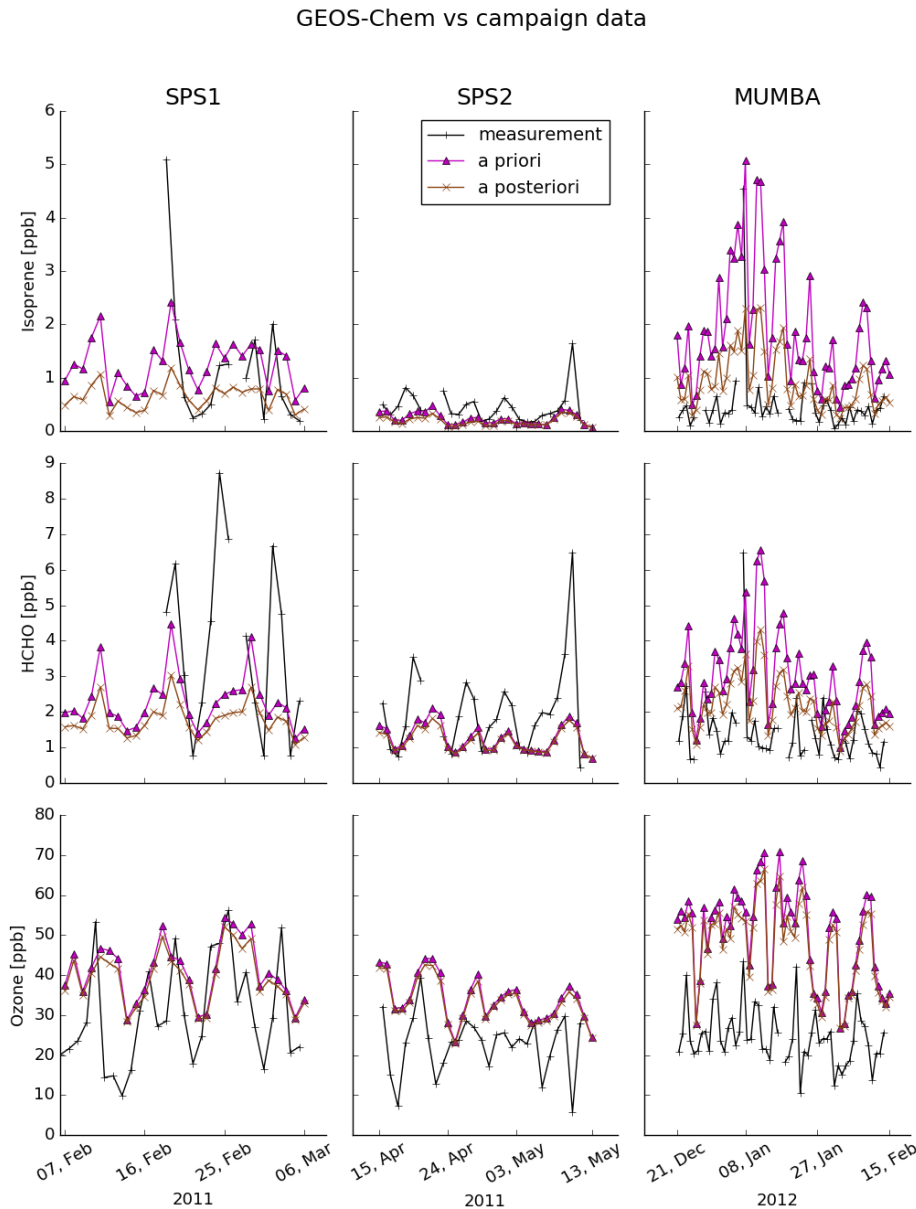


FIGURE 3.23: SPS1, SPS2, and MUMBA (left to right columns respectively) midday (13:00–14:00 local time) measurements of isoprene, HCHO, and ozone (top to bottom rows respectively). Shown in magenta and brown are the a priori and a posteriori GEOS-Chem surface outputs for the matching grid square at midday for days containing measurements.

TABLE 3.4: Mean total column HCHO amounts in 10^{15} molec cm^{-2} at Wollongong.

Season	Ω_{FTIR}	Ω_{GC}	Ω_{GC}^α
summer	15.4	17.7	13.6
winter	3.68	4.41	4.49

Wollongong measures total column HCHO in the atmosphere during clear sky conditions. This is the only non-satellite long-term measurement record of total column HCHO available in Australia (see Section 2.2.3.3). In order to compare modelled profiles against retrievals from the FTIR, modelled profiles are first convolved with the instrument averaging kernel and a priori. FTIR output is resampled to only include measurements taken at midday (13:00-14:00) and GEOS-Chem overpass outputs are interpolated onto matching vertical levels for days where FTIR output exists. Figure 3.24 shows total column HCHO from FTIR, and from GEOS-Chem before and after scaling isoprene emissions. While the comparison suffers from representational error between FTIR measurements and GEOS-Chem output (see Figure 3.22), one can see that the summer overestimate of HCHO from GEOS-Chem is removed by isoprene scaling. The mean summer underestimate of HCHO shown after scaling makes more sense due to the relatively dense forested areas around Wollongong, which would raise local HCHO concentrations above the average for the large grid square represented by GEOS-Chem. Another feature is the January and December dip in all three datasets. The FTIR has a lower data count and higher variance in these (holiday) months as measurements involve manual processes, increasing uncertainty for the measurements. Analysis of this dip could be performed in future work; however, it would require an in depth examination of local and synoptic HCHO patterns, and higher resolution model data. Seasonal mean HCHO from the FTIR measurements and co-located, convolved, and resampled model output is summarised in Table 3.4. The original modelled summer vertical column is higher than the FTIR measurements by $\sim 15\%$, which decreases with isoprene scaling to $\sim -12\%$. In winter the column is modelled high by $\sim 20\%$, which increases to $\sim 22\%$ after scaling.

3.4 Uncertainty

This section identifies and quantifies the overall uncertainties of calculating isoprene emissions using OMI HCHO observations and the GEOS-Chem model in the top-down method used in this chapter. However, these uncertainties lack verification against measurements. Even as the top-down inversion performed in this chapter attempts to work around the lack of measurements over Australia, it suffers from the lack of independent observations against which it can be verified.

The major source of uncertainty throughout the year comes from uncertainty in the modelled yield slope S (see Section 3.4.2); however, in winter, uncertainty from satellite column calculation becomes dominant (see Section 3.4.3). Monthly calculated slope uncertainty mostly lies within 30% to 50%, and for each grid box a month of

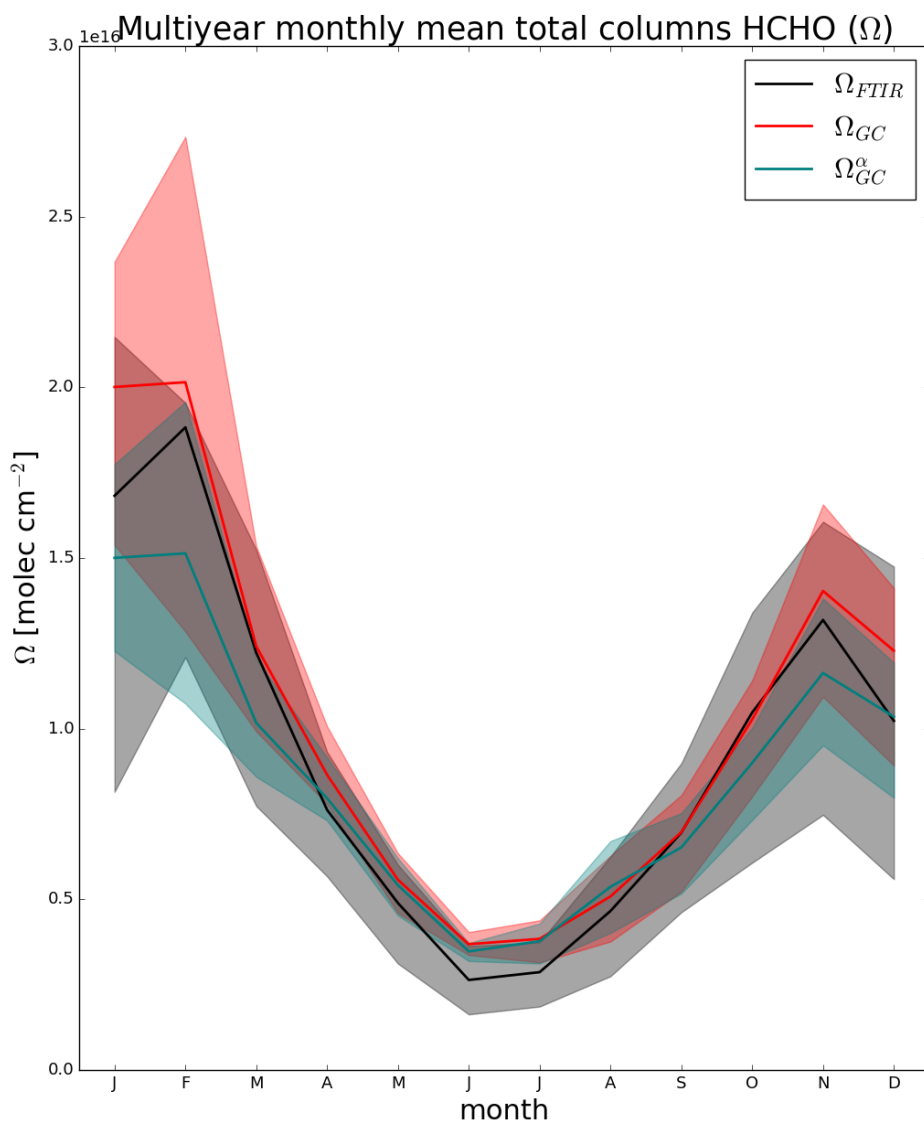


FIGURE 3.24: Multi-year (from all days where both measurements and model data exist: 2007–2012) monthly mean total column (Ω) HCHO from the FTIR instrument at Wollongong (southeast Australia), and the colocated convolved GEOS-Chem equivalent before (Ω_{GC}) and after (Ω_{GC}^α) scaling isoprene emissions. Shaded areas show inter quartile range.

TABLE 3.5: Relative uncertainty estimates.

Region	Summer			Winter		
	$\frac{\Delta E_{OMI}}{E_{OMI}}$ a	$\frac{\Delta \Omega_{OMI}}{\Omega_{OMI}}$	$\frac{\Delta S}{S}$	$\frac{\Delta E_{OMI}}{E_{OMI}}$ a	$\frac{\Delta \Omega_{OMI}}{\Omega_{OMI}}$	$\frac{\Delta S}{S}$
Aus	46%	21%	36%	51%	258%	35%
SE	54%	14%	37%	66%	141%	38%
NE	53%	18%	35%	51%	40%	37%
Mid	45%	38%	38%	47%	41%	35%
SW	43%	27%	32%	61%	96%	36%
N	39%	16%	33%	38%	22%	30%

a: Grid squares with monthly uncertainty over 200% are removed when calculating the mean uncertainty, which has small (< 1%) impacts on E_{OMI} overall, but removes many data points in winter.

model data is used, which means that slope uncertainty is not reduced by monthly averaging. Uncertainty from each OMI satellite measurement is relatively large ($> 100\%$); however, averaging thousands of pixels in each grid square greatly reduces the monthly uncertainty. Uncertainty in satellite HCHO is seasonally dependent, with better signal during the summer. Reliable OMI measurements are less frequent (leading to higher uncertainty) at high solar zenith angles, which are more frequent at higher latitudes and during winter. Table 3.5 shows the estimated uncertainty calculated in this work in summer and winter over each region described by Figure 3.7. The assumptions and calculations made to determine uncertainties in the top-down estimate (ΔE_{OMI}), the satellite column ($\Delta \Omega_{OMI}$) and the slope (ΔS) are described in the following subsections.

3.4.1 Top-down emissions

Important factors in the calculation of isoprene emissions using OMI HCHO include the modelled relationship between HCHO and isoprene and the satellite HCHO measurements. Uncertainty in each of these terms is quantified before being combined in quadrature to give the uncertainty estimate of the a posteriori. Additional biases may arise due to the filters applied to satellite data and model output, and where possible these are assessed.

The final determination of top-down emissions comes from Equation 3.8, repeated here:

$$E_{OMI} = \frac{\Omega_{OMI} - \Omega_{OMI,0}}{S}$$

Assuming each term is independent, the following quadrature rules are used we use the following quadrature rules^{mh} to estimate random error in E_{OMI} :

$$z = x + y : \Delta z = \sqrt{(\Delta x)^2 + (\Delta y)^2} \quad (3.10)$$

$$z = x/y : \Delta z = z \sqrt{\left(\frac{\Delta x}{x}\right)^2 + \left(\frac{\Delta y}{y}\right)^2} \quad (3.11)$$

Which leads to the uncertainty estimation for $\text{theour}^{\text{mh}}$ a posteriori emissions as follows

$$\Phi \equiv \Omega_{OMI} - \Omega_{OMI,0}$$

$$\Delta\Phi = \sqrt{(\Delta\Omega_{OMI})^2 + (\Delta\Omega_{OMI,0})^2} \quad (3.12)$$

$$\Delta E_{OMI} = E_{OMI} \times \sqrt{\left(\frac{\Delta\Phi}{\Phi}\right)^2 + \left(\frac{\Delta S}{S}\right)^2} \quad (3.13)$$

ΔE_{OMI} is calculated using the uncertainty in underlying terms: ΔS , $\Delta\Omega_{OMI}$, and $\Delta\Omega_{OMI,0}$. For ΔS ($\Omega_{GC} = S \times E_{GC} + \Omega_{OMI,0}$ from equation 3.7), the variance in the monthly linear regression of modelled isoprene emissions and column HCHO is used—I use variance in the monthly linear regression of modelled isoprene emissions and column HCHO^{mh}, shown in Section 3.4.2. For $\Delta\Omega_{OMI}$ and $\Delta\Omega_{OMI,0}$, uncertainty comes from instrument fitting uncertainty, modelled AMF uncertainty, and uncertainty in the background correction terms, which are described and calculated in Section 3.4.3.

Figure 3.25 shows relative uncertainty over each region of Australia in monthly bins. Uncertainty in the southern regions increases between May and July due to increased error in the satellite measurements. Northern regions are impacted less by the seasonal satellite error, which generally is 10 – 20 % lower than the error from S . Figure 3.26 shows the spatial distribution of relative uncertainty in the a posteriori in summer and winter. Here the effects of satellite uncertainty at higher latitudes (especially in winter) can be seen through the increase in uncertainty with increasing latitude.

3.4.2 Model Uncertainty

E_{OMI} depends partly on the product it is trying to improve, as modelled yield is based on GEOS-Chem run with MEGAN emissions. The uncertainty in the reduced major axis regression slope between model HCHO (Ω_{GC}) and emissions (E_{GC}) is used to estimate ΔS in Equation 3.13. THere I use the ratio of t^{mh}he upper bound of the 95% confidence interval of the regression slope (CI_{UB}) is used^{mh} to represent the relative uncertainty.

$$\frac{\Delta S}{S} = \frac{CI_{UB}}{S} - 1 \quad (3.14)$$

For example, if the interval upper bound is 30% higher than the slope, relative uncertainty is set to 0.3 (or 30%). The confidence interval for each month is based on the covariance matrix between Ω_{GC} and E_{GC} , and the critical t-statistic considering n to be the number of days in the month (the significance value of the test is set to 0.025).

This is a simple method of approximating the uncertainty of this term, only accounting for monthly uncertainty of the slope calculation. It does not take into account uncertainty in the underlying model, nor representation uncertainties arising from temporal or spatial resolution, which are difficult to quantify. Figure 3.27 shows the relative uncertainty in S over Australia and for each region. There is little discernible seasonality to the relative error in S , which generally ranges from 0.3 – 0.4 (30 – 40%). For comparison, Palmer et al. (2006) found $\frac{\Delta S}{S}$ to be 30% over the US after comparing with another chemical transport model and in situ measurements. To

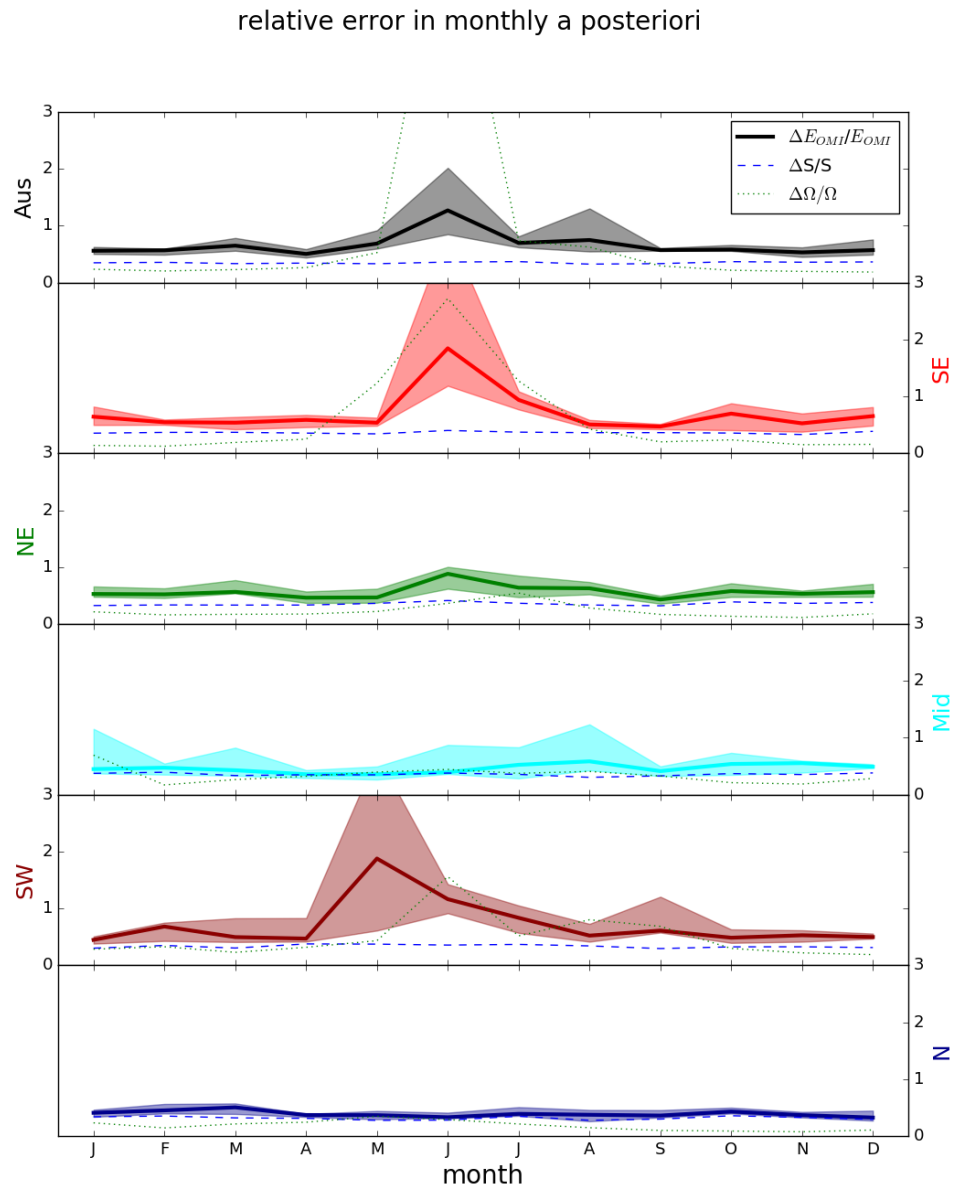


FIGURE 3.25: Median and inter-quartile range of multi-year monthly relative uncertainty in the a posteriori. Median relative uncertainty in S and Ω are added as dashed and dotted lines respectively.

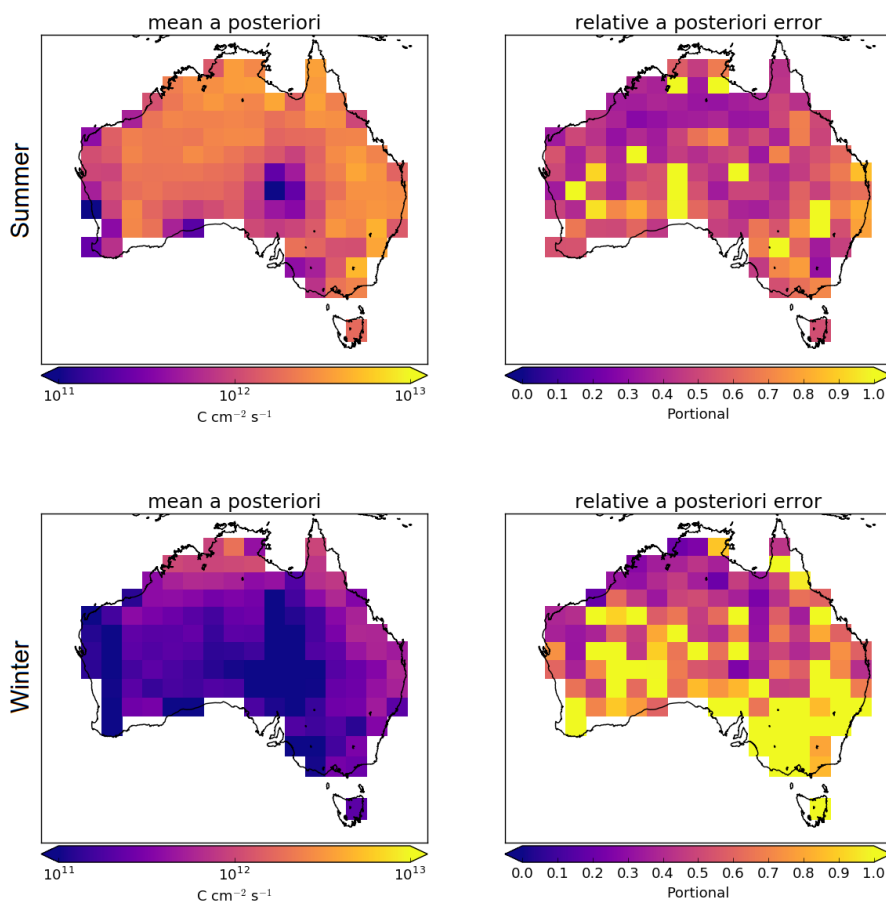


FIGURE 3.26: Summer (DJF, top row) and winter (JJA, bottom row) a posteriori emissions (left column) and relative error (right column).

improve understanding of uncertainty in S would require further analysis of GEOS-Chem yield over Australia, including how it responds to environmental and meteorological parameters, and how representative this modelled quantity is when compared to measurements. Slope estimation may also be affected by non-isoprene biogenic VOC emissions such as monoterpenes, which are not analysed in this work. The effects of these biogenics will be in part seen by ΔS (as they make up some of the variability); however this is an important source of HCHO that will need to be attributed in future work to improve confidence in the estimation of S .

Filtering for spatial smearing (see Section 3.2.5.1) reduces the number of data points making up the regression slope S . The process generally improves the linear relationship between isoprene emission and HCHO total column, which suggests it is working as intended to remove days when local biogenic emissions are not driving HCHO enhancement. Where S regressions have a correlation coefficient (r) of less than 0.4, a multi-year average (or in the worst cases no value at all) is used in lieu of monthly S data. The thresholds for the smearing filter are based on literature values from other countries, which may prove to be unsuitable within Australia. To improve the understanding of smearing in Australia, a better approximation of HCHO lifetimes and yields, as well as NO_x seasonality and regional concentrations, is required. The filtering process is accounted for in the calculation of ΔS , and the effect is a small reduction of the overall uncertainty from S .

Model biases are not analysed in this thesis, except to note that they would impact both preliminary OMI calculations (via use in calculating the air mass factor) and the modelled slope. Insufficient independent measurements in Australia make it impossible to quantify uncertainty at a national scale.

3.4.3 Satellite Uncertainty

Corrected vertical columns of HCHO from the OMI product are calculated using Equation 2.23: $\Omega = \frac{SC - RSC}{AMF}$. Error in satellite HCHO columns is determined by error in the three terms SC , RSC , and AMF :

Fitting error from the OMI retrieval

Fitting error represents the uncertainty in the DOAS technique used to estimate HCHO concentrations. Fitting error is provided in the OMHCHO product. This error is ascribed to the SC term.

Provided with the OMI product is the measurement of uncertainty in each pixel, calculated by the Smithsonian Astrophysical Observatory from the back scattered solar radiation fit (Gonzalez Abad et al. 2015; Abad et al. 2016). This is used as the ΔSC in Equation 3.15. The relative fitting error per pixel ($\frac{\Delta SC}{SC}$) ranges from around 20% to 150%, and is higher where low amounts of HCHO are detected, and at higher solar zenith angles (i.e. at high latitudes).

Uncertainty in AMF calculations

Air mass factors model vertical sensitivity to slant path measurements in the satellite instrument, and uncertainties arise predominantly from uncertain cloud parameters (Palmer et al. 2006). Vertical columns from OMI are recalculated using AMFs derived from GEOS-Chem (Section 2.6.3). AMF uncertainty can be

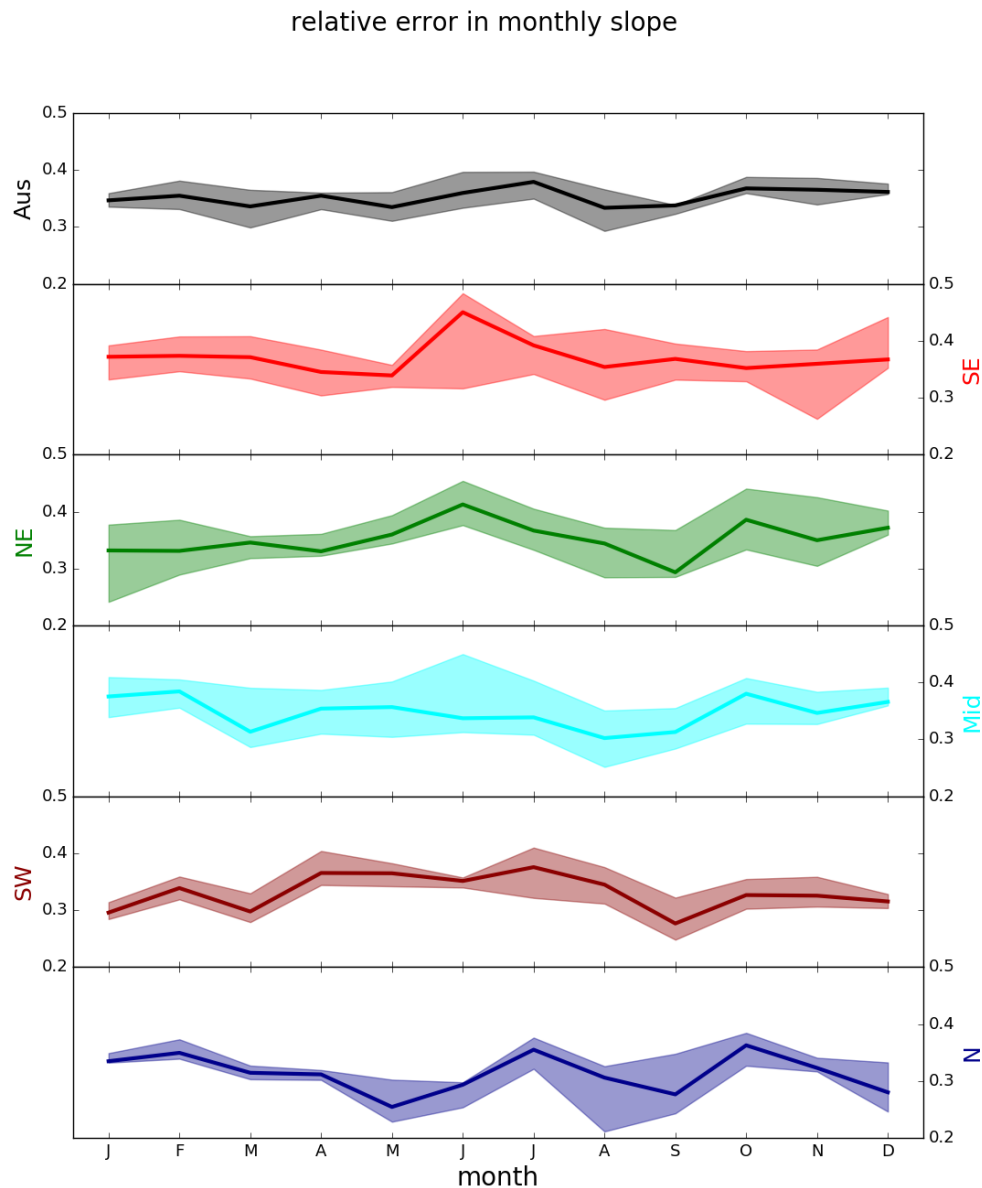


FIGURE 3.27: Median and inter-quartile range of monthly binned uncertainty in S .

determined through comparison of GEOS-Chem output to independently measured HCHO columns. In this work the AMF error is set to 30%, which approximates that seen by Palmer et al. (2006), since measurements over Australia are lacking. For comparison, Wollongong FTIR measurements are over-predicted by GEOS-Chem modelled vertical columns by $\sim 15 - 20\%$, but these are not representative at the continental scale simulated here. The assumed error of 30% is ascribed to the *AMF* term.

Palmer et al. (2006) calculated the error in AMF through combining estimates of error in the UV albedo database ($\sim 8\%$), model error based on in situ measurements, cloud error (20 – 30% (Martin 2003)), and aerosol errors ($< 20\%$), totalling AMF error of around $\sim 30\%$ (calculated in quadrature). This error estimate can be compared with that of Curci et al. (2010), where the error in AMF calculations and background columns were respectively found to be 30% and 15%. Millet et al. (2008) also examined this uncertainty and determine an overall uncertainty (1σ) of 25 – 27% in HCHO vertical columns with calculated AMFs where cloud fraction < 0.2 .

Uncertainty of HCHO background

OMI vertical columns are corrected using background (or reference sector) measurements. This is to account for instrument degradation, and adds some uncertainty to the column. In this work vertical columns are corrected using reference sector measurements combined with modelled HCHO, which is described in Chapter 2 (Section 2.6.5). Error from background uncertainty is ascribed to the *RSC* term.

The *RSC*, or background correction, is based on differences in the remote Pacific between daily HCHO slant columns measured by OMI and monthly averages from GEOS-Chem. The correction for each pixel is determined per latitude and OMI track; however, a couple of conservative simplifications are used here to estimate the error in this term. For each SC, the *RSC* is set to the mean correction matching the *SC* latitude over all tracks. For each day, the ΔRSC is set to the standard deviation of the *RSC* over Australian latitudes (45°S to 10°S) in all tracks. Background error calculated in this way is on the order of 5%-10% after monthly averaging, however this error increases in the higher southern latitudes during autumn and winter to $\sim 15\%$. For comparison, the background error is assumed to be 15% in Curci et al. (2010) following (Dufour et al. 2008).

Calculation of uncertainty in the OMI vertical column HCHO ($\Omega = \frac{SC-RSC}{AMF}$) is performed using quadrature equations 3.10 and 3.11. Error in the slant column

(ΔSC) is combined with assumed relative AMF error ($\frac{\Delta AMF}{AMF}$) of 30%, and background error to calculate $\Delta\Omega_{OMI}$ (and $\Delta\Omega_{OMI,0}$) as follows:

$$\begin{aligned}\Delta(SC - RSC) &= \sqrt{(\Delta SC)^2 + (\Delta RSC)^2} \\ \Delta\Omega &= \Omega \sqrt{\left(\frac{\Delta(SC - RSC)}{(SC - RSC)}\right)^2 + \left(\frac{\Delta AMF}{AMF}\right)^2} \\ \frac{\Delta\Omega}{\Omega} &= \sqrt{\frac{(\Delta SC)^2 + (\Delta RSC)^2}{(SC - RSC)^2} + \left(\frac{\Delta AMF}{AMF}\right)^2} \quad (3.15)\end{aligned}$$

The RSC term is described in Chapter 2 Section 2.6.6. Negative columns can occur where column amounts are lower than RSC , and these are not removed so as not to introduce a bias. When monthly averages are less than zero, relative error is set to 100%. This only impacts the uncertainty calculations in winter for the non-northern regions, where occasional highly negative absolute uncertainty was seen when Ω approached 0.

These sources of error can be reduced through spatial and temporal averaging, as they are assumed to be unbiased. Uncertainty is reduced by the square root of the number of pixels averaged over each $2^\circ \times 2.5^\circ$ grid square for each day or month. For example, daily averaging reduces pixel uncertainty by a factor of 2-4. Figure 3.28 shows the pixel counts in each region before and after applying filters. Winter has lower pixel count for southern regions, with approximately 50-60% fewer good pixels through May, June, and July. The lowest pixel counts occur in the southeast in winter, likely due to a mix of relatively high solar zenith angles and filtering of anthropogenic emissions. Northern regions have lower pixel counts in the summer, most likely due to increased cloud coverage which limits satellite measurement capabilities as discussed previously.

Figure 3.29 shows the relative uncertainty in monthly satellite columns for each sub-region and averaged over Australia. Uncertainty in winter at higher latitudes is greatly increased due to lower pixel counts, lower absolute column amounts, and higher fitting error.

Uncertainty in satellite HCHO ($\Delta\Omega$) from literature and calculated here is listed in Table 3.6. De Smedt et al. (2012) found satellite HCHO uncertainty to be 30 – 40% for the GOME-2 instrument by combining slant column systematic and random errors. For mid latitude winters they found an excess of 60% uncertainty. OMI measurements will have similar uncertainty; however, the array of detectors provide more pixels which can be averaged to reduce this uncertainty.

In order to calculate the bias or systematic error, an understanding of biases in the underlying terms is required, since there is little in the way of comparable measurements. OMI has been shown to underestimate observed HCHO by up to $\sim 40\%$ elsewhere in the world. For example OMI underestimated aircraft measurements by 37% in Guyana (Barkley et al. 2013). OMI underestimates range from 20-37% when compared against aircraft data over the southeast United States (Zhu et al. 2016). OMI validation against 7 sites (the most southern site being Reunion Island at 20.9°S) using MAX-DOAS and FTIR retrievals showed up to 50% underestimates by satellite HCHO retrievals (De Smedt et al. 2015). The highest underestimate occurred during

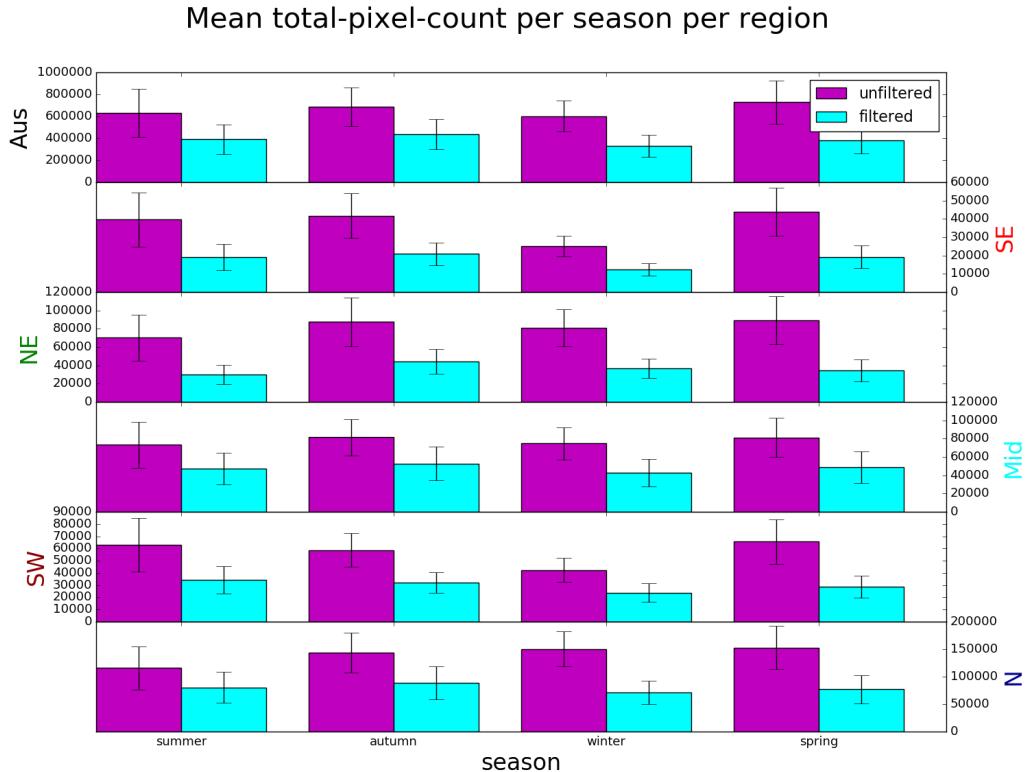


FIGURE 3.28: Mean and standard deviation (vertical error bars) of total pixel counts per region per season, before (magenta) and after (cyan) applying smearing, pyrogenic, and anthropogenic filters.

TABLE 3.6: Uncertainties in satellite total column HCHO.

uncertainty	location	notes
40%	North America	GOME, mostly due to cloud interference ^a
26%	North America	GOME, OMI, with cloud fraction less than 20% ^b
30%-40%	global	GOME-2 ^c
> 60%	Mid-latitude	GOME-2 in winters ^c
1%-10%	Australia	OMI, monthly uncertainty at $2^\circ \times 2.5^\circ$ ^d
50%-100+%	Australia	OMI, in winter at higher latitudes ^d

a: Millet et al. (2006) and Palmer et al. (2006)

b: Millet et al. (2008)

c: De Smedt et al. (2008) and De Smedt et al. (2012)

d: This work

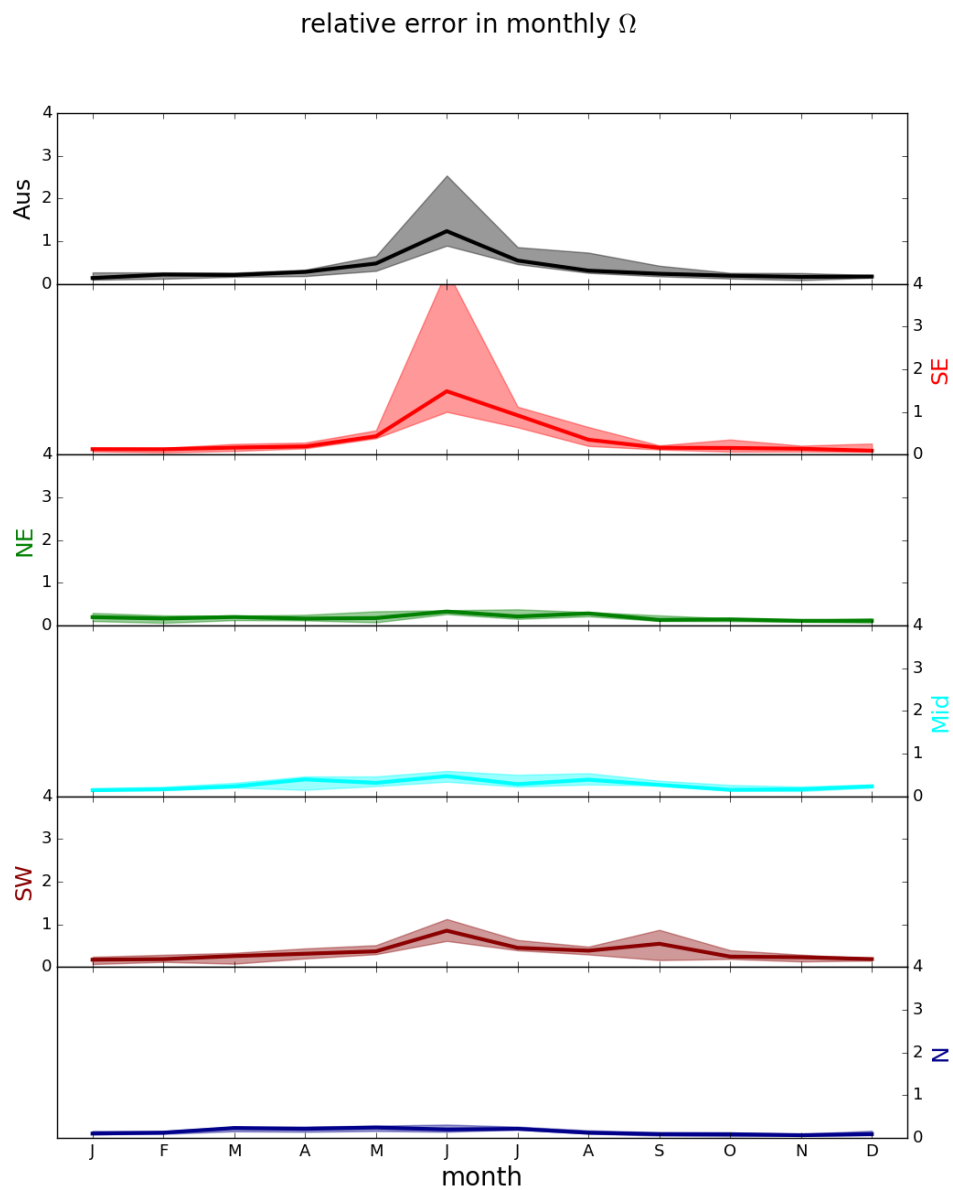


FIGURE 3.29: Median and inter-quartile range for monthly binned relative uncertainty in satellite vertical columns.

periods of high concentration (Vigouroux et al. 2009; De Smedt et al. 2015). Satellite HCHO may also suffer from $\sim 13\%$ overestimation when taking monthly averages due to only measuring on relatively cloud-free days (Surl, Palmer, and Abad 2018). In this thesis, the a posteriori is linearly related to the satellite HCHO and any bias is directly transferred. The conclusion drawn here is that the isoprene emissions product in this work may be affected by satellite HCHO underestimation of up to 40%, and also by monthly HCHO overestimation of 13%, which gives a potential bias of 1/0.6 to 1/1.13. This may be complicated further if the satellite bias over Australia does not match the bias over the remote Pacific at corresponding latitudes. However, bias over Australia cannot be quantified due to insufficient measurements. GEOS-Chem biases would affect the recalculation of HCHO, but they cannot be quantified and so are not included in this thesis. Lacking suitable measurements to estimate satellite bias over Australia, the potential bias range compiled from the literature (-13% to $+40\%$) is applied to the mean emissions in each month when calculating the uncertainty range shown in the results (see Figure 3.9).

3.4.4 Sensitivity to AMF recalculation

This section examines the sensitivity of the top-down isoprene emission estimates (E_{OMI}) to the AMF recalculation method. The a posteriori emissions change linearly with recalculated vertical columns, which are calculated in three different ways: using the AMF provided in the OMHCHO product (AMF_{OMI}), recalculating AMF shape factors but keeping the original scattering weights (AMF_{GC}), or recalculating both shape factors and scattering weights (AMF_{PP}), as described in Section 2.5.

Figure 3.30 shows AMFs and emissions recalculated using each of these three methods over 2005. This figure only depicts grid squares with non-zero emissions, since in this work the regions of interest are those where emissions are relatively more substantial within Australia. The fully recalculated AMF_{PP} is higher in summer, but lower in other seasons compared against the other recalculations. The direct effect of a lower AMF is an increased vertical column, which should lead to higher emission estimates, and vice versa. This can be seen in all seasons except for summer, although even here the emissions estimates based on AMF_{PP} are higher than if they are calculated using the original AMF_{OMI} . Emission estimates vary widely over Australia, but the sensitivity to AMF recalculation technique is proportional and potentially non-linear. Changes in AMF of 5 – 30% cause changes in emission estimates of 5 – 50%. Further analysis is warranted and should be a focus of future work.

3.4.5 Sensitivity to filtering

Figure 3.31 shows emissions estimates with and without filtering for smearing, anthropogenic, and pyrogenic influences. The overall effect of filtering is to slightly raise emissions in all non-summer months, with relatively little change to the mean in winter months. This is true in all regions except for northern Australia, which shows a slight decrease in spring. Eastern regions are most frequently filtered, with more than 50% of the available good pixels filtered throughout the year, while other regions vary between 20% and 60% with lower filtering rates in summer months.

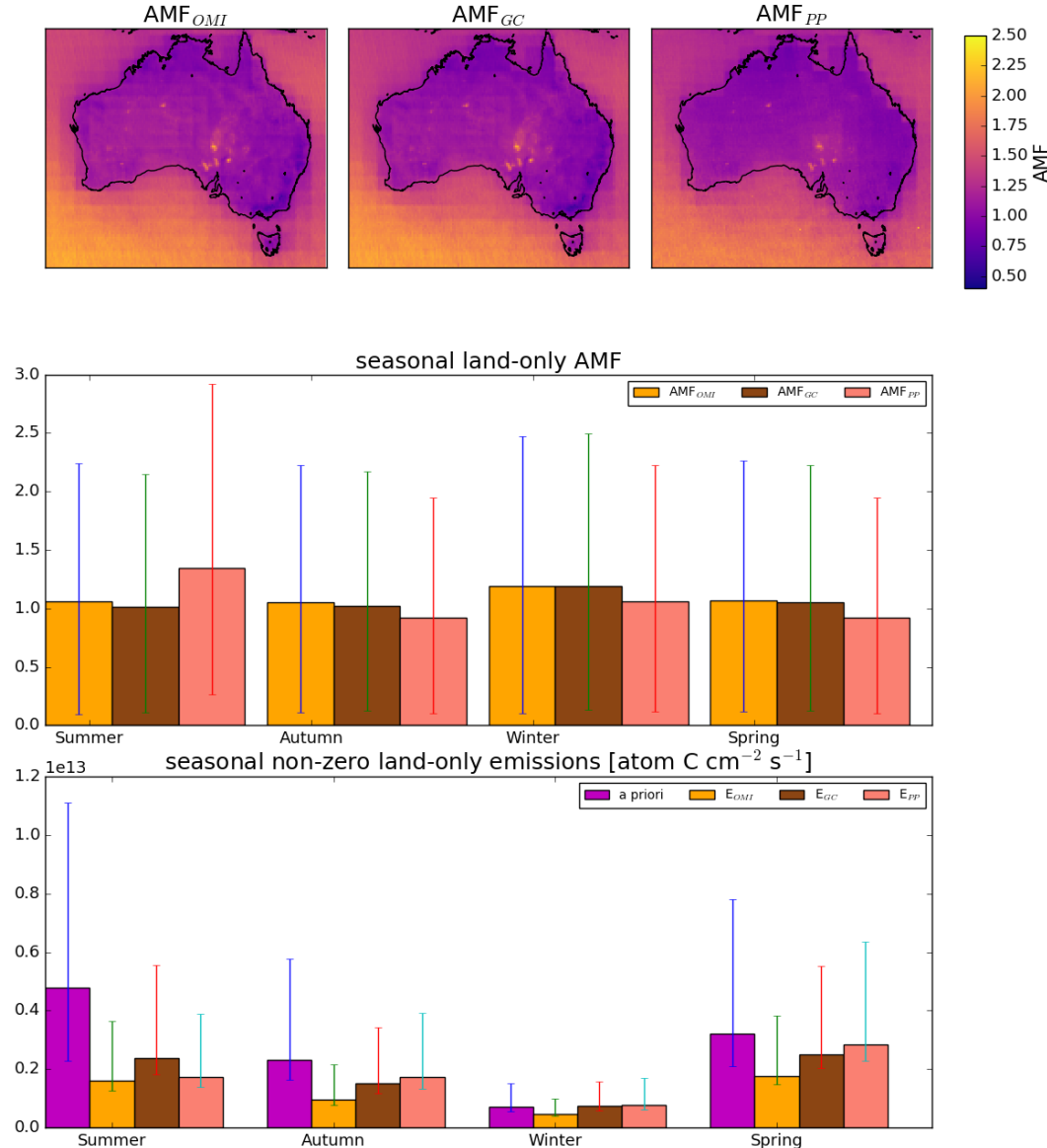


FIGURE 3.30: Top row: averaged OMI Satellite AMF for 2005, from the OMHCCHO dataset (left, AMF_{OMI}), recalculated using GEOS-Chem shape factors (middle, AMF_{GC}), and recalculated using GEOS-Chem shape factors and scattering weights (right, AMF_{PP}). Middle row: mean and inter-quartile range of each AMF over 2005 for each season. Bottom row: mean and inter-quartile range of non-zero a priori emissions based on the three AMFs (with matching subscripts) along with the a priori emissions from GEOS-Chem.

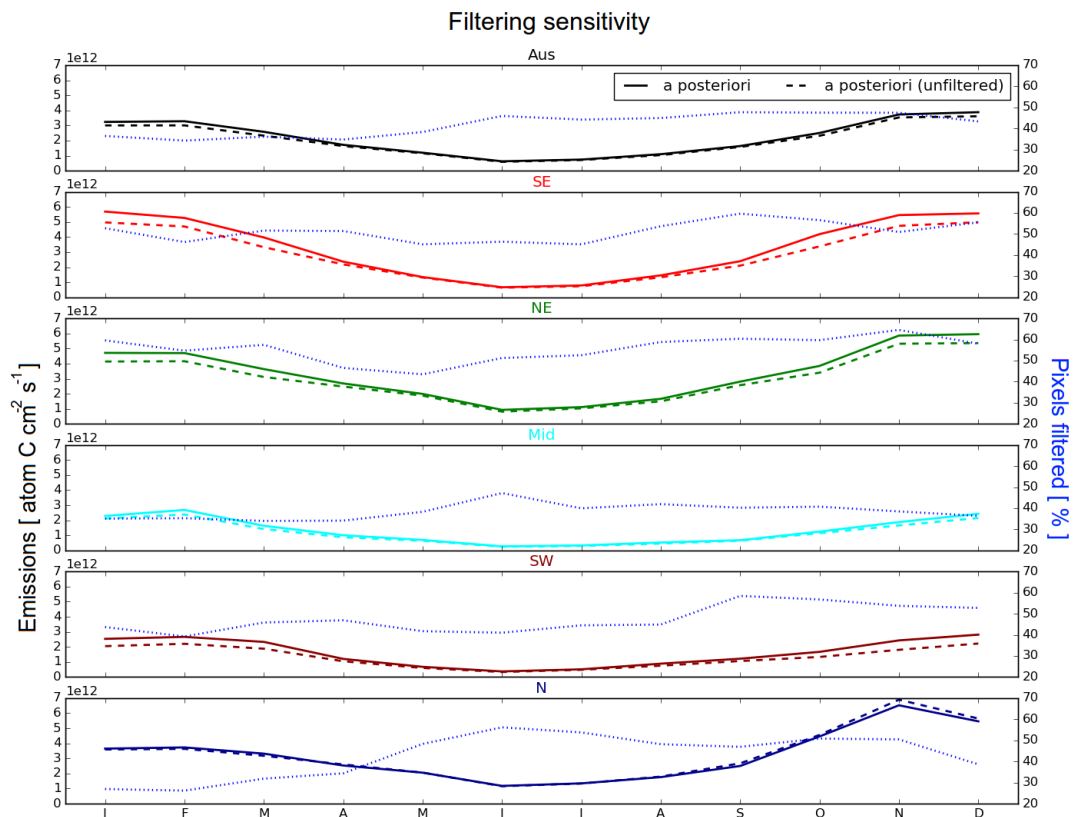


FIGURE 3.31: Multi-year monthly mean values for a posteriori emission estimates calculated with (solid) and without (dashed) applying filters for anthropogenic, pyrogenic, and smearing influences. The portion of pixels within each region which are filtered is shown on the right axis with a blue dotted line.

3.5 Conclusions and implications

Very few ground-based measurements of BVOC concentrations are available in Australia. Emission models use largely unverified extrapolations for emission factors and parameterisations in Australia, leading to overestimated isoprene emissions (Emmerson et al. 2016). This leads to uncertainty and error when modelling atmospheric ozone and other trace gases.

In this chapter, I created and tested^{mh} an isoprene emissions estimate (a posteriori) is created and tested^{mh} based on OMI satellite measurements of HCHO, a high-yield product of isoprene oxidation. The a posteriori emissions' effects on ozone and HCHO were tested by running GEOS-Chem with a seasonal (multi-year monthly averaged) gridded ($2^\circ \times 2.5^\circ$) scaling factor calculated from the a posteriori applied to the a priori emissions. Uncertainty in the primary components of the top-down emissions calculation were calculated where possible and potential biases identified.

The a posteriori isoprene emission estimate showed that GEOS-Chem coupled with the MEGAN emissions model overestimates emissions in summer by a factor of 2-5. Total yearly Australian emissions are reduced from 39 Tg yr^{-1} to 21 Tg yr^{-1} (decrease of $\sim 46\%$) in the a posteriori. The overestimate is spatially and temporally diverse and leads to model biases in HCHO, and ozone. Running GEOS-Chem using scaled emissions based on OMI HCHO columns reduced the model HCHO overestimate (when compared to OMI HCHO) in summer by half, from $\sim 100\%$ down to $\sim 50\%$, with most of the difference occurring outside the northern region. Model vertical column HCHO variance is somewhat ($\sim 10\% - 50\%$) lower than that seen by the OMI satellite, and this difference increased after scaling isoprene emissions. Scaling GEOS-Chem emissions also lowered simulated surface ozone concentrations by $\sim 5\%$. A posteriori uncertainty was shown to be on the order of 50% (monthly, per grid square), with large satellite-based uncertainty in winter and a potential bias coming from satellite data of -13% to $+40\%$. The primary uncertainty in the a posteriori emissions comes from the monthly modelled isoprene-to-HCHO yield ($\sim 30\% - 50\%$ uncertainty), although at higher latitudes in winter the satellite uncertainty becomes restrictively high ($> 100\%$).

The reason for the a priori overestimate remains unclear, and both global and Australian emissions estimates for isoprene range widely. The bias is in part due to the MEGAN emission model's parameterisation of how isoprene responds to parameters such as leaf area index, plant specific emission factors, and meteorological factors. In Australia, a mixture of poorly defined emission factors (e.g., Emmerson et al. 2016), unaccounted for soil moisture forcing (e.g., Sindelarova et al. 2014; Emmerson et al. 2019) and poorly understood forest responses to meteorological stresses likely drive uncertainty and model biases (Jiang et al. 2018; Emmerson et al. 2019). A potential improvement to the MEGAN soil parameterisation has been described (Jiang et al. 2018); however, a detailed map of soil properties is not currently available in Australia, and this would be required to apply the parameterisation here. An alternative parameterisation of soil moisture and drought effects on isoprene emissions was recently implemented in a different CTM by Emmerson et al. (2019) and applying this parameterisation in GEOS-Chem should be a priority for future work in Australia.

In the US, bias between OMI and in situ measurements is as high as 40%, but bias

across Australia cannot be determined as there are not enough independent observations. This leads to a wide uncertainty range for estimated top-down emissions (see Figure 3.9) and limits potential top-down refinements to isoprene emissions. Ground-based and aircraft VOC, NO_x, HCHO, and ozone measurements over large areas at relatively fine temporal resolution would help quantify the currently unknown satellite biases while additionally providing constraints for bottom-up models. In the northern region in particular, emissions are affected by monsoonal forcing, but increased cloud coverage during the monsoon limits satellite coverage. This makes characterisation of forest emissions and their response to sunlight, temperature, and moisture even more important in these areas. In addition to measurements, further analysis determining the sensitivity of modelled emissions to model resolution and changing soil moisture parameters (and parameterisations) would provide the foundation to improve GEOS-Chem and MEGAN modelled isoprene emissions along with oxidation products like HCHO and ozone.

In the future, other satellites (e.g., GOME-2, TROPOMI) could be used to improve emission estimates further, with differing overpass times potentially allowing a measure of diurnal emission patterns. Additionally, an adjoint version of GEOS-Chem over Australia could provide improved estimates of isoprene emission taking into account transport. An adjoint based inversion could also provide an evaluation of how resolution-limited the linear top-down emission estimates are over Australia. The emission estimate created in this chapter could also be refined to higher temporal resolution, with further analysis of uncertainty. Oversampling techniques could be applied near populated areas in order to improve the understanding of isoprene, HCHO, and ozone relationships over cities (e.g., Surl, Palmer, and Abad 2018). Furthermore, linking the top-down isoprene emissions to the underlying emission factors for Australia and implementing the changes in GEOS-Chem would improve the understanding of the natural atmosphere over this relatively remote portion of the planet.

Bibliography

- Abad, Gonzalo González et al. (2016). "Smithsonian Astrophysical Observatory Ozone Mapping and Profiler Suite (SAO OMPS) formaldehyde retrieval". In: *Atmospheric Measurement Techniques* 9.7, pp. 2797–2812. ISSN: 18678548. DOI: 10.5194/amt-9-2797-2016.
- Abbot, Dorian S. (2003). "Seasonal and interannual variability of North American isoprene emissions as determined by formaldehyde column measurements from space". In: *Geophysical Research Letters* 30.17, pp. 1999–2002. ISSN: 0094-8276. DOI: 10.1029/2003GL017336. URL: <http://doi.wiley.com/10.1029/2003GL017336>.
- Ahn, Changwoo, Omar Torres, and Pawan K. Bhartia (2008). "Comparison of Ozone Monitoring Instrument UV Aerosol Products with Aqua/Moderate Resolution Imaging Spectroradiometer and Multiangle Imaging Spectroradiometer observations in 2006". In: *Journal of Geophysical Research Atmospheres* 113.16, pp. 1–13. ISSN: 01480227. DOI: 10.1029/2007JD008832.
- Akritidis, Dimitris et al. (2016). "On the role of tropopause folds in summertime tropospheric ozone over the eastern Mediterranean and the Middle East". In: *Atmospheric Chemistry and Physics* 16.21, pp. 14025–14039. DOI: 10.5194/acp-16-14025-2016. URL: <http://www.atmos-chem-phys.net/16/14025/2016/>.
- Alexander, S. P. et al. (2013). "High resolution VHF radar measurements of tropopause structure and variability at Davis, Antarctica (69 S, 78 E)". In: *Atmospheric Chemistry and Physics* 13.6, pp. 3121–3132. ISSN: 16807324. DOI: 10.5194/acp-13-3121-2013. URL: <http://www.atmos-chem-phys.net/13/3121/2013/>.
- Arneth, A et al. (2008). "Why are estimates of global terrestrial isoprene emissions so similar (and why is this not so for monoterpenes)?" In: *Atmos. Chem. Phys* 8.x, pp. 4605–4620. ISSN: 1680-7375. DOI: 10.5194/acpd-8-7017-2008.
- Arneth, Almut et al. (2007). "CO₂ inhibition of global terrestrial isoprene emissions: Potential implications for atmospheric chemistry". In: *Geophysical Research Letters* 34.18, p. L18813. DOI: 10.1029/2007GL030615. URL: <http://doi.wiley.com/10.1029/2007GL030615>.
- Ashmore, M R, Lisa. Emberson, and Murray Frank (2003). *Air pollution impacts on crops and forests : a global assessment*. Ed. by Lisa Emberson, Mike Ashmore, and Frank Murray. Imperial College Press London ; River Edge, NJ, xiii, 372 p. : ISBN: 186094292.
- Atkinson, Roger (2000). "Atmospheric chemistry of VOCs and NO(x)". In: *Atmospheric Environment* 34.12-14, pp. 2063–2101. ISSN: 13522310. DOI: 10.1016/S1352-2310(99)00460-4.
- Atkinson, Roger and Janet Arey (2003). "Gas-phase tropospheric chemistry of biogenic volatile organic compounds: A review". In: *Atmospheric Environment* 37.SUPPL. 2. ISSN: 13522310. DOI: 10.1016/S1352-2310(03)00391-1.

- Avnery, Shiri et al. (2013). "Global crop yield reductions due to surface ozone exposure: 2. Year 2030 potential crop production losses and economic damage under two scenarios of O₃ pollution". In: *Atmospheric Environment* 71.13, pp. 408–409. ISSN: 13522310. DOI: 10.1016/j.atmosenv.2012.12.045. URL: <http://dx.doi.org/10.1016/j.atmosenv.2011.01.002>.
- Ayers, G. P. et al. (1997). "Formaldehyde production in clean marine air". In: *Geophysical Research Letters* 24.4. DOI: <https://doi.org/10.1029/97GL00123>.
- Ayers, James D and William R Simpson (2006). "Measurements of N₂O₅ near Fairbanks, Alaska". In: *Journal of Geophysical Research: Atmospheres* 111.D14, n/a–n/a. ISSN: 2156-2202. DOI: 10.1029/2006JD007070. URL: <http://dx.doi.org/10.1029/2006JD007070>.
- Baray, J. L. et al. (2000). "Planetary-scale tropopause folds in the southern subtropics". In: *Geophysical Research Letters* 27.3, pp. 353–356. ISSN: 00948276. DOI: 10.1029/1999GL010788.
- Baray, Jean-Luc et al. (2012). "One year ozonesonde measurements at Kerguelen Island (49.2S, 70.1E): Influence of stratosphere-to-troposphere exchange and long-range transport of biomass burning plumes". In: *Journal of Geophysical Research* 117.D6. ISSN: 2156-2202. DOI: 10.1029/2011JD016717. URL: <http://dx.doi.org/10.1029/2011JD016717>.
- Barkley, Michael P. et al. (2013). "Top-down isoprene emissions over tropical South America inferred from SCIAMACHY and OMI formaldehyde columns". In: *Journal of Geophysical Research Atmospheres* 118.12, pp. 6849–6868. ISSN: 21698996. DOI: 10.1002/jgrd.50552. URL: <http://dx.doi.org/10.1002/jgrd.50552>.
- Bauwens, M et al. (2013). "Satellite-based isoprene emission estimates (2007–2012) from the GlobEmission project". In: *Proceedings of the ACCENT-Plus Symposium, Atmospheric Composition Change-Policy Support and Science, Urbino*, pp. 17–20.
- Bauwens, Maite et al. (2016). "Nine years of global hydrocarbon emissions based on source inversion of OMI formaldehyde observations". In: *Atmospheric Chemistry and Physics* March, pp. 1–45. ISSN: 1680-7375. DOI: 10.5194/acp-2016-221. URL: <http://www.atmos-chem-phys-discuss.net/acp-2016-221/>.
- Beekmann, M. et al. (1997). "Regional and global tropopause fold occurrence and related ozone flux across the tropopause". In: *Journal of Atmospheric Chemistry* 28.1–3, pp. 29–44. ISSN: 01677764. DOI: 10.1023/A:1005897314623.
- Bethan, S., G. Vaughan, and S. J. Reid (1996). "A comparison of ozone and thermal tropopause heights and the impact of tropopause definition on quantifying the ozone content of the troposphere". In: *Quarterly Journal of the Royal Meteorological Society* 122.532, pp. 929–944. ISSN: 00359009. DOI: 10.1002/qj.49712253207. URL: <http://doi.wiley.com/10.1002/qj.49712253207>.
- Bey, Isabelle et al. (2001). "Global Modeling of Tropospheric Chemistry with Assimilated Meteorology: Model Description and Evaluation". In: *Journal of Geophysical Research* 106, pp. 73–95. ISSN: 0148-0227. DOI: 10.1029/2001JD000807.
- Brasseur, Guy P and Daniel J Jacob (2017). *Modeling of Atmospheric Chemistry*. Cambridge University Press. DOI: 10.1017/9781316544754.

- Brinksma, E. J. et al. (2002). "Five years of observations of ozone profiles over Lauder , New Zealand". In: *Journal of Geophysical Research* 107.D14, pp. 1–11. ISSN: 0148-0227. DOI: 10 . 1029 / 2001JD000737. URL: <http://doi.wiley.com/10.1029/2001JD000737>.
- Brown, S. S. et al. (2009). "Nocturnal isoprene oxidation over the Northeast United States in summer and its impact on reactive nitrogen partitioning and secondary organic aerosol". In: *Atmospheric Chemistry and Physics* 9.9, pp. 3027–3042. ISSN: 16807316. DOI: 10.5194/acp-9-3027-2009.
- Cape, J. N. (2008). "Surface ozone concentrations and ecosystem health: Past trends and a guide to future projections". In: *Science of the Total Environment* 400.1-3, pp. 257–269. ISSN: 00489697. DOI: 10.1016/j.scitotenv.2008.06.025. URL: <http://dx.doi.org/10.1016/j.scitotenv.2008.06.025>.
- Carlisle, Wendy (2012). *The coal seam gas rush*. URL: <http://www.abc.net.au/news/2011-11-24/coal-seam-gas-by-the-numbers-map/3664318>.
- Chance, K. (2002). "OMI Algorithm Theoretical Basis Document". In: I.August, pp. 1–50. URL: https://docserver.gesdisc.eosdis.nasa.gov/repository/Mission/OMI/3.3{_}ScienceDataProductDocumentation/3.3.4{_}ProductGenerationAlgorithm/ATBD-OMI-04.pdf.
- Chance, K. et al. (2000). "Satellite observations of formaldehyde over North America from GOME". In: *Geophysical Research Letters* 27.21, pp. 3461–3464. ISSN: 00948276. DOI: 10.1029/2000GL011857. URL: <http://dx.doi.org/10.1029/2000gl011857>.
- Chen, D. et al. (2009). "Regional CO pollution in China simulated by the high-resolution nested-grid GEOS-Chem model". In: *Atmospheric Chemistry and Physics Discussions* 9.2, pp. 5853–5887. ISSN: 1680-7324. DOI: 10.5194/acpd-9-5853-2009. URL: <http://dx.doi.org/10.5194/acp-9-3825-2009>.
- Cheng, M et al. (2016). "Factors controlling volatile organic compounds in dwellings in Melbourne, Australia". In: *Indoor Air* 26.2, pp. 219–230. DOI: 10.1111/ina.12201. URL: <https://onlinelibrary.wiley.com/doi/abs/10.1111/ina.12201>.
- Christian, Kenneth E, William H Brune, and Jingqiu Mao (2017). "Global sensitivity analysis of the GEOS-Chem chemical transport model: ozone and hydrogen oxides during ARCTAS (2008)". In: *Atmos. Chem. Phys* 17, pp. 3769–3784. DOI: 10.5194/acp-17-3769-2017. URL: www.atmos-chem-phys.net/17/3769/2017/.
- Christian, Kenneth E. et al. (2018). "Global sensitivity analysis of GEOS-Chem modeled ozone and hydrogen oxides during the INTEX campaigns". In: *Atmospheric Chemistry and Physics* 18.4, pp. 2443–2460. ISSN: 1680-7324. DOI: 10.5194/acp-18-2443-2018. URL: <https://www.atmos-chem-phys.net/18/2443/2018/>.
- Cooper, O. et al. (2004). "On the life cycle of a stratospheric intrusion and its dispersion into polluted warm conveyor belts". In: *Journal of Geophysical Research* 109.23, pp. 1–18. ISSN: 01480227. DOI: 10.1029/2003JD004006.
- Cooper, O R, S Gilge, and D T Shindell (2014). "Global distribution and trends of tropospheric ozone : An observation-based review". In: pp. 1–28. DOI: 10.12952/journal.elementa.000029. URL: <https://www.elementascience.org/articles/10.12952/journal.elementa.000029/>.
- Cope, M. E. et al. (2004). "The Australian Air Quality Forecasting System. Part I: Project Description and Early Outcomes". In: *American Meteorological Society*. DOI:

- 10.1175/2093.1. URL: <https://journals.ametsoc.org/doi/full/10.1175/2093.1>.
- Crounse, John D. et al. (2006). "Measurement of gas-phase hydroperoxides by chemical ionization mass spectrometry". In: *Analytical Chemistry* 78.19, pp. 6726–6732. ISSN: 00032700. DOI: 10.1021/ac0604235. URL: <https://pubs.acs.org/doi/abs/10.1021/ac0604235>.
- Crounse, John D et al. (2011). "Peroxy radical isomerization in the oxidation of isoprene". In: *Physical Chemistry Chemical Physics* 13.30, pp. 13607–13613. ISSN: 1463-9076. DOI: doi:10.1039/c1cp21330j. URL: <http://dx.doi.org/10.1039/C1CP21330J>.
- Crounse, John D et al. (2012). "Atmospheric Fate of Methacrolein. 1. Peroxy Radical Isomerization Following Addition of OH and O₂". In: *Physical Chemistry m.*
- Crounse, John D. et al. (2013). "Autoxidation of organic compounds in the atmosphere". In: *Journal of Physical Chemistry Letters* 4.20, pp. 3513–3520. ISSN: 19487185. DOI: 10.1021/jz4019207. URL: <http://pubs.acs.org/doi/abs/10.1021/jz4019207>.
- Crutzen, Paul J, Mark G Lawrence, and Ulrich Poschl (1999). "On the background photochemistry of tropospheric ozone". In: *Tellus A* 51.1, pp. 123–146. ISSN: 1600-0870. DOI: 10.1034/j.1600-0870.1999.t01-1-00010.x. URL: <http://dx.doi.org/10.1034/j.1600-0870.1999.t01-1-00010.x>.
- Curci, G. et al. (2010). "Estimating European volatile organic compound emissions using satellite observations of formaldehyde from the Ozone Monitoring Instrument". In: *Atmospheric Chemistry and Physics* 10.23, pp. 11501–11517. ISSN: 16807316. DOI: 10.5194/acp-10-11501-2010. URL: <https://www.atmos-chem-phys.net/10/11501/2010/acp-10-11501-2010.pdf>.
- Danielsen, Edwin F. (1968). *Stratospheric-Tropospheric Exchange Based on Radioactivity, Ozone and Potential Vorticity*. DOI: 10.1175/1520-0469(1968)025<0502:STEBOR>2.0.CO;2.
- Das, Siddarth Shankar et al. (2016). "Influence of tropical cyclones on tropospheric ozone: possible implications". In: *Atmospheric Chemistry and Physics* 16, pp. 4837–4847. DOI: 10.5194/acp-16-4837-2016. URL: www.atmos-chem-phys.net/16/4837/2016/.
- Davenport, J. J. et al. (2015). "A measurement strategy for non-dispersive ultra-violet detection of formaldehyde in indoor air : spectral analysis and interferent gases". In: *Measurement Science and Technology* 015802. December 2015, p. 15802. ISSN: 0957-0233. DOI: 10.1088/0957-0233/27/1/015802. URL: <http://dx.doi.org/10.1088/0957-0233/27/1/015802>.
- De Smedt, I et al. (2008). "Twelve years of global observations of formaldehyde in the troposphere using GOME and SCIAMACHY sensors". In: *Atmospheric Chemistry and Physics* 8.16, pp. 4947–4963. ISSN: 1680-7324. DOI: 10.5194/acp-8-4947-2008. URL: <http://www.atmos-chem-phys.net/8/4947/2008/>.
- De Smedt, I. et al. (2012). "Improved retrieval of global tropospheric formaldehyde columns from GOME-2/MetOp-A addressing noise reduction and instrumental degradation issues". In: *Atmospheric Measurement Techniques* 5.11, pp. 2933–2949. ISSN: 18671381. DOI: 10.5194/amt-5-2933-2012. URL: <https://www.atmos-meas-tech.net/5/2933/2012/amt-5-2933-2012.pdf>.

- De Smedt, I. et al. (2015). "Diurnal, seasonal and long-term variations of global formaldehyde columns inferred from combined OMI and GOME-2 observations". In: *Atmospheric Chemistry and Physics* 15.21, pp. 12519–12545. ISSN: 16807324. DOI: 10.5194/acp-15-12519-2015. URL: <https://www.atmos-chem-phys.net/15/12519/2015/acp-15-12519-2015.pdf>.
- Dee, D P et al. (2011). "The ERA-Interim reanalysis: configuration and performance of the data assimilation system". In: *Quarterly Journal of the Royal Meteorological Society* 137.656, pp. 553–597. ISSN: 1477-870X. DOI: 10.1002/qj.828. URL: <http://dx.doi.org/10.1002/qj.828>.
- Deeter, M. N. (2002). *Calculation and application of MOPITT averaging kernels*. URL: https://www.acom.ucar.edu/mopitt/avg{_}krnl{_}app.pdf (visited on 09/20/2004).
- Delmas, R, D Serca, and C Jambert (1997). "Global inventory of NO_x sources". In: *Nutrient cycling in agroecosystems* 48.x, pp. 51–60. ISSN: 1385-1314. DOI: 10.1023/A:1009793806086. URL: <http://link.springer.com/article/10.1023/A:1009793806086>.
- Dufour, G. et al. (2008). "SCIAMACHY formaldehyde observations: constraint for isoprene emissions over Europe?" In: *Atmospheric Chemistry and Physics* 8.6, pp. 19273–19312. ISSN: 1680-7324. DOI: 10.5194/acpd-8-19273-2008.
- Dunne, Erin et al. (2018). "Comparison of VOC measurements made by PTR-MS, adsorbent tubes-GC-FID-MS and DNPH derivatization-HPLC during the Sydney Particle Study, 2012: A contribution to the assessment of uncertainty in routine atmospheric VOC measurements". In: *Atmospheric Measurement Techniques* 11.1, pp. 141–159. ISSN: 18678548. DOI: 10.5194/amt-11-141-2018. URL: <https://www.atmos-meas-tech.net/11/141/2018/amt-11-141-2018.pdf>.
- Eastham, Sebastian D., Debra K. Weisenstein, and Steven R H Barrett (2014). "Development and evaluation of the unified tropospheric-stratospheric chemistry extension (UCX) for the global chemistry-transport model GEOS-Chem". In: *Atmospheric Environment* 89, pp. 52–63. ISSN: 13522310. DOI: 10.1016/j.atmosenv.2014.02.001. URL: <http://dx.doi.org/10.1016/j.atmosenv.2014.02.001>.
- Edwards, D. P. (2003). "Tropospheric ozone over the tropical Atlantic: A satellite perspective". In: *Journal of Geophysical Research* 108.D8, p. 4237. ISSN: 0148-0227. DOI: 10.1029/2002JD002927. URL: <http://doi.wiley.com/10.1029/2002JD002927>.
- Edwards, D. P. et al. (2006). "Satellite-observed pollution from Southern Hemisphere biomass burning". In: *Journal of Geophysical Research* 111.14, pp. 1–17. ISSN: 01480227. DOI: 10.1029/2005JD006655.
- Elbern, H, J Hendricks, and A Ebel (1998). "A Climatology of Tropopause Folds by Global Analyses". In: *Theoretical and Applied Climatology* 59.3, pp. 181–200. ISSN: 1434-4483. DOI: 10.1007/s007040050023. URL: <http://dx.doi.org/10.1007/s007040050023>.
- Emmerson, Kathryn M. et al. (2016). "Current estimates of biogenic emissions from eucalypts uncertain for southeast Australia". In: *Atmospheric Chemistry and Physics* 16.11, pp. 6997–7011. ISSN: 1680-7324. DOI: 10.5194/acp-16-6997-2016. URL: <http://www.atmos-chem-phys.net/16/6997/2016/>.
- Emmerson, Kathryn M et al. (2019). "Sensitivity of isoprene emissions to drought over south-eastern Australia : Integrating models and satellite observations of soil moisture". In: *Atmospheric Environment* 209.April, pp. 112–124. ISSN: 1352-2310. DOI:

- 10 . 1016 / j . atmosenv . 2019 . 04 . 038. URL: <https://doi.org/10.1016/j.atmosenv.2019.04.038>.
- Eskes, HJ and K F Boersma (2003). "Averaging kernels for DOAS total-column satellite retrievals". In: *Atmospheric Chemistry and Physics* 3.1, pp. 1285–1291. ISSN: 1680-7324. DOI: 10.5194/acp-3-1285-2003. URL: <http://dx.doi.org/10.5194/acpd-3-895-2003>.
- EUMETSAT (2015). GOME2. URL: <http://www.eumetsat.int/website/home/Satellites/CurrentSatellites/Metop/MetopDesign/GOME2/index.html>.
- Fan, Jiwen and Renyi Zhang (2004). "Atmospheric oxidation mechanism of isoprene". In: *Environmental Chemistry* 1.3, pp. 140–149. ISSN: 14482517. DOI: 10.1071/EN04045. URL: <http://dx.doi.org/10.1071/en04045>.
- Fisher, Jenny A. et al. (2016). "Organic nitrate chemistry and its implications for nitrogen budgets in an isoprene- and monoterpene-rich atmosphere: Constraints from aircraft (SEAC 4 RS) and ground-based (SOAS) observations in the Southeast US". In: *Atmospheric Chemistry and Physics* 16.9, pp. 5969–5991. ISSN: 16807324. DOI: 10.5194/acp-16-5969-2016. URL: <https://www.atmos-chem-phys.net/16/5969/2016/acp-16-5969-2016.pdf>.
- Forster, P. et al. (2007). *Changes in Atmospheric Constituents and in Radiative Forcing*. In: *Climate Change 2007: The Physical Science Basis. Contribution of Working Group I to the Fourth Assessment Report of the Intergovernmental Panel on Climate Change* [Solomon, S., D. Qin, M. Man. URL: https://www.ipcc.ch/publications_and_data/ar4/wg1/en/ch2.html (visited on 01/14/2016)].
- Fortems-Cheiney, A. et al. (2012). "The formaldehyde budget as seen by a global-scale multi-constraint and multi-species inversion system". In: *Atmospheric Chemistry and Physics* 12.15, pp. 6699–6721. ISSN: 16807316. DOI: 10.5194/acp-12-6699-2012. URL: <http://www.atmos-chem-phys.net/12/6699/2012/acp-12-6699-2012.pdf>.
- Franco, B. et al. (2015). "Retrievals of formaldehyde from ground-based FTIR and MAX-DOAS observations at the Jungfraujoch station and comparisons with GEOS-Chem and IMAGES model simulations". In: *Atmospheric Measurement Techniques* 8.4, pp. 1733–1756. ISSN: 18678548. DOI: 10.5194/amt-8-1733-2015.
- Frey, W. et al. (2015). "The impact of overshooting deep convection on local transport and mixing in the tropical upper troposphere/lower stratosphere (UTLS)". In: *Atmospheric Chemistry and Physics* 15.11, pp. 6467–6486. ISSN: 1680-7324. DOI: 10.5194/acp-15-6467-2015. URL: <http://www.atmos-chem-phys.net/15/6467/2015/>.
- Fu, Tzung-may et al. (2007). "Space-based formaldehyde measurements as constraints on volatile organic compound emissions in east and south Asia and implications for ozone". In: 112, pp. 1–15. DOI: 10.1029/2006JD007853.
- Fuentes, J. D. et al. (2000). "Biogenic Hydrocarbons in the Atmospheric Boundary Layer: A Review". In: *Bulletin of the American Meteorological Society* 81.7, pp. 1537–1575. ISSN: 00030007. DOI: 10.1175/1520-0477(2000)081<1537:BHAM>2.3.CO;2. arXiv: arXiv:1011.1669v3. URL: [http://journals.ametsoc.org/doi/abs/10.1175/1520-0477\(2000\)081<1537:BHAM>2.3.CO;2](http://journals.ametsoc.org/doi/abs/10.1175/1520-0477(2000)081<1537:BHAM>2.3.CO;2).

- Galani, E. (2003). "Observations of stratosphere-to-troposphere transport events over the eastern Mediterranean using a ground-based lidar system". In: *Journal of Geophysical Research* 108.D12, pp. 1–10. ISSN: 0148-0227. DOI: 10.1029/2002JD002596. URL: <http://www.agu.org/pubs/crossref/2003/2002JD002596.shtml>.
- Giglio, Louis, James T. Randerson, and Guido R. Van Der Werf (2013). "Analysis of daily, monthly, and annual burned area using the fourth-generation global fire emissions database (GFED4)". In: *Journal of Geophysical Research* 118.1, pp. 317–328. ISSN: 21698961. DOI: 10.1002/jgrg.20042.
- Glasius, Marianne and Allen H. Goldstein (2016). "Recent Discoveries and Future Challenges in Atmospheric Organic Chemistry". In: *Environmental Science and Technology* 50.6, pp. 2754–2764. ISSN: 15205851. DOI: 10.1021/acs.est.5b05105.
- Gloudemans, Annemieke et al. (2006). "Evidence for long-range transport of carbon monoxide in the Southern Hemisphere from SCIAMACHY observations". In: *European Space Agency, (Special Publication)* 33.SP-636, pp. 1–5. ISSN: 03796566. DOI: 10.1029/2006GL026804.
- Goldberg, Daniel L. et al. (2017). "A high-resolution and observationally constrained OMI NO₂ satellite retrieval". In: *Atmospheric Chemistry and Physics* 17.18, pp. 11403–11421. ISSN: 16807324. DOI: 10.5194/acp-17-11403-2017.
- Gonzalez Abad, G. et al. (2015). "Updated Smithsonian Astrophysical Observatory Ozone Monitoring Instrument (SAO OMI) formaldehyde retrieval". In: *Atmospheric Measurement Techniques* 8.1, pp. 19–32. ISSN: 18678548. DOI: 10.5194/amt-8-19-2015.
- Greenslade, Jesse W et al. (2017). "Stratospheric ozone intrusion events and their impacts on tropospheric ozone in the Southern Hemisphere". In: *Atmospheric Chemistry and Physics*, pp. 1–33. URL: <https://www.atmos-chem-phys.net/17/10269/2017/acp-17-10269-2017.pdf>.
- Guenther, A et al. (2006). "Estimates of global terrestrial isoprene emissions using {MEGAN} (Model of Emissions of Gases and Aerosols from Nature)". In: *Atmospheric Chemistry and Physics* 6.11, pp. 3181–3210. DOI: 10.5194/acp-6-3181-2006. URL: <http://dx.doi.org/10.5194/acp-6-3181-2006>.
- Guenther, A. B. et al. (2012). "The model of emissions of gases and aerosols from nature version 2.1 (MEGAN2.1): An extended and updated framework for modeling biogenic emissions". In: *Geoscientific Model Development* 5.6, pp. 1471–1492. ISSN: 1991959X. DOI: 10.5194/gmd-5-1471-2012.
- Guenther, Alex et al. (1995). "A global model of natural volatile organic compound emissions". In: *Journal of Geophysical Research* 100.D5, pp. 8873–8892. ISSN: 0148-0227. DOI: 10.1029/94JD02950. URL: <http://onlinelibrary.wiley.com/doi/10.1029/94JD02950/full>.
- Guenther, Alex et al. (2000). "Natural emissions of non-methane volatile organic compounds, carbon monoxide, and oxides of nitrogen from North America". In: *Atmospheric Environment* 34.12-14, pp. 2205–2230. ISSN: 13522310. DOI: 10.1016/S1352-2310(99)00465-3.
- Guérette, Elise-Andrée et al. (2018). "Emissions of trace gases from Australian temperate forest fires: emission factors and dependence on modified combustion efficiency". In: *Atmospheric Chemistry and Physics* 18.5, pp. 3717–3735. ISSN: 1680-7324.

- DOI: 10.5194/acp-18-3717-2018. URL: <https://www.atmos-chem-phys.net/18/3717/2018/>.
- Hak, C. et al. (2005). "Intercomparison of four different in-situ techniques for ambient formaldehyde measurements in urban air". In: *Atmospheric Chemistry and Physics Discussions* 5.3, pp. 2897–2945. ISSN: 1680-7316. DOI: 10.5194/acpd-5-2897-2005.
- Hegglin, Michaela I and Theodore G Shepherd (2009). "Large climate-induced changes in ultraviolet index and stratosphere-to-troposphere ozone flux". In: *Nature Geoscience* 2.10, pp. 687–691. DOI: 10.1038/ngeo604. URL: <http://dx.doi.org/10.1038/ngeo604>.
- Hewitt, C N et al. (2011). "Ground-level ozone influenced by circadian control of isoprene emissions". In: *Nature Geoscience* 4.10, pp. 671–674. DOI: 10.1038/ngeo1271. URL: <http://dx.doi.org/10.1038/ngeo1271>.
- Hoek, Gerard et al. (2013). "Long-term air pollution exposure and cardio-respiratory mortality: a review". In: *Environmental Health* 12.1, p. 43. DOI: 10.1186/1476-069x-12-43. URL: <http://dx.doi.org/10.1186/1476-069x-12-43>.
- Horowitz, Larry W. et al. (1998). "Export of reactive nitrogen from North America during summertime: Sensitivity to hydrocarbon chemistry". In: *Journal of Geophysical Research* 103.D11, pp. 13451–13476. ISSN: 0148-0227. DOI: 10.1029/97JD03142. URL: <http://doi.wiley.com/10.1029/97JD03142> <http://www.agu.org/pubs/crossref/1998/97JD03142.shtml>.
- Hsieh, Nan-Hung and Chung-Min Liao (2013). "Fluctuations in air pollution give risk warning signals of asthma hospitalization". In: *Atmospheric Environment* 75, pp. 206–216. DOI: 10.1016/j.atmosenv.2013.04.043. URL: <http://dx.doi.org/10.1016/j.atmosenv.2013.04.043>.
- Hu, Lu et al. (2017). "Global budget of tropospheric ozone: evaluating recent model advances with satellite (OMI), aircraft (IAGOS), and ozonesonde observations". In: *Atmospheric Environment*, pp. 1–36. DOI: 10.1016/j.atmosenv.2017.08.036.
- Huang, Guanyu et al. (2018). "Validation of 10-year SAO OMI Ozone Profile (PROFOZ) Product Using Aura MLS Measurements". In: *Atmospheric Measurement Techniques* 11, pp. 17–32. ISSN: 1867-8610. DOI: 10.5194/amt-11-17-2018. URL: <https://www.atmos-meas-tech.net/11/17/2018/amt-11-17-2018.pdf>.
- Hudman, R. C. et al. (2012). "Steps towards a mechanistic model of global soil nitric oxide emissions: implementation and space based-constraints". In: *Atmospheric Chemistry and Physics* 12.16, pp. 7779–7795. ISSN: 1680-7324. DOI: 10.5194/acp-12-7779-2012. URL: <https://www.atmos-chem-phys.net/12/7779/2012/>.
- Jacob, Daniel J (1999). *Introduction to Atmospheric Chemistry*. Ed. by Daniel J Jacob. Princeton University Press. URL: <http://acmg.seas.harvard.edu/people/faculty/djj/book/index.html>.
- Jacobson, M C and H Hansson (2000). "Organic atmospheric aerosols: Review and state of the science". In: *Reviews of Geophysics* 38.2, pp. 267–294. ISSN: 87551209. DOI: 10.1029/1998RG000045. URL: <http://dx.doi.org/10.1029/1998RG000045>.
- Jaffe, Daniel a. and Nicole L. Wigder (2012). "Ozone production from wildfires: A critical review". In: *Atmospheric Environment* 51, pp. 1–10. ISSN: 13522310. DOI: 10.1016/j.atmosenv.2011.11.063. URL: <http://dx.doi.org/10.1016/j.atmosenv.2011.11.063>.

- Jiang, Xiaoyan et al. (2018). "Isoprene emission response to drought and the impact on global atmospheric chemistry". In: *Atmospheric Environment* 183, pp. 69–83. ISSN: 1352-2310. DOI: 10.1016/J.ATMOSENV.2018.01.026. URL: <https://www.sciencedirect.com/science/article/pii/S1352231018300402>.
- Jozef, Peeters et al. (2014). "Hydroxyl Radical Recycling in Isoprene Oxidation Driven by Hydrogen Bonding and Hydrogen Tunneling: The Upgraded LIM1 Mechanism". In: *Journal of Physical Chemistry*. URL: <https://pubs.acs.org/doi/10.1021/jp5033146>.
- Kaiser, Jennifer et al. (2018). "High-resolution inversion of OMI formaldehyde columns to quantify isoprene emission on ecosystem-relevant scales: application to the southeast US". In: *Atmospheric Chemistry and Physics* 18.8, pp. 5483–5497. DOI: 10.5194/acp-18-5483-2018. URL: <https://www.atmos-chem-phys.net/18/5483/2018/acp-18-5483-2018.pdf>.
- Kanakidou, M et al. (2005). "Physics Organic aerosol and global climate modelling : a review". In: *Atmospheric Chemistry and Physics* 5, pp. 1053–1123.
- Kefauver, Shawn C., Iolanda Filella, and Josep Peñuelas (2014). "Remote sensing of atmospheric biogenic volatile organic compounds (BVOCs) via satellite-based formaldehyde vertical column assessments". en. In: *International Journal of Remote Sensing*. URL: <http://www.tandfonline.com/doi/abs/10.1080/01431161.2014.968690>.
- Keywood, MD, KM Emmerson, and MF Hibberd (2016). *Australia state of the environment 2016*. Canberra. DOI: 10.4226/94/58b65c70bc372. URL: <https://soe.environment.gov.au/theme/atmosphere>.
- Keywood, Melita et al. (2016a). *Collection., Sydney Particle Study 1 - Aerosol and gas data collection. v3*. CSIRO. Data. DOI: 10.1594/PANGAEA.884317. URL: <https://doi.org/10.4225/08/57903B83D6A5D> (visited on 05/30/2019).
- Keywood, Melita et al. (2016b). "Sydney Particle Study 2 - Aerosol and gas data collection. v1". CSIRO. Data Collection." In: CSIRO. DOI: <https://doi.org/10.4225/08/5791B5528BD63>.
- Krewski, D et al. (2009). "Extended follow-up and spatial analysis of the American Cancer Society study linking particulate air pollution and mortality". In: *Res Rep Health Eff Inst* 140, pp. 5–36. ISSN: 1041-5505 (Print) 1041-5505 (Linking). URL: <http://www.ncbi.nlm.nih.gov/pubmed/19627030>.
- Kroll, Jesse H. and John H. Seinfeld (2008). "Chemistry of secondary organic aerosol: Formation and evolution of low-volatility organics in the atmosphere". In: *Atmospheric Environment* 42.16, pp. 3593–3624. ISSN: 13522310. DOI: 10.1016/j.atmosenv.2008.01.003. URL: <http://www.sciencedirect.com.ezproxy.uow.edu.au/science/article/pii/S1352231008000253>.
- Kuang, Shi et al. (2017). "Summertime tropospheric ozone enhancement associated with a cold front passage due to stratosphere-to-troposphere transport and biomass burning: Simultaneous ground-based lidar and airborne measurements". In: *Journal of Geophysical Research: Atmospheres* 122.2, pp. 1293–1311. ISSN: 21698996. DOI: 10.1002/2016JD026078. URL: <http://doi.wiley.com/10.1002/2016JD026078>.
- Kurosu, T and K Chance (2014). *OMIReadme*. URL: https://www.cfa.harvard.edu/atmosphere/Instruments/OMI/PGEReleases/READMEs/OMHCHO{_}README{_}v3.0.pdf.

- Kwon, Hyeong-Ahn et al. (2017). "Sensitivity of formaldehyde (HCHO) column measurements from a geostationary satellite to temporal variation of the air mass factor in East Asia". In: *Atmospheric Chemistry and Physics* 17.7, pp. 4673–4686. ISSN: 1680-7324. DOI: 10.5194/acp-17-4673-2017. URL: <http://www.atmos-chem-phys.net/17/4673/2017/>.
- Lamsal, L N et al. (2014). "Evaluation of OMI operational standard NO₂ column retrievals using in situ and surface-based NO₂ observations". In: *Atmos. Chem. Phys.* 14, pp. 11587–11609. DOI: 10.5194/acp-14-11587-2014. URL: www.atmos-chem-phys.net/14/11587/2014/.
- Langford, A. O. et al. (2012). "Stratospheric influence on surface ozone in the Los Angeles area during late spring and early summer of 2010". In: *Journal of Geophysical Research* 117.3, pp. 1–17. ISSN: 01480227. DOI: 10.1029/2011JD016766.
- Lathière, J et al. (2006). "Impact of climate variability and land use changes on global biogenic volatile organic compound emissions". In: *Atmospheric Chemistry and Physics* 6.2003, pp. 2129–2146. ISSN: 16807324. DOI: 10.5194/acp-6-2129-2006. URL: www.atmos-chem-phys.net/6/2129/2006/.
- Lawson, S. J. et al. (2015). "Seasonal in situ observations of glyoxal and methylglyoxal over the temperate oceans of the Southern Hemisphere". In: *Atmospheric Chemistry and Physics* 15.1, pp. 223–240. ISSN: 1680-7324. DOI: 10.5194/acp-15-223-2015. URL: <http://www.atmos-chem-phys.net/15/223/2015/>.
- Lawson, Sarah J. et al. (2017). "Biomass burning at Cape Grim: Exploring photochemistry using multi-scale modelling". In: *Atmospheric Chemistry and Physics* 17.19, pp. 11707–11726. ISSN: 16807324. DOI: 10.5194/acp-17-11707-2017. arXiv: 0006240 [astro-ph].
- Lee, Anita et al. (2006). "Gas-phase products and secondary aerosol yields from the ozonolysis of ten different terpenes". In: 111.Ci, pp. 1–18. DOI: 10.1029/2005JD006437.
- Lefohn, Allen S. et al. (2011). "The importance of stratospheric-tropospheric transport in affecting surface ozone concentrations in the western and northern tier of the United States". In: *Atmospheric Environment* 45.28, pp. 4845–4857. ISSN: 13522310. DOI: 10.1016/j.atmosenv.2011.06.014. URL: <http://dx.doi.org/10.1016/j.atmosenv.2011.06.014>.
- Lelieveld, J. et al. (2009). "Severe ozone air pollution in the Persian Gulf region". In: *Atmospheric Chemistry and Physics* 9, pp. 1393–1406. ISSN: 1680-7324. DOI: 10.5194/acp-9-1393-2009.
- Lelieveld, J. et al. (2013). "Model calculated global, regional and megacity premature mortality due to air pollution". In: *Atmospheric Chemistry and Physics* 13.14, pp. 7023–7037. ISSN: 16807324. DOI: 10.5194/acp-13-7023-2013.
- Lelieveld, J et al. (2015). "The contribution of outdoor air pollution sources to premature mortality on a global scale". In: *Nature* 525.7569, pp. 367–371. DOI: 10.1038/nature15371. URL: <http://dx.doi.org/10.1038/nature15371>.
- Lelieveld, Jos and Frank J. Dentener (2000). "What controls tropospheric ozone?" In: *Journal of Geophysical Research* 105.D3, pp. 3531–3551. ISSN: 01480227. DOI: 10.1029/1999JD901011. URL: <http://doi.wiley.com/10.1029/1999JD901011>.
- Lerner, Brian M. et al. (2017). "An improved, automated whole air sampler and gas chromatography mass spectrometry analysis system for volatile organic compounds in the atmosphere". In: *Atmospheric Measurement Techniques* 10.1, pp. 291–313. ISSN:

18678548. DOI: 10.5194/amt-10-291-2017. URL: <https://www.atmos-meas-tech.net/10/291/2017/amt-10-291-2017.pdf>.
- Leue, C et al. (2001). "Quantitative analysis of {NO} x emissions from Global Ozone Monitoring Experiment satellite image sequences". In: *J. Geophys. Res.* 106.D6, p. 5493. DOI: 10.1029/2000jd900572. URL: <http://dx.doi.org/10.1029/2000jd900572>.
- Levy, Hiram (1972). "Photochemistry of the lower troposphere". In: *Planetary and Space Science* 20.6, pp. 919–935. ISSN: 00320633. DOI: 10.1016/0032-0633(72)90177-8.
- Lieschke, Kaitlyn J. et al. (2019). "Decreasing trend in formaldehyde detected from 20-year record at Wollongong, Southeast Australia". In: *Geophysical Research Letters*. DOI: 10.1029/2019GL083757. URL: <https://doi.org/10.1029/2019GL083757>.
- Lin, Meiyun et al. (2012). "Springtime high surface ozone events over the western United States: Quantifying the role of stratospheric intrusions". In: *Journal of Geophysical Research* 117.19, pp. 1–20. ISSN: 01480227. DOI: 10.1029/2012JD018151.
- Lin, Meiyun et al. (2015). "Climate variability modulates western US ozone air quality in spring via deep stratospheric intrusions." In: *Nature communications* 6.May, p. 7105. ISSN: 2041-1723. DOI: 10.1038/ncomms8105. URL: <http://www.nature.com/ncomms/2015/150512/ncomms8105/full/ncomms8105.html>.
- Liu, Junhua et al. (2015). "Origins of tropospheric ozone interannual variation over Réunion: A model investigation". In: *Journal of Geophysical Research*, pp. 1–19. DOI: 10.1002/2015JD023981. URL: <http://onlinelibrary.wiley.com/doi/10.1002/2015JD023981/abstract>.
- Liu, Junhua et al. (2016a). "Causes of interannual variability of tropospheric ozone over the Southern Ocean". In: *Atmospheric Chemistry and Physics Discussions* October, pp. 1–46. ISSN: 1680-7316. DOI: 10.5194/ACP-2016-692.
- Liu, Junhua et al. (2017a). "Causes of interannual variability over the southern hemispheric tropospheric ozone maximum". In: *Atmos. Chem. Phys* 17.5, pp. 3279–3299. ISSN: 1680-7324. DOI: 10.5194/acp-17-3279-2017. URL: www.atmos-chem-phys.net/17/3279/2017/.
- Liu, Y. J. et al. (2013). "Production of methyl vinyl ketone and methacrolein via the hydroperoxyl pathway of isoprene oxidation". In: *Atmospheric Chemistry and Physics* 13.11, pp. 5715–5730. ISSN: 1680-7324. DOI: 10.5194/acp-13-5715-2013. URL: <http://www.atmos-chem-phys.net/13/5715/2013/>.
- Liu, Yingjun et al. (2016b). "Isoprene photochemistry over the Amazon rainforest". In: *Proceedings of the National Academy of Sciences* 113.22, pp. 6125–6130. ISSN: 0027-8424. DOI: 10.1073/pnas.1524136113. URL: <http://www.pnas.org/content/113/22/6125.abstract>.
- Liu, Zhen et al. (2017b). "Theoretically derived mechanisms of HPALD photolysis in isoprene oxidation". In: *Physical Chemistry Chemical Physics* 19.13, pp. 9096–9106. ISSN: 14639076. DOI: 10.1039/c7cp00288b.
- Lorente, Alba et al. (2017). "Structural uncertainty in air mass factor calculation for NO₂ and HCHO satellite retrievals". In: *Atmospheric Measurement Techniques* 2, pp. 1–35. ISSN: 1867-8610. DOI: 10.5194/amt-10-759-2017. URL: <https://www.atmos-meas-tech.net/10/759/2017/amt-10-759-2017.html>.
- Mao, J. et al. (2012). "Insights into hydroxyl measurements and atmospheric oxidation in a California forest". In: *Atmospheric Chemistry and Physics* 12.17, pp. 8009–8020. ISSN: 16807316. DOI: 10.5194/acp-12-8009-2012.

- Mao, Jingqiu et al. (2013). "Ozone and organic nitrates over the eastern United States: Sensitivity to isoprene chemistry". In: *Journal of Geophysical Research Atmospheres* 118.19, pp. 11256–11268. ISSN: 21698996. DOI: 10.1002/jgrd.50817.
- Marais, E A et al. (2012). "Isoprene emissions in Africa inferred from {OMI} observations of formaldehyde columns". In: *Atmospheric Chemistry and Physics* 12.3, pp. 7475–7520. DOI: 10.5194/acp-12-6219-2012. URL: <http://dx.doi.org/10.5194/acp-12-6219-2012>.
- Marais, E A et al. (2014). "Improved model of isoprene emissions in Africa using Ozone Monitoring Instrument ({OMI}) satellite observations of formaldehyde: implications for oxidants and particulate matter". In: *Atmospheric Chemistry and Physics* 14.15, pp. 7693–7703. DOI: 10.5194/acp-14-7693-2014. URL: <http://dx.doi.org/10.5194/acp-14-7693-2014>.
- Mari, C H et al. (2008). "Tracing biomass burning plumes from the Southern Hemisphere during the AMMA 2006 wet season experiment, Atmos". In: *Atmospheric Chemistry and Physics* 8, pp. 3951–3961. ISSN: 1680-7324. DOI: 10.5194/acpd-7-17339-2007.
- Martin, Randall V. (2003). "Global and regional decreases in tropospheric oxidants from photochemical effects of aerosols". In: *Journal of Geophysical Research* 108.D3, p. 4097. ISSN: 0148-0227. DOI: 10.1029/2002JD002622. URL: <http://doi.wiley.com/10.1029/2002JD002622>.
- Martin, Randall V. et al. (2002). "An improved retrieval of tropospheric nitrogen dioxide from GOME". In: *Journal of Geophysical Research D: Atmospheres* 107.20. ISSN: 01480227. DOI: 10.1029/2001JD001027.
- Martin, Randall V et al. (2003). "Global inventory of nitrogen oxide emissions constrained by space-based observations of NO₂ columns". In: 108.2, pp. 1–12. DOI: 10.1029/2003JD003453.
- Marvin, Margaret R. et al. (2017). "Impact of evolving isoprene mechanisms on simulated formaldehyde: An inter-comparison supported by in situ observations from SENEX". In: *Atmospheric Environment* 164, pp. 325–336. ISSN: 13522310. DOI: 10.1016/j.atmosenv.2017.05.049. URL: https://ac.els-cdn.com/S1352231017303618/1-s2.0-S1352231017303618-main.pdf?{_}tid=3de7eaaa-06ff-11e8-99a9-0000aacb360{\&}acdnat=1517455576{_}09d7334af609ed43470155c1c42fad5fhttp://www.sciencedirect.com/science/article/pii/S1352231017303618.
- Mazzuca, Gina M. et al. (2016). "Ozone production and its sensitivity to NO_x and VOCs: Results from the DISCOVER-AQ field experiment, Houston 2013". In: *Atmospheric Chemistry and Physics* 16.22, pp. 14463–14474. ISSN: 16807324. DOI: 10.5194/acp-16-14463-2016.
- Messina, Palmira et al. (2016). "Global biogenic volatile organic compound emissions in the ORCHIDEE and MEGAN models and sensitivity to key parameters". In: *Atmospheric Chemistry and Physics* 16.22, pp. 14169–14202. ISSN: 16807324. DOI: 10.5194/acp-16-14169-2016. URL: <http://www.atmos-chem-phys.net/16/14169/2016/acp-16-14169-2016.pdf>.
- Mihalikova, M et al. (2012). "Observation of a tropopause fold by MARA VHF wind-profiler radar and ozonesonde at Wasa, Antarctica: comparison with ECMWF analysis and a WRF model simulation". In: *Annales Geophysicae* 30.9, pp. 1411–1421.

- DOI: 10.5194/angeo-30-1411-2012. URL: <http://www.ann-geophys.net/30/1411/2012/>.
- Miller, C. et al. (2014). "Glyoxal retrieval from the Ozone Monitoring Instrument". In: *Atmospheric Measurement Techniques* 7.11, pp. 3891–3907. ISSN: 1867-8548. DOI: 10.5194/amt-7-3891-2014. URL: <http://www.atmos-meas-tech.net/7/3891/2014/>.
- Millet, Dylan B et al. (2006). "Formaldehyde distribution over North America: Implications for satellite retrievals of formaldehyde columns and isoprene emission". In: *J. Geophys. Res.* 111.D24. DOI: 10.1029/2005jd006853. URL: TODO.
- Millet, Dylan B. et al. (2008). "Spatial distribution of isoprene emissions from North America derived from formaldehyde column measurements by the OMI satellite sensor". In: *Journal of Geophysical Research Atmospheres* 113.2, pp. 1–18. ISSN: 01480227. DOI: 10.1029/2007JD008950.
- Millet, Dylan B. et al. (2016). "Nighttime Chemistry and Morning Isoprene Can Drive Urban Ozone Downwind of a Major Deciduous Forest". In: *Environmental Science and Technology* 50.8, pp. 4335–4342. ISSN: 15205851. DOI: 10.1021/acs.est.5b06367. URL: <https://pubs.acs.org/doi/pdfplus/10.1021/acs.est.5b06367>.
- Monks, P. S. et al. (2015). "Tropospheric ozone and its precursors from the urban to the global scale from air quality to short-lived climate forcer". In: *Atmospheric Chemistry and Physics* 15.15, pp. 8889–8973. ISSN: 1680-7324. DOI: 10.5194/acp-15-8889-2015. URL: <http://www.atmos-chem-phys.net/15/8889/2015/>.
- Myhre, G and D Shindell (2013). *Chapter 8: Anthropogenic and Natural Radiative Forcing, in Climate Change 2013: The Physical Science Basis, Working Group 1 Contribution to the Fifth Assessment Report of the Intergovernmental Panel on Climate Change*, 2013. Fifth Assessment Report of the Intergovernmental Panel on Climate Change, 2013.
- Mze, N. et al. (2010). "Climatology and comparison of ozone from ENVISAT/GOMOS and SHADOZ/balloon-sonde observations in the southern tropics". In: *Atmospheric Chemistry and Physics* 10.16, pp. 8025–8035. ISSN: 16807316. DOI: 10.5194/acp-10-8025-2010.
- Nguyen, T. B. et al. (2014). "Overview of the Focused Isoprene eXperiment at the California Institute of Technology (FIXCIT): Mechanistic chamber studies on the oxidation of biogenic compounds". In: *Atmospheric Chemistry and Physics* 14.24. ISSN: 16807324. DOI: 10.5194/acp-14-13531-2014.
- Nguyen, Tran B. et al. (2016). "Atmospheric fates of Criegee intermediates in the ozonolysis of isoprene". In: *Phys. Chem. Chem. Phys.* 18.15, pp. 10241–10254. ISSN: 1463-9076. DOI: 10.1039/C6CP00053C. URL: <http://xlink.rsc.org/?DOI=C6CP00053C>.
- Niinemets, U. et al. (1999). "A model of isoprene emission based on energetic requirements for isoprene synthesis and leaf photosynthetic properties for Liquidambar and Quercus". In: *Plant, Cell and Environment* 22.11, pp. 1319–1335. ISSN: 01407791. DOI: 10.1046/j.1365-3040.1999.00505.x.
- Niinemets, U. et al. (2010). "The emission factor of volatile isoprenoids: Stress, acclimation, and developmental responses". In: *Biogeosciences* 7.7, pp. 2203–2223. ISSN: 17264170. DOI: 10.5194/bg-7-2203-2010.
- NOAA. *Earth System Research Laboratory; Global Monitoring Division*. URL: https://esrl.noaa.gov/gmd/ccgg/trends{_}ch4/ (visited on 06/18/2019).
- Ojha, Narendra et al. (2016). "Secondary ozone peaks in the troposphere over the Himalayas". In: *Atmospheric Chemistry and Physics Discussions* 17.November, pp. 1–

25. ISSN: 1680-7375. DOI: 10.5194/acp-2016-908. URL: <http://www.atmos-chem-phys-discuss.net/acp-2016-908/>.
- Olsen, Mark a. (2003). "A comparison of Northern and Southern Hemisphere cross-tropopause ozone flux". In: *Geophysical Research Letters* 30.7, p. 1412. ISSN: 0094-8276. DOI: 10.1029/2002GL016538. URL: <http://doi.wiley.com/10.1029/2002GL016538>.
- Oltmans, J et al. (2001). "Ozone in the Pacific tropical troposphere from ozonesonde observations". In: *Journal of Geophysical Research* 106.D23, pp. 32503–32525.
- Pak, B.C.a et al. (2003). "Measurements of biomass burning influences in the troposphere over southeast Australia during the SAFARI 2000 dry season campaign". In: *Journal of Geophysical Research* 108.13, SAF 16–1 –SAF 16–10. ISSN: 0148-0227. DOI: 10.1029/2002JD002343. URL: <http://www.scopus.com/inward/record.url?eid=2-s2.0-0742322536&partnerID=40&md5=cafafef03b948fb456696583ed3ab9a5>.
- Palmer, Paul I et al. (2001). "Air mass factor formulation for spectroscopic measurements from satellites' Application to formaldehyde retrievals from the Global Ozone Monitoring Experiment". In: *Journal of Geophysical Research* 106.D13.
- Palmer, Paul I et al. (2003). "Mapping isoprene emissions over North America using formaldehyde column observations from space". In: *J. Geophys. Res.* 108.D6. DOI: 10.1029/2002jd002153. URL: <http://dx.doi.org/10.1029/2002jd002153>.
- Palmer, Paul I et al. (2006). "Quantifying the seasonal and interannual variability of North American isoprene emissions using satellite observations of the formaldehyde column". In: *J. Geophys. Res.* 111, p. D12315. ISSN: 0148-0227. DOI: 10.1029/2005JD006689. URL: <http://dx.doi.org/10.1029/2005JD006689>.
- Patchen, Amie K. et al. (2007). "Direct Kinetics Study of the Product-Forming Channel of the Reaction of Isoprene-Derived Hydroxyperoxy Radicals with NO". In: *International journal of Chemical Kinetics* 31.5, pp. 493–499. ISSN: 13000527. DOI: 10.1002/kin. URL: <http://onlinelibrary.wiley.com/wol1/doi/10.1002/kin.20248/full>.
- Paton-Walsh, C et al. (2017). "The MUMBA campaign: measurements of urban, marine and biogenic air". In: *Earth system science data*, pp. 349–362.
- Paton-Walsh, Clare et al. (2018). "Urban Air Quality in a Coastal City: Wollongong during the MUMBA Campaign". In: *Atmosphere*. URL: <https://www.mdpi.com/2073-4433/9/12/500/htm>.
- Paulot, F, D K Henze, and P O Wennberg (2012). "Impact of the isoprene photochemical cascade on tropical ozone". In: *Atmos. Chem. Phys. Atmospheric Chemistry and Physics* 12, pp. 1307–1325. DOI: 10.5194/acp-12-1307-2012. URL: www.atmos-chem-phys.net/12/1307/2012/.
- Paulot, F. et al. (2009a). "Isoprene photooxidation: new insights into the production of acids and organic nitrates". In: *Atmospheric Chemistry and Physics* 9.4, pp. 1479–1501. ISSN: 1680-7324. DOI: 10.5194/acp-9-1479-2009.
- Paulot, Fabien et al. (2009b). "Unexpected Epoxide Formation in the Gas-Phase Photooxidation of Isoprene". In: *Science* 325.2009, pp. 730–733. ISSN: 0036-8075. DOI: 10.1126/science.1172910. URL: <https://science.sciencemag.org/content/325/5941/730.abstract>.

- Peeters, J., T. L. Nguyen, and L. Vereecken (2009). "HOx radical regeneration in the oxidation of isoprene". In: *Physical Chemistry Chemical Physics* 11.28, p. 5935. ISSN: 1463-9076. DOI: 10.1039/b908511d. URL: <http://xlink.rsc.org/?DOI=b908511d>.
- Peeters, Jozef and Jean-Francis Muller (2010). "HOx radical regeneration in isoprene oxidation via peroxy radical isomerisations. II: experimental evidence and global impact". In: *Physical Chemistry Chemical Physics* 12.42, p. 14227. ISSN: 1463-9076. DOI: 10.1039/c0cp00811g. URL: <http://pubs.rsc.org/en/content/articlepdf/2010/cp/c0cp00811g>.
- Pegoraro, E. et al. (2004). "Effect of drought on isoprene emission rates from leaves of *Quercus virginiana* Mill." In: *Atmospheric Environment* 38.36, pp. 6149–6156. ISSN: 13522310. DOI: 10.1016/j.atmosenv.2004.07.028. URL: <http://linkinghub.elsevier.com/retrieve/pii/S1352231004007198>.
- Press, William H et al. (1992). *Numerical Recipes in C (2Nd Ed.): The Art of Scientific Computing*. New York, NY, USA: Cambridge University Press. ISBN: 0-521-43108-5.
- Price, J. D. and G. Vaughan (1993). "The potential for stratosphere-troposphere exchange in cut-off-low systems". In: *Quarterly Journal of the Royal Meteorological Society* 119.510, pp. 343–365. DOI: 10.1002/qj.49711951007. URL: <http://onlinelibrary.wiley.com/doi/10.1002/qj.49711951007/abstract>.
- Reutter, P. et al. (2015). "Stratosphere-troposphere exchange (STE) in the vicinity of North Atlantic cyclones". In: *Atmospheric Chemistry and Physics* 15.19, pp. 10939–10953. ISSN: 16807324. DOI: 10.5194/acp-15-10939-2015.
- Rienecker, Michele (2007). "File Specification for GEOS-5 DAS Gridded Output". In: pp. 1–54. URL: https://gmao.gsfc.nasa.gov/products/documents/GEOS-5.1.0__File__Specification.pdf.
- Roelofs, Geert Jan and Jos Lelieveld (1997). *Model study of the influence of cross-tropopause O₃ transports on tropospheric O₃ levels*. DOI: 10.1034/j.1600-0889.49.issue1.3.x.
- Rollins, A W et al. (2009). "Isoprene oxidation by nitrate radical: alkyl nitrate and secondary organic aerosol yields". In: *Atmos. Chem. Phys. Atmospheric Chemistry and Physics* 9, pp. 6685–6703. URL: www.atmos-chem-phys.net/9/6685/2009/.
- Romer Present, Paul S., Azimeh Zare, and Ronald C. Cohen (2019). "The changing role of organic nitrates in the removal and transport of NO_x". In: *Atmospheric Chemistry and Physics Discussions* x, pp. 1–18. DOI: 10.5194/acp-2019-471. URL: <https://www.atmos-chem-phys-discuss.net/acp-2019-471/>.
- Russell-Smith, Jeremy et al. (2007). "Bushfires 'down under': patterns and implications of contemporary Australian landscape burning". In: *International Journal of Wildland Fire* 16.4, p. 361. ISSN: 1049-8001. DOI: 10.1071/wf07018. URL: https://www.researchgate.net/publication/228969191__Bushfires__’down__under’__Patterns__and__implications__of__contemporary__Australian__landscape__burning.
- Schenkeveld, V. M. Erik et al. (2017). "In-flight performance of the Ozone Monitoring Instrument". In: *Atmospheric Measurement Techniques* 10.5, pp. 1957–1986. ISSN: 1867-8548. DOI: 10.5194/amt-10-1957-2017. URL: <https://www.atmos-meas-tech.net/10/1957/2017/>.
- Selin, N E et al. (2009). "Global health and economic impacts of future ozone pollution". In: *Environmental Research Letters* 4.4, p. 044014. ISSN: 1748-9326. DOI: 10.1088/1748-9326/4/4/044014.

- Shao, Yaping et al. (2007). "Numerical simulation of the October 2002 dust event in Australia". In: *J. Geophys. Res.* 112.D8. DOI: 10.1029/2006jd007767. URL: <http://dx.doi.org/10.1029/2006jd007767>.
- Shim, Changsub et al. (2005). "Constraining global isoprene emissions with Global Ozone Monitoring Experiment (GOME) formaldehyde column measurements". In: *Journal of Geophysical Research Atmospheres* 110.24, pp. 1–14. ISSN: 01480227. DOI: 10.1029/2004JD005629.
- Sillman, Sanford (1999). "The relation between ozone, NO and hydrocarbons in urban and polluted rural environments". In: *Atmospheric Environment* 33. DOI: [https://doi.org/10.1016/S1352-2310\(98\)00345-8](https://doi.org/10.1016/S1352-2310(98)00345-8). URL: <http://www-personal.umich.edu/~sillman/web-publications/Sillmanreview99.pdf> <https://www.sciencedirect.com/science/article/pii/S1352231098003458>.
- Silva, Raquel A et al. (2013). "Global premature mortality due to anthropogenic outdoor air pollution and the contribution of past climate change". In: *Environ. Res. Lett.* 8.3, p. 34005. DOI: 10.1088/1748-9326/8/3/034005. URL: <http://dx.doi.org/10.1088/1748-9326/8/3/034005>.
- Sindelarova, K. et al. (2014). "Global data set of biogenic VOC emissions calculated by the MEGAN model over the last 30 years". In: *Atmospheric Chemistry and Physics* 14.17, pp. 9317–9341. ISSN: 16807324. DOI: 10.5194/acp-14-9317-2014. arXiv: [arXiv:1011.1669v3](https://arxiv.org/abs/1011.1669v3).
- Sinha, Parikhit et al. (2004). "Transport of biomass burning emissions from southern Africa". In: *Journal of Geophysical Research* 109, p. D20204. ISSN: 01480227. DOI: 10.1029/2004JD005044.
- Škerlak, B, M Sprenger, and H Wernli (2014). "A global climatology of stratosphere-troposphere exchange using the ERA-Interim data set from 1979 to 2011". In: *Atmospheric Chemistry and Physics* 14.2, pp. 913–937. DOI: 10.5194/acp-14-913-2014. URL: <http://www.atmos-chem-phys.net/14/913/2014/>.
- Škerlak, Bojan et al. (2015). "Tropopause folds in ERA-Interim: Global climatology and relation to extreme weather events". In: *Journal of Geophysical Research* 120.10, pp. 4860–4877. ISSN: 21698996. DOI: 10.1002/2014JD022787.
- Smit, Herman G J et al. (2007). "Assessment of the performance of ECC-ozonesondes under quasi-flight conditions in the environmental simulation chamber: Insights from the Juelich Ozone Sonde Intercomparison Experiment (JOSIE)". In: *Journal of Geophysical Research* 112.19, pp. 1–18. ISSN: 01480227. DOI: 10.1029/2006JD007308.
- Sprenger, Michael, Mischa Croci Maspoch, and Heini Wernli (2003). "Tropopause folds and cross-tropopause exchange: A global investigation based upon ECMWF analyses for the time period March 2000 to February 2001". In: *Journal of Geophysical Research* 108.D12. ISSN: 2156-2202. DOI: 10.1029/2002JD002587. URL: <http://dx.doi.org/10.1029/2002JD002587>.
- Spurr, R. J D (2002). "Simultaneous derivation of intensities and weighting functions in a general pseudo-spherical discrete ordinate radiative transfer treatment". In: *Journal of Quantitative Spectroscopy and Radiative Transfer* 75.2, pp. 129–175. ISSN: 00224073. DOI: 10.1016/S0022-4073(01)00245-X.
- Spurr, R.J.D., T.P. Kurosu, and K.V. Chance (2001). "A linearized discrete ordinate radiative transfer model for atmospheric remote-sensing retrieval". In: *Journal of Quantitative Spectroscopy and Radiative Transfer* 68.6, pp. 689–735. DOI: 10.1016/

- S0022-4073(00)00055-8. URL: <https://www.sciencedirect.com/science/article/pii/S0022407300000558>.
- Stavrakou, T et al. (2009). "Evaluating the performance of pyrogenic and biogenic emission inventories against one decade of space-based formaldehyde columns". In: *Atmospheric Chemistry and Physics* 9.3, pp. 1037–1060. DOI: 10.5194/acp-9-1037-2009. URL: <http://dx.doi.org/10.5194/acp-9-1037-2009>.
- Stavrakou, T. et al. (2014). "Isoprene emissions over Asia 1979-2012: Impact of climate and land-use changes". In: *Atmospheric Chemistry and Physics* 14.9. ISSN: 16807324. DOI: 10.5194/acp-14-4587-2014. URL: <https://www.atmos-chem-phys.net/14/4587/2014/acp-14-4587-2014.pdf>.
- Stavrakou, T. et al. (2015). "How consistent are top-down hydrocarbon emissions based on formaldehyde observations from GOME-2 and OMI?" English. In: *Atmospheric Chemistry and Physics* 15.20, pp. 11861–11884. ISSN: 1680-7324. DOI: 10.5194/acp-15-11861-2015. URL: <http://www.atmos-chem-phys.net/15/11861/2015/acp-15-11861-2015.html>.
- Stevenson, D S et al. (2006). "Multimodel ensemble simulations of present-day and near-future tropospheric ozone". In: *Journal of Geophysical Research* 111.D8. DOI: 10.1029/2005jd006338. URL: <http://dx.doi.org/10.1029/2005JD006338>.
- Stevenson, D. S. et al. (2013). "Tropospheric ozone changes, radiative forcing and attribution to emissions in the Atmospheric Chemistry and Climate Model Intercomparison Project (ACCMIP)". In: *Atmospheric Chemistry and Physics* 13.6, pp. 3063–3085. ISSN: 16807316. DOI: 10.5194/acp-13-3063-2013.
- Stocker, T.F. et al. *IPCC, 2013: Climate Change 2013: The Physical Science Basis. Contribution of Working Group I to the Fifth Assessment Report of the Intergovernmental Panel on Climate Change*. Tech. rep. Cambridge University Press, Cambridge, United Kingdom and New York, NY, USA. DOI: 10.1017/CBO9781107415324.
- Stohl, Andreas et al. (2003). "A new perspective of stratosphere-troposphere exchange". In: *Bulletin of the American Meteorological Society* 84.11, pp. 1565–1573+1473. ISSN: 00030007. DOI: 10.1175/BAMS-84-11-1565.
- Stone, K. et al. (2015). "A new Dobson Umkehr ozone profile retrieval method optimising information content and resolution". In: *Atmospheric Measurement Techniques* 8.3, pp. 1043–1053. ISSN: 18678548. DOI: 10.5194/amt-8-1043-2015.
- Streets, David G et al. (2013). "Emissions estimation from satellite retrievals: A review of current capability". In: *Atmospheric Environment* 77, pp. 1011–1042. DOI: 10.1016/j.atmosenv.2013.05.051. URL: <http://dx.doi.org/10.1016/j.atmosenv.2013.05.051>.
- Struthers, H. et al. (2004). "Past and future simulations of NO₂ from a coupled chemistry-climate model in comparison with observations". In: *Atmospheric Chemistry and Physics* 4.8, pp. 2227–2239. ISSN: 1680-7324. DOI: 10.5194/acp-4-2227-2004. URL: <http://www.atmos-chem-phys.net/4/2227/2004/>.
- Surl, Luke, Paul I. Palmer, and Gonzalo G. Abad (2018). "Which processes drive observed variations of HCHO columns over India?" In: *Atmospheric Chemistry and Physics* 18.March, pp. 4549–4566. DOI: 10.5194/acp-18-4549-2018. URL: <https://doi.org/10.5194/acp-18-4549-2018>.

- Tang, Q. and M. J. Prather (2010). "Correlating tropospheric column ozone with tropopause folds: The Aura-OMI satellite data". In: *Atmospheric Chemistry and Physics* 10.19, pp. 9681–9688. ISSN: 16807316. DOI: 10.5194/acp-10-9681-2010.
- (2012). "Five blind men and the elephant: What can the NASA Aura ozone measurements tell us about stratosphere-troposphere exchange?" In: *Atmospheric Chemistry and Physics* 12.5, pp. 2357–2380. ISSN: 16807316. DOI: 10.5194/acp-12-2357-2012. URL: <http://dx.doi.org/10.5194/acpd-11-26897-2011>.
- Taraborrelli, D. et al. (2012). "Hydroxyl radical buffered by isoprene oxidation over tropical forests". In: *Nature Geoscience* 5.3, pp. 190–193. ISSN: 17520894. DOI: 10.1038/ngeo1405. URL: <http://dx.doi.org/10.1038/ngeo1405> <https://www.nature.com/articles/ngeo1405.pdf>.
- Terao, Yukio et al. (2008). "Contribution of stratospheric ozone to the interannual variability of tropospheric ozone in the northern extratropics". In: *Journal of Geophysical Research* 113.D18. DOI: 10.1029/2008jd009854. URL: <http://dx.doi.org/10.1029/2008jd009854>.
- Texeira, Joao (2013). *AIRS/Aqua L3 Daily Standard Physical Retrieval (AIRS-only) 1 degree x 1 degree V006*: Accessed 2/Dec/2015. DOI: doi:10.5067/AQUA/AIRS/DATA303.
- Thomas, W et al. (1998). "Detection of biomass burning combustion products in Southeast Asia from backscatter data taken by the GOME spectrometer". In: *Geophysical Research Letters* 25.9, pp. 1317–1320. DOI: 10.1029/98GL01087. URL: <http://onlinelibrary.wiley.com/doi/10.1029/98GL01087/epdf>.
- Thompson, A. M. et al. (2014). "Tropospheric ozone increases over the southern Africa region: Bellwether for rapid growth in Southern Hemisphere pollution?" In: *Atmospheric Chemistry and Physics* 14.18, pp. 9855–9869. ISSN: 16807324. DOI: 10.5194/acp-14-9855-2014.
- Tomikawa, Yoshihiro, Yashiro Nishimura, and Takashi Yamanouchi (2009). "Characteristics of Tropopause and Tropopause Inversion Layer in the Polar Region". In: *SOLA* 5, pp. 141–144. DOI: 10.2151/sola.2009-036. URL: <http://dx.doi.org/10.2151/sola.2009-036>.
- Torres, Omar O. (2008). *OMI/Aura Near UV Aerosol Optical Depth and Single Scattering Albedo L3*. DOI: 10.5067/Aura/OMI/DATA3003. URL: https://disc.gsfc.nasa.gov/datasets/OMAERUVd{_}V003/summary (visited on 05/30/2019).
- Travis, Katherine R et al. (2016). "Why do models overestimate surface ozone in the Southeast United States?" In: *Atmos. Chem. Phys* 16, pp. 13561–13577. DOI: 10.5194/acp-16-13561-2016. URL: www.atmos-chem-phys.net/16/13561/2016/.
- Trickl, T. et al. (2014). "How stratospheric are deep stratospheric intrusions?" In: *Atmospheric Chemistry and Physics* 14.18, pp. 9941–9961. ISSN: 16807324. DOI: 10.5194/acp-14-9941-2014.
- Tyrlis, Evangelos et al. (2014). "On the linkage between the Asian summer monsoon and tropopause fold activity over the eastern Mediterranean and the Middle East". In: *Journal of Geophysical Research* 119.6, pp. 3202–3221. ISSN: 2169897X. DOI: 10.1002/2013JD021113. URL: <http://doi.wiley.com/10.1002/2013JD021113>.
- VanDerA, R J et al. (2008). "Trends seasonal variability and dominant {NO} x source derived from a ten year record of {NO} 2 measured from space". In: *J. Geophys. Res.* 113.D4. DOI: 10.1029/2007jd009021. URL: <http://dx.doi.org/10.1029/2007jd009021>.

- Vasilkov, A et al. (2017). "Accounting for the effects of surface BRDF on satellite cloud and trace-gas retrievals: a new approach based on geometry-dependent Lambertian equivalent reflectivity applied to OMI algorithms". In: *Atmospheric Measurement Techniques* 10.1, pp. 333–349. DOI: 10.5194/amt-10-333-2017. URL: <http://www.atmos-meas-tech.net/10/333/2017/>.
- Vaughan, G., J. D. Price, and A. Howells (1993). "Transport into the troposphere in a tropopause fold". In: *Quarterly Journal of the Royal Meteorological Society* 120.518, pp. 1085–1103. ISSN: 00359009. DOI: 10.1002/qj.49712051814.
- Vigouroux, C. et al. (2009). "Ground-based FTIR and MAX-DOAS observations of formaldehyde at Réunion Island and comparisons with satellite and model data". In: *Atmospheric Chemistry and Physics Discussions* 9, pp. 15891–15957. ISSN: 1680-7316. DOI: 10.5194/acpd-9-15891-2009.
- Wagner, V (2002). "Are CH₂O measurements in the marine boundary layer suitable for testing the current understanding of CH₄ photooxidation?: A model study". In: *Journal of Geophysical Research* 107.D3, p. 4029. ISSN: 0148-0227. DOI: 10.1029/2001JD000722. URL: <http://doi.wiley.com/10.1029/2001JD000722>.
- Wauben, Wiel M F, J Paul F Fortuin, and Peter F J Van Velthoven (1998). "Comparison of modeled ozone distributions observations". In: *Journal of Geophysical Research* 103, pp. 3511–3530.
- Wild, Oliver and Michael J. Prather (2006). "Global tropospheric ozone modeling: Quantifying errors due to grid resolution". In: *Journal of Geophysical Research Atmospheres* 111.11, pp. 1–14. ISSN: 01480227. DOI: 10.1029/2005JD006605.
- Winters, Anthony J et al. (2009). "Emissions of isoprene, monoterpene and short-chained carbonyl compounds from Eucalyptus spp. in southern Australia". In: *Atmospheric Environment* 43.19, pp. 3035–3043. ISSN: 13522310. DOI: 10.1016/j.atmosenv.2009.03.026.
- Wirth, Volkmar (1995). "Diabatic heating in an axisymmetric cut-off cyclone and related stratosphere-troposphere exchange". In: *Quarterly Journal of the Royal Meteorological Society* 121.521, pp. 127–147. ISSN: 00359009. DOI: 10.1002/qj.49712152107. URL: <http://doi.wiley.com/10.1002/qj.49712152107>.
- WMO, World Meteorological Organization (1957). "Meteorology A Three-Dimensional Science". In: *Geneva, Second Session of the Commission for Aerology* 4, pp. 134–138.
- Wolfe, G. M. et al. (2016). "Formaldehyde production from isoprene oxidation across NO_x regimes". In: *Atmospheric Chemistry and Physics* 16.x, pp. 2597–2610. ISSN: 16807324. DOI: 10.5194/acp-16-2597-2016. URL: <https://www.atmos-chem-phys.net/16/2597/2016/acp-16-2597-2016.pdf>.
- Wolfe, Glenn M. et al. (2012). "Photolysis, OH reactivity and ozone reactivity of a proxy for isoprene-derived hydroperoxyenals (HPALDs)". In: *Physical Chemistry Chemical Physics* 14.20, p. 7276. ISSN: 1463-9076. DOI: 10.1039/c2cp40388a. URL: <http://xlink.rsc.org/?DOI=c2cp40388a>.
- Wuebbles, Donald J and Katharine Hayhoe (2002). "Atmospheric methane and global change". In: *Earth-Science Reviews* 57.3-4, pp. 177–210. ISSN: 0012-8252. DOI: 10.1016/S0012-8252(01)00062-9. URL: <https://www.sciencedirect.com/science/article/pii/S0012825201000629?via%20ihub>.
- Young, P. J. et al. (2013). "Preindustrial to present-day changes in tropospheric hydroxyl radical and methane lifetime from the Atmospheric Chemistry and Climate

- Model Intercomparison Project (ACCMIP)". In: *Atmospheric Chemistry and Physics* 13.10, pp. 5277–5298. ISSN: 16807316. DOI: 10.5194/acp-13-5277-2013.
- Young, P J et al. (2017). "Tropospheric Ozone Assessment Report (TOAR): Assessment of global-scale model performance for global and regional ozone distributions, variability, and trends". In: *Elementa: Science of the Anthropocene*, pp. 0–84. ISSN: 2325-1026. DOI: 10.1525/elementa.265. URL: http://eprints.lancs.ac.uk/88836/1/TOAR__Model__Performance__07062017.pdf0Ahttp://www.igacproject.org/sites/default/files/2017-05/TOAR-Model__Performance__draft__for__open__comment.pdf.
- Yu, Karen et al. (2016). "Sensitivity to grid resolution in the ability of a chemical transport model to simulate observed oxidant chemistry under high-isoprene conditions". In: *Atmospheric Chemistry and Physics* 16.7, pp. 4369–4378. ISSN: 16807324. DOI: 10.5194/acp-16-4369-2016. URL: http://acmg.seas.harvard.edu/publications/2016/Yu__ACP__2016.pdf.
- Yue, X., N. Unger, and Y. Zheng (2015). "Distinguishing the drivers of trends in land carbon fluxes and plant volatile emissions over the past 3 decades". In: *Atmospheric Chemistry and Physics* 15.20, pp. 11931–11948. ISSN: 16807324. DOI: 10.5194/acp-15-11931-2015.
- Yue, Xu et al. (2017). "Ozone and haze pollution weakens net primary productivity in China". In: *Atmospheric Chemistry and Physics* 17.9, pp. 6073–6089. ISSN: 1680-7324. DOI: 10.5194/acp-17-6073-2017. URL: <https://www.atmos-chem-phys.net/17/6073/2017/>.
- Zanis, P. et al. (2014). "Summertime free-tropospheric ozone pool over the eastern Mediterranean/middle east". In: *Atmospheric Chemistry and Physics* 14.1, pp. 115–132. ISSN: 16807316. DOI: 10.5194/acp-14-115-2014.
- Zeng, G. et al. (2015). "Multi-model simulation of CO and HCHO in the Southern Hemisphere: comparison with observations and impact of biogenic emissions". In: *Atmospheric Chemistry and Physics* 15.13, pp. 7217–7245. ISSN: 1680-7324. DOI: 10.5194/acp-15-7217-2015. URL: <http://www.atmos-chem-phys.net/15/7217/2015/>.
- Zeng, Guang et al. (2017). "Attribution of recent ozone changes in the Southern Hemisphere mid-latitudes using statistical analysis and chemistry-climate model simulations". In: *Atmospheric Chemistry and Physics* 17.17, pp. 10495–10513. ISSN: 16807324. DOI: 10.5194/acp-17-10495-2017.
- Zhang, L et al. (2014). "Sources contributing to background surface ozone in the {US} Intermountain West". In: *Atmospheric Chemistry and Physics* 14.11, pp. 5295–5309. DOI: 10.5194/acp-14-5295-2014. URL: <http://dx.doi.org/10.5194/acp-14-5295-2014>.
- Zhang, Yang et al. (2012). "Impact of gas-phase mechanisms on Weather Research Forecasting Model with Chemistry (WRF/Chem) predictions: Mechanism implementation and comparative evaluation". In: *Journal of Geophysical Research: Atmospheres* 117.D1, n/a-n/a. DOI: 10.1029/2011JD015775. URL: <http://doi.wiley.com/10.1029/2011JD015775>.
- Zheng, Y. et al. (2015). "Relationships between photosynthesis and formaldehyde as a probe of isoprene emission". In: *Atmospheric Chemistry and Physics* 15.15, pp. 8559–8576. ISSN: 16807324. DOI: 10.5194/acp-15-8559-2015.

- Zhu, Lei et al. (2013). "Variability of HCHO over the Southeastern United States observed from space : Implications for VOC emissions". In: vol. 1.
- Zhu, Lei et al. (2014). "Anthropogenic emissions of highly reactive volatile organic compounds in eastern Texas inferred from oversampling of satellite (OMI) measurements of HCHO columns". In: *Environmental Research Letters* 9.11, p. 114004. ISSN: 1748-9326. DOI: 10 . 1088 / 1748 - 9326 / 9 / 11 / 114004. URL: <http://stacks.iop.org/1748-9326/9/i=11/a=114004?key=crossref.3d2869ee02fd4f0792f831ac8cbe117>.
- Zhu, Lei et al. (2016). "Observing atmospheric formaldehyde (HCHO) from space: validation and intercomparison of six retrievals from four satellites (OMI, GOME2A, GOME2B, OMPS) with SEAC4RS aircraft observations over the Southeast US". In: *Atmospheric Chemistry and Physics* 0.March, pp. 1–24. ISSN: 1680-7375. DOI: 10.5194/acp-2016-162. URL: <http://www.atmos-chem-phys.net/16/13477/2016/acp-16-13477-2016.pdf>.